SEARCH FOR LONG-LIVED PARTICLES PRODUCED IN PROTON-PROTON COLLISIONS AT $\sqrt{S}$=13 TEV THAT DECAY TO DISPLACED HADRONIC JETS DETECTED WITH THE MUON SPECTROMETER IN ATLAS

by

Hao Zhou

A Dissertation Submitted to the Faculty of the

DEPARTMENT OF PHYSICS

In Partial Fulfillment of the Requirements
For the Degree of

DOCTOR OF PHILOSOPHY

In the Graduate College

THE UNIVERSITY OF ARIZONA

2021

THE UNIVERSITY OF ARIZONA
GRADUATE COLLEGE

As members of the Dissertation Committee, we certify that we have read the dissertation prepared by: Hao Zhou

titled: Search for Long-Lived Particles Produced in Proton-Proton Collisions at $\sqrt{s} = 13$ TeV That Decay to Displaced Hadronic Jets Detected With the Muon Spectrometer in ATLAS

and recommend that it be accepted as fulfilling the dissertation requirement for the Degree of Doctor of Philosophy.

kenneth johns — Date: Jul 27, 2021
kenneth johns

Elliott Cheu — Date: Jul 27, 2021
Elliott Cheu

John Rutherfoord — Date: Jul 28, 2021
John Rutherfoord

Shufang Su — Date: Jul 27, 2021
Shufang Su

Erich Varnes — Date: Aug 3, 2021
Erich Varnes

Final approval and acceptance of this dissertation is contingent upon the candidate's submission of the final copies of the dissertation to the Graduate College.

I hereby certify that I have read this dissertation prepared under my direction and recommend that it be accepted as fulfilling the dissertation requirement.

kenneth johns — Date: Jul 27, 2021
kenneth johns
Physics

ACKNOWLEDGEMENTS

During these five years at the University of Arizona, I received help from many people and I would like to say thanks to you all.

First, I want to thank my adviser, Kenneth Johns, for giving me the opportunity to involve in the experimental particle physics and continuously supporting me over the years so that I am able to finish this thesis. I also want to thank Erich Varnes and Elliott Cheu for their questions and advice in each week's group meeting, which always helped me think on a deeper level. Also, I want to thank Shufang Su and John Rutherfoord for reading this thesis and providing comments.

I would like to thank my colleagues as well. In particular, I want to thank UA post-doc, Simon Berlendis, for always patiently answering my countless questions and teaching me the skills in the particle physics analysis. I also want to thank my office mate Rachel Lindley and Billie Lubis for the help and company over the years. I want to thank Michael Schott for working together to push the analysis forward. In addition, I want to thank Matt LeBlanc, Chris Delitzsch, Maxwell Cui and Nicholas Lopez for the useful physics discussions and conversations. I want to thank the UA MMFE8 team, especially to Kade Gigliotti, Garrett Scott and Michelle Solis. Without their hard work and help, I will not be able to finish the ATLAS qualification task. I want to thank the analysis team of the University of Washington. Many thanks go to Henry Lubatti, Cristiano Alpigiani and Audrey Kvam for lots of work and discussions in the long-lived particle analysis.

I also would like to thank Gardie Lueders for solving many issues I met during my graduate studies. I want to thank Shane Smith and Amy Bai for their help on the paper work regarding traveling, funding and etc. I want to thank Mike Eklund for his technical support whenever the Tier3 server had a problem. I want to thank Sarah Jones, Ruchika Nayyar and Hannah Carson for their guidance and help when I enter the UA analysis team in my first year.

Finally, I want to thank my parents. I could not have made this far without their support.

DEDICATION

For my parents.

TABLE OF CONTENTS

TABLE OF CONTENTS – *Continued*

TABLE OF CONTENTS – *Continued*

LIST OF FIGURES

LIST OF FIGURES – *Continued*

LIST OF FIGURES – *Continued*

LIST OF FIGURES – *Continued*

LIST OF TABLES

LIST OF TABLES – *Continued*

LIST OF TABLES – *Continued*

ABSTRACT

The discovery of the Higgs boson in 2012 marked a great success of the Standard Model (SM) of particle physics. Up to now, the branching ratio of the Higgs boson to undetected particles beyond the Standard Model (BSM) is not well constrained (up to 22%). Long-lived particles (LLPs) show up in a variety of BSM theories, such as Higgs portal models. This thesis presents a search for displaced vertices from LLP decays in the ATLAS muon spectrometer (MS) using 139 fb^{-1} of proton-proton collision data at $\sqrt{s} = 13$ TeV collected by the ATLAS detector at the LHC from 2015 to 2018. The signal benchmark model of interest is a Hidden Sector scenario, where a Higgs-like boson can decay into a pair of neutral long-lived scalars. A specialized trigger is used to collect events that produce high activity in the MS. A specialized software algorithm subsequently reconstructs vertices in the MS. Background to two LLP decays producing displaced vertices in the MS are determined using a data-driven method. To extend the sensitivity of the search to a wide range of LLP proper lifetime $c\tau_s$, we employ a toy Monte Carlo method. No events are found after event selection optimized for the LLP signal. The 95% confidence level limits on the branching ratio into LLPs for the SM-like Higgs boson with 125 GeV mass are subsequently constructed. The LLP $c\tau_s$ are excluded at 95% CL from about 4 cm to 71.3 m for the branching ratio above 10% depending on mass. If the Higgs-like boson has a mass different than 125 GeV, we set the 95% CL upper limit on the LLP production cross section.

CHAPTER 1

Introduction

Particle physics studies the elementary constituents and fundamental interactions in our world. In the latter part of the 20th century, a consistent mathematical framework called the Standard Model (SM) [1, 2] was developed to describe them. The Standard Model is a gauge quantum field theory that describes the strong, weak and electromagnetic interactions between the elementary particles. During the past 50 years, from the discovery of quarks in 1970s to the discovery of the Higgs boson in 2012 [3, 4], all SM particles have been experimentally observed. With enormous amounts of precise measurements, no particles outside of the SM have been observed at the Large Hadron Collider (LHC) or other experiments.

There are several reasons why we believe the SM to be incomplete, or an approximation to some more fundamental one. Among these are the non-zero neutrino mass, hierarchy problem, strong CP problem, and lack of dark matter candidate. Many extensions of the SM have been developed in order to address some of these problems. A list of a few of these models includes minimal supersymmetric SM (MSSM) [5, 6], split supersymmetry (SUSY) [7, 8], SUSY with R-parity violation (RPV) [9], Stealth SUSY [10, 11], Hidden Valley models [12, 13], neutral naturalness theories [14, 15, 16, 17], neutrino mass theories [18, 19, 20, 21], dark matter theories [22, 23, 24] and baryogenesis [25, 26, 27].

Several of these Beyond-the-Standard Model (BSM) theories contain new, long-lived particles (LLPs) in their description [28]. A long-lived particle is defined as a fundamental particle that decays with large proper lifetime so that it has a detectable vertex some distance away from the primary vertex (PV). There are generally several theoretical mechanisms that can give rise to a long-lived particle: heavy propagator (e.g. split SUSY), small coupling between LLP and its decay products (e.g. RPV SUSY), and suppressed decay phase space (e.g. Stealth SUSY).

Depending on the lifetime and the traveling speed, an LLP can possibly decay anywhere inside the detector and leave a secondary vertex, which is also called displaced vertex. For example, in the ATLAS detector, we can search for LLPs in the inner detector (ID), calorimeter, or muon spectrometer (MS). Depending on the specific model that includes LLPs, the decay modes can be hadronic, leptonic, semileptonic or photonic. In ATLAS, a very rich spectrum of LLP search strategies is possible and listed in Figure 1.1 [29]. This analysis focuses on a search for two displaced vertices produced by LLP decays that are reconstructed with the muon spectrometer. The Hidden Sector model is used as a benchmark model against which to compare the data.

This dissertation is organized as follows. Chapter 2 gives an introduction to the theory of the Standard Model and the BSM benchmark models used in the analysis. Chapter 3 describes the LHC accelerator and the ATLAS detector. Chapter 4 summarizes the details of data and Monte Carlo samples used in the analysis. Chapter 5 describes the Run 2 trigger system of the ATLAS detector. A specialized Muon RoI Cluster Trigger used for this analysis is presented. Chapter 6 discusses the reconstruction of objects that are used in the analysis including charged particle tracks, jets, missing transverse energy, and vertices reconstructed in the muon spectrometer. Chapter 7 presents the criteria to select displaced vertices and the reconstruction efficiency for LLPs. Chapter 8 describes the strategy for selecting events that could contain LLP decays. The background estimation, lifetime extrapolation procedure and systematic uncertainties are also described. Chapter 9 presents the statistical model used to interpret the data and the upper limit cross section results. Chapter 10 gives a summary and discusses the future work to be done.

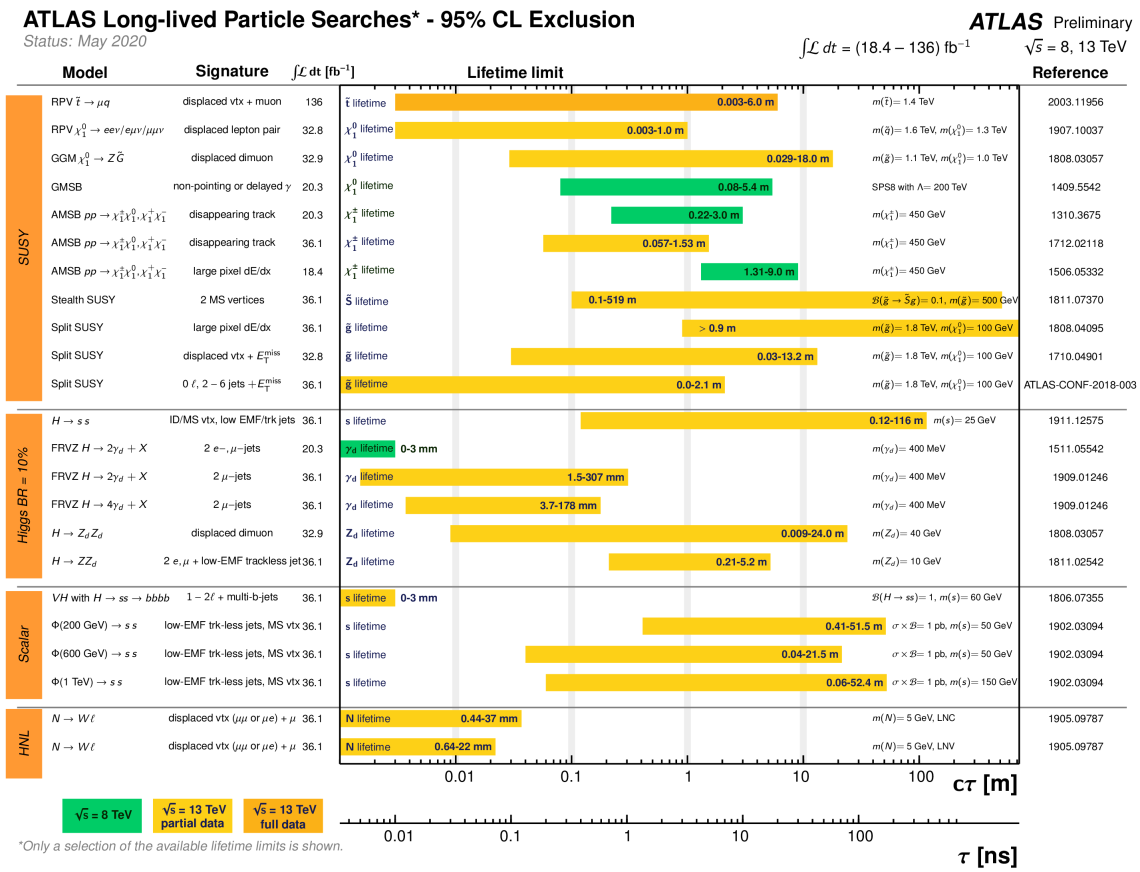

Figure 1.1: 95% CL lifetime limits from various recent LLP searches in the ATLAS experiment.

CHAPTER 2

Theories of Particle Physics

2.1 The Standard Model of Particle Physics

The Standard Model of particle physics is a $SU(3)_C \times SU(2)_L \times U(1)_Y$ gauge theory that describes the fundamental interactions. Among them, electromagnetic interaction was firstly understood by researchers. From study, people discovered that the electromagnetic interaction satisfies $U(1)$ gauge invariance and the photon is the mediator that propagates the electromagnetic interaction. In 1961, Glashow proposed a $SU(2)\times U(1)$ theoretical model that unified the electromagnetic and weak interactions [30].

In 1967 and 1968, Weinberg and Salam introduced spontaneous symmetry breaking (SSB) into this model [31, 32] and a gauge theory with Higgs mechanism [33, 34] was constructed. In 1971 and 1972, t'Hooft and Veltman proved that this theory is unitary and renormalizable [35, 36]. In 1970, Glashow, Iliopoulos and Maiani developed the GIM mechanism [37] that explains why flavor-changing neutral currents are suppressed and predicted the existence of charm quark. In 1973, Kobayashi and Maskawa extended the GIM mechanism and introduced a quark mixing matrix (Cabibbo–Kobayashi–Maskawa matrix or CKM matrix) that describes the strength of the flavor-changing weak interaction between three generation of quarks [38, 39]. The electroweak interaction is thus described by $SU(2)_L \times U(1)_Y$. The strong interaction has $SU(3)_C$ gauge symmetry and is described by the quantum chromodynamics (QCD) theory [40].

Experiments carried out over several decades tested the predictions of the Standard Model as well as searched for phenomena not associated with it. In 1974, the charm quark was discovered by two teams led by Samuel Ting at Brookhaven National Laboratory [41] and Burton Richter at the Stanford Linear Accelerator Center [42]. In 1977, the bottom quark was discovered at the Fermilab experiment by a team led by Leon M. Lederman [43]. In 1983, the W and Z bosons were discovered at CERN [44, 45, 46, 47]. In 1995, the top quark was discovered by the CDF and DØ experiments at Fermilab [48, 49]. In 2000, the direct evidence of tau neutrino interactions was found by the DONUT experiment at Fermilab [50]. In 2012, the last undiscovered SM particle Higgs boson was found at the LHC [3, 4]. This brief history review shows the huge success of the SM in explaining three of the four fundamental forces and the associated elementary particles.

2.1.1 SM Particles and Interactions

In the SM, fermions with spin-1/2 are called matter particles, i.e. leptons and quarks. The properties of these particles are summarized in Table 2.1. Charged leptons include electron, muon and tau. Neutral leptons have electron neutrino, muon neutrino and tau neutrino. SM neutrinos are massless. With the discovery of neutrino oscillation, effects have been made to extend the SM so that massive neutrinos can be included [51]. These six types of leptons are grouped in three generations. Each lepton generation has a left-handed weak isospin doublet and a right-handed weak isospin singlet.

Quarks include up quark, down quark, charm quark, strange quark, top quark and bottom quark. Similar to leptons, quarks are also grouped in three generations. Each quark generation has a left-handed weak isospin doublet and two right-handed weak isospin singlets. Unlike leptons, quarks carry an extra color charge (red, green or blue) which is related to the strong interaction.

Fermion	1st Gen.	2nd Gen.	3rd Gen.	I	I_3	Y	Q
Lepton	$\begin{pmatrix} \nu_e \\ e \end{pmatrix}_L$	$\begin{pmatrix} \nu_\mu \\ \mu \end{pmatrix}_L$	$\begin{pmatrix} \nu_\tau \\ \tau \end{pmatrix}_L$	$\frac{1}{2}$	$\begin{pmatrix} \frac{1}{2} \\ -\frac{1}{2} \end{pmatrix}$	-1	$\begin{pmatrix} 0 \\ -1 \end{pmatrix}$
	e_R	μ_R	τ_R	0	0	-2	-1
Quark	$\begin{pmatrix} u \\ d \end{pmatrix}_L$	$\begin{pmatrix} c \\ s \end{pmatrix}_L$	$\begin{pmatrix} t \\ b \end{pmatrix}_L$	$\frac{1}{2}$	$\begin{pmatrix} \frac{1}{2} \\ -\frac{1}{2} \end{pmatrix}$	$\frac{1}{3}$	$\begin{pmatrix} \frac{2}{3} \\ -\frac{1}{3} \end{pmatrix}$
	u_R	c_R	t_R	0	0	$\frac{4}{3}$	$\frac{2}{3}$
	d_R	s_R	b_R	0	0	$-\frac{2}{3}$	$-\frac{1}{3}$

Table 2.1: Three generations of SM fermions with their quantum numbers. I is weak isospin. I_3 is the third component of weak isospin. Y is hypercharge. Q is electric charge.

Fermions can interact with each other by exchanging spin-1 gauge bosons, which include the photon, W boson, Z boson and gluon. Table 2.2 lists the quantum numbers of these gauge bosons and Higgs. The electromagnetic interaction is generated by exchanging photons between charged particles. The theory that describe this interaction is quantum electrodynamics (QED). The strong and weak interactions get their names from comparing their interaction strength with electromagnetic interaction. Since the photon is massless, the effective range of the electromagnetic interaction is infinite long.

The weak interactions exists among all the fermions and is generated by the exchange of W and Z bosons. Its strength is a bit larger than that of the electromagnetic interaction. The weak interaction has several obvious features. First, the weak interaction shows different behavior for fermions with different chirality. For example, W boson only couples with left-handed fermions and their right-handed anti-fermions. The Z boson can interact with fermions with any chirality. Next, since the W and Z bosons are massive (~80 GeV), the weak interaction has a very short effective range (around 10^{-17} to 10^{-16} m). The weak interaction is the only interaction that can change the flavor of quarks. In the SM, the masses of W and Z bosons are generated through an interaction with the Higgs field, which is a spin-0 scalar field with a non-zero vacuum expectation value. This mechanism is called the Higgs mechanism and will be described later.

The strong interaction only affects particles with color charge, i.e. quarks and gluons. This interaction is mediated by the gluon, which is a massless neutral boson. The strength of the strong interaction is much larger than that of the electroweak interaction. The strength of the strong force decreases (increases) with decreasing (increasing) distance between two color charges.

Quarks and gluons do not exist in isolation. Because of the nature of the strong interaction, the separation of quarks results in the creation of new quark-antiquark pairs. This phenomena is known as color confinement and is related to the hadronization of quarks and gluons produced in collisions.

Bosons	S	I	I_3	Y	Q
γ	1	0	0	0	0
Z	1	1	0	0	0
$W^{\pm}$	1	1	±1	0	±1
g	1	0	0	0	0
H	0	$\frac{1}{2}$	$-\frac{1}{2}$	1	0

Table 2.2: SM bosons and their quantum numbers. S is spin. I is weak isospin. I_3 is the third component of weak isospin. Y is hypercharge. Q is electric charge.

2.1.2 $SU(2)_L \times U(1)_Y$ Electroweak Gauge Theory

An important element of electroweak theory is local gauge invariance. Taking $U(1)$ gauge transformation as an example, consider the Lagrangian of Dirac field $\psi(x)$,

$$\mathcal{L}_0 = i\bar{\psi}(x)\gamma^\mu \partial_\mu \psi(x) - m\bar{\psi}(x)\psi(x). \tag{2.1}$$

$\mathcal{L}_0$ is invariant under global $U(1)$ transformations

$$\psi(x) \xrightarrow{U(1)} \psi'(x) \equiv \exp\{iQ\theta\}\psi(x), \tag{2.2}$$

where θ is an arbitrary real number, Q is the electric charge. When θ becomes a local phase rather than global phase, i.e., $\theta = \theta(x)$, this Lagrangian is no longer invariant. Invariance can be regained by introducing a vector field $A_\mu(x)$, which has a corresponding gauge transformation

$$A_\mu(x) \xrightarrow{U(1)} A'_\mu(x) \equiv A_\mu(x) - \frac{1}{e}\partial_\mu\theta. \tag{2.3}$$

In addition, the original partial derivative needs to be replaced by the gauge covariant derivative,

$$D_\mu\psi(x) \equiv [\partial_\mu + ieQA_\mu(x)]\psi(x). \tag{2.4}$$

Then it is easy to verify that Lagrangian

$$\mathcal{L} \equiv i\bar{\psi}(x)\gamma^\mu D_\mu\psi(x) - m\bar{\psi}(x)\psi(x) = \mathcal{L}_0 - eQA_\mu(x)\bar{\psi}(x)\gamma^\mu\psi(x) \tag{2.5}$$

is invariant under the local $U(1)$ gauge transformation.

The last term in Equation 2.5 arises as a consequence of local gauge invariance and gives the interaction. This interaction term is the familiar QED interaction between photon and electrons. It can be seen that gauge symmetry plays a very important role in modern theories of particle physics.

In the SM electroweak gauge theory, the gauge symmetry group is

$$G \equiv SU(2)_L \times U(1)_Y. \tag{2.6}$$

Subscript L represents left-handed and Y refers to hypercharge. Their meaning will be given later. The SM Lagrangian can be separated into four parts: the gauge part, fermion part, Higgs part, and Yukawa part:

$$\mathcal{L}_{\mathrm{SM}} = \mathcal{L}_{\mathrm{gauge}} + \mathcal{L}_{\mathrm{f}} + \mathcal{L}_{\mathrm{Higgs}} + \mathcal{L}_{\mathrm{Yukawa}}. \tag{2.7}$$

$\mathcal{L}_{\text{gauge}}$ gives kinetic term and interaction terms of the gauge bosons. $\mathcal{L}_{\text{f}}$ gives kinetic term of fermion field and their interaction with gauge bosons. $\mathcal{L}_{\text{Higgs}}$ gives the kinetic and potential terms of the Higgs field and the interaction between the Higgs field and gauge bosons. $\mathcal{L}_{\text{Yukawa}}$ describes the coupling between the Higgs field and fermions.

For quarks, we introduce the notation

$$\psi_1(x) = \begin{pmatrix} u \\ d \end{pmatrix}_L, \quad \psi_2(x) = u_R, \quad \psi_3(x) = d_R, \tag{2.8}$$

where u and d represent up type and down type quarks of three generations. For leptons, we use a similar notation

$$\psi_1(x) = \begin{pmatrix} \nu_e \\ e \end{pmatrix}_L, \quad \psi_2(x) = \nu_{eR}, \quad \psi_3(x) = e_R. \tag{2.9}$$

Since there is no right-handed neutrinos, $\psi_2(x)$ can be regarded as zero. With the help of these notations, $\mathcal{L}_{\text{f}}$ can be expressed as

$$\mathcal{L}_{\text{f}} = \sum_{j=1}^{3} i\bar{\psi}_j(x)\gamma^\mu D_\mu \psi_j(x). \tag{2.10}$$

Fermion fields have the following $SU(2)_L \times U(1)_Y$ local gauge transformation

$$\begin{aligned} \psi_1(x) &\xrightarrow{G} \psi_1'(x) \equiv \exp\{i\frac{Y_1}{2}\beta(x)\}U_L\psi_1(x), \\ \psi_2(x) &\xrightarrow{G} \psi_2'(x) \equiv \exp\{i\frac{Y_2}{2}\beta(x)\}\psi_2(x), \\ \psi_3(x) &\xrightarrow{G} \psi_3'(x) \equiv \exp\{i\frac{Y_3}{2}\beta(x)\}\psi_3(x). \end{aligned} \tag{2.11}$$

U_L is the $SU(2)_L$ transformation matrix for doublet $\psi_1(x)$

$$U_L \equiv \exp\{i\frac{\sigma_i}{2}\alpha^i(x)\} \quad (i = 1, 2, 3), \tag{2.12}$$

where σ_i is the Pauli matrix and Y_i is called hypercharge. It is worth noting that there is no mass term in (2.10). $\psi(x)$ has to be massless, otherwise an additional term of $m(\bar{\psi}_L\psi_R + \bar{\psi}_R\psi_L)$ will be introduced and thus breaks the gauge invariance.

Because there are four gauge parameters $\alpha^i(x)$ and $\beta(x)$, four corresponding gauge fields need to be introduced into the covariant derivative D_μ. These are denoted as

$W_\mu^i(x)$ $(i = 1, 2, 3)$ and $B_\mu(x)$:

$$\begin{aligned} D_\mu \psi_1(x) &\equiv [\partial_\mu + ig\widetilde{W}_\mu(x) + ig'\frac{Y_1}{2}B_\mu(x)]\psi_1(x), \\ D_\mu \psi_2(x) &\equiv [\partial_\mu + ig'\frac{Y_2}{2}B_\mu(x)]\psi_2(x), \\ D_\mu \psi_3(x) &\equiv [\partial_\mu + ig'\frac{Y_3}{2}B_\mu(x)]\psi_3(x), \end{aligned} \tag{2.13}$$

where

$$\widetilde{W}_\mu(x) \equiv I_i W_\mu^i(x) = \frac{\sigma_i}{2} W_\mu^i(x), \tag{2.14}$$

and $I_i = \frac{\sigma_i}{2}$ is the SU(2) weak isospin generator under fundamental representation. The $U(1)_Y$ gauge field B_μ and $SU(2)_L$ gauge fields W_μ^i $(i = 1, 2, 3)$ have following gauge transformation

$$B_\mu(x) \xrightarrow{G} B'_\mu(x) \equiv B_\mu(x) - \frac{1}{g'}\partial_\mu \beta(x), \tag{2.15}$$

$$\widetilde{W}_\mu \xrightarrow{G} \widetilde{W}'_\mu \equiv U_L(x)\widetilde{W}_\mu U_L^\dagger(x) + \frac{i}{g}\partial_\mu U_L(x) U_L^\dagger(x). \tag{2.16}$$

It may be noticed that the transformation of B_μ is same as the transformation of a photon field (2.3) in QED, but B_μ itself is not the electromagnetic vector potential.

In order to establish the kinetic terms of these gauge fields, it is convenient to define the gauge field strength tensor

$$B_{\mu\nu} \equiv \partial_\mu B_\nu - \partial_\nu B_\mu, \tag{2.17}$$

$$\widetilde{W}_{\mu\nu} \equiv -\frac{i}{g}[(\partial_\mu + ig\widetilde{W}_\mu), (\partial_\nu + ig\widetilde{W}_\nu)] = \partial_\mu \widetilde{W}_\nu - \partial_\nu \widetilde{W}_\mu + ig[\widetilde{W}_\mu, \widetilde{W}_\nu], \tag{2.18}$$

$$\widetilde{W}_{\mu\nu} \equiv \frac{\sigma_i}{2} W_{\mu\nu}^i, \quad W_{\mu\nu}^i = \partial_\mu W_\nu^i - \partial_\nu W_\mu^i - g\epsilon^{ijk} W_\mu^j W_\nu^k. \tag{2.19}$$

where ϵ^{ijk} is the Levi-Civita totally antisymmetric tensor. $B_{\mu\nu}$ is invariant under $SU(2)_L \times U(1)_Y$, but $\widetilde{W}_{\mu\nu}$ has following transformation:

$$\widetilde{W}_{\mu\nu} \xrightarrow{G} U_L \widetilde{W}_{\mu\nu} U_L^\dagger. \tag{2.20}$$

The kinetic term of the gauge fields then follows as

$$\begin{aligned} \mathcal{L}_{\text{gauge}} &= -\frac{1}{4}B_{\mu\nu}B^{\mu\nu} - \frac{1}{2}\mathrm{Tr}[\widetilde{W}_{\mu\nu}\widetilde{W}^{\mu\nu}] \\ &= -\frac{1}{4}B_{\mu\nu}B^{\mu\nu} - \frac{1}{4}W_{\mu\nu}^i W_i^{\mu\nu}. \end{aligned} \tag{2.21}$$

Since $W^i_{\mu\nu}$ contains a quadratic term of W^i_μ, $\mathcal{L}_{\text{gauge}}$ contains terms that describe the triple and quartic couplings of the gauge bosons. Gauge bosons remain massless in $\mathcal{L}_{\text{gauge}}$, because the introduction of a mass term will destroy the gauge invariance. The interaction terms between fermions and gauge bosons are contained in Equation 2.10. If we expand the Lagrangian, we will be able to find their interaction term

$$\mathcal{L}_{\text{f}} \rightarrow -g\bar{\psi}_1\gamma^\mu\widetilde{W}_\mu\psi_1 - g'B_\mu\sum_{j=1}^{3}\frac{y_j}{2}\bar{\psi}_j\gamma^\mu\psi_j, \tag{2.22}$$

where

$$\widetilde{W}_\mu = \frac{\sigma^i}{2}W^i_\mu = \frac{1}{2}\begin{pmatrix} W^3_\mu & \sqrt{2}W^+_\mu \\ \sqrt{2}W^-_\mu & -W^3_\mu \end{pmatrix}, \tag{2.23}$$

$$W^-_\mu \equiv (W^1_\mu + iW^2_\mu)/\sqrt{2}, \quad W^+_\mu \equiv (W^1_\mu - iW^2_\mu)/\sqrt{2}. \tag{2.24}$$

The W^+_μ and W^-_μ represent the two charged states of the W boson. The charged current interactions between quarks or leptons and the W boson follows as

$$\mathcal{L}_{\text{CC}} = -\frac{g}{2\sqrt{2}}\{W^+_\mu[\bar{u}\gamma^\mu(1-\gamma_5)d + \bar{\nu}_e\gamma^\mu(1-\gamma_5)e] + \text{h.c.}\}. \tag{2.25}$$

The photon γ and Z boson are realized through mixing between W^3_μ and B_μ:

$$\begin{pmatrix} Z_\mu \\ A_\mu \end{pmatrix} = \begin{pmatrix} \cos\theta_W & -\sin\theta_W \\ \sin\theta_W & \cos\theta_W \end{pmatrix}\begin{pmatrix} W^3_\mu \\ B_\mu \end{pmatrix}, \tag{2.26}$$

where θ_W is called the weak mixing angle. Then, using A_μ and Z_μ, the neutral current interaction can be expressed as

$$\begin{aligned}\mathcal{L}_{\text{NC}} = \; & - \sum_j \bar{\psi}_j\gamma^\mu\{A_\mu[gI_{3,j}\sin\theta_W + g'\frac{Y_j}{2}\cos\theta_W] \\ & + Z_\mu[gI_{3,j}\cos\theta_W - g'\frac{Y_j}{2}\sin\theta_W]\}\psi_j,\end{aligned} \tag{2.27}$$

where $I_{3,j}$ is the 3rd component of weak isospin of fermion field ψ_j. The following relations can also be found

$$g\sin\theta_W = g'\cos\theta_W = e, \quad \frac{Y}{2} = Q - I_3. \tag{2.28}$$

The first equation connects the $SU(2)_L$ and $U(1)_Y$ coupling constants with the electromagnetic coupling constant, which realizes the unification of the electromagnetic interaction and the weak interaction. The second equation gives us the relation between hypercharge, electric charge and weak isospin.

To find the interaction Lagrangian between $W^{\pm}$, Z and γ, one can replace the W^i_μ and B_μ with $W^{\pm}_\mu$, Z_μ and A_μ in (2.21). The Lagrangian for triple gauge boson couplings is

$$\begin{aligned}\mathcal{L}_3 \;=\;& ie\cot\theta_W\{(\partial^\mu W^{-\nu} - \partial^\nu W^{-\mu})W^+_\mu Z_\nu - (\partial^\mu W^{+\nu} - \partial^\nu W^{+\mu})W^-_\mu Z_\nu \\ & + W^-_\mu W^+_\nu(\partial^\mu Z^\nu - \partial^\nu Z^\mu)\} + ie\{(\partial^\mu W^{-\nu} - \partial^\nu W^{-\mu})W^+_\mu A_\nu \\ & -(\partial^\mu W^{+\nu} - \partial^\nu W^{+\mu})W^-_\mu A_\nu + W^-_\mu W^+_\nu(\partial^\mu A^\nu - \partial^\nu A^\mu)\}. \end{aligned} \tag{2.29}$$

The Lagrangian for interactions among four gauge bosons is

$$\begin{aligned}\mathcal{L}_4 \;=\;& -\frac{e^2}{2\sin^2\theta_W}\{(W^+_\mu W^{-\mu})^2 - W^+_\mu W^{+\mu} W^-_\nu W^{-\nu}\} \\ & -e^2\cot^2\theta_W\{W^+_\mu W^{-\mu} Z_\nu Z^\nu - W^+_\mu Z^\mu W_\nu Z^\nu\} \\ & -e^2\cot\theta_W\{2W^+_\mu W^{-\mu} Z_\nu A^\nu - W^+_\mu Z^\mu W^-_\nu A^\nu - W^+_\mu A^\mu W^-_\nu Z^\nu\} \\ & -e^2\{W^+_\mu W^{-\mu} A_\nu A^\nu - W^+_\mu A^\mu W^-_\nu A^\nu\}. \end{aligned} \tag{2.30}$$

2.1.3 Higgs Mechanism

The theory discussed above corresponds to massless W and Z bosons contradicting nature. In order to solve this problem, a $SU(2)_L$ doublet constructed by complex scalar fields is introduced

$$\phi = \begin{pmatrix} \phi^+ \\ \phi^0 \end{pmatrix}. \tag{2.31}$$

It has hypercharge $Y = 1$. ϕ has a $SU(2)_L \times U(1)_Y$ invariant Lagrangian

$$\mathcal{L}_{\text{Higgs}} = (D_\mu\phi)^\dagger(D^\mu\phi) - V(\phi), V(\phi) = \mu^2\phi^\dagger\phi + \lambda(\phi^\dagger\phi)^2, \tag{2.32}$$

where $\mu^2 < 0$ and the potential $V(\phi)$ has non-zero minimum value

$$|\langle 0|\phi^0|0\rangle| = \sqrt{\frac{-\mu^2}{\lambda}} \equiv \frac{\nu}{\sqrt{2}}, \tag{2.33}$$

Since all points with same $\phi^\dagger\phi$ are gauge equivalent, we can choose to write the ϕ field in the unitary gauge

$$\phi(x) = \begin{pmatrix} 0 \\ \frac{\nu + H(x)}{\sqrt{2}} \end{pmatrix}. \tag{2.34}$$

$H(x)$ is a real scalar field with zero vacuum expectation value. It is called the Higgs field. Using (2.24) and (2.26), the kinematic term of $\mathcal{L}_{\text{Higgs}}$ can be written as

$$(D_\mu\phi)^\dagger D^\mu\phi = \frac{1}{2}\partial_\mu H\partial^\mu H + (\nu + H)^2(\frac{g^2}{4}W_\mu^+ W^{-\mu} + \frac{g^2}{8\cos^2\theta_W}Z_\mu Z^\mu). \quad (2.35)$$

In this equation, one sees from the quadratic terms of the W and Z that these particles have obtained a mass. The masses of $W^\pm$ and Z can be expressed as

$$M_W = \frac{1}{2}\nu g, \quad M_Z = \frac{1}{2\cos\theta_W}\nu g = \frac{\nu\sqrt{g^2 + g'^2}}{2}. \quad (2.36)$$

The quadratic term of the Higgs field shows up in the potential part, which is given by

$$V(\phi) = -\frac{1}{4}\lambda\nu^4 + M_H^2(\frac{1}{2}H^2 + \frac{1}{2\nu}H^3 + \frac{1}{8\nu^2}H^4), \quad (2.37)$$

where M_H is mass of the Higgs. Its expression is

$$M_H = \sqrt{2\lambda}\nu. \quad (2.38)$$

Using (2.36) and (2.38), $\mathcal{L}_{\text{Higgs}}$ can have the following expression

$$\begin{aligned}\mathcal{L}_{\text{Higgs}} \quad = \quad & \frac{1}{2}\partial_\mu H\partial^\mu H + \frac{1}{4}\lambda\nu^4 + M_W^2 W_\mu^+ W^{-\mu}(1 + \frac{2}{\nu} + \frac{H^2}{\nu^2}) \\ & + \frac{1}{2}M_Z^2 Z_\mu Z^\mu(1 + \frac{2}{\nu} + \frac{H^2}{\nu^2}) - \frac{1}{2}M_H^2 H^2 - \frac{M_H^2}{2\nu}H^3 - \frac{M_H^2}{8\nu^2}H^4. \quad (2.39)\end{aligned}$$

In the SM, the masses of fermions are produced through the introduction of a Yukawa term between the Higgs field and fermions. The Lagrangian for the Yukawa coupling is

$$\mathcal{L}_{\text{Yukawa}} = -\lambda_u(\bar{u},\ \bar{d})_L\phi d_R - \lambda_d(\bar{u},\ \bar{d})_L\phi^c u_R - \lambda_e(\bar{\nu_e},\ \bar{e})_L\phi e_R + \text{h.c.}, \quad (2.40)$$

where $\phi^c = i\sigma_2\phi$. Here u, d and e represent quarks and leptons of three generations. Using the unitary gauge, $\mathcal{L}_{\text{Yukawa}}$ can be simplified as

$$\mathcal{L}_{\text{Yukawa}} = -\frac{\nu + H}{\sqrt{2}}(\lambda_d\bar{d}_L d_R + \lambda_u\bar{u_L}u_R + \lambda_e\bar{e_L}e_R) + h.c.. \quad (2.41)$$

For leptons, the mass of each is given by

$$m_e = \frac{\lambda_e\nu}{\sqrt{2}}. \quad (2.42)$$

The Standard Model provides no prediction about the strength of Yukawa coupling. Thus the lepton masses must be determined experimentally. Unlike the lepton mass, the expressions for the quark masses cannot be extracted directly from the Lagrangian, since coefficients $\nu\lambda_d$ and $\nu\lambda_u$ construct non-diagonal matrix. This means the u and d quarks are in flavor eigenstates, not mass eigenstates. In order to obtain the quark mass eigenstates, the coefficients of the quark quadratic terms must be diagnolized.

2.1.4 $SU(3)_C$ Quantum Chromodynamics

The gauge theory of the Quantum Chromodynamics is $SU(3)_C$. For a quark field with color α and flavor f, q_f^α, its $SU(3)_C$ transformation is

$$q_f^\alpha \to (q_f^\alpha)' = U^\alpha_\beta q_f^\beta, \tag{2.43}$$

where U is the local transformation matrix and given by

$$U = \exp\{i\frac{\lambda^a}{2}\theta_a(x)\}. \tag{2.44}$$

The matrices lambda $\frac{\lambda^a}{2}$ $(a = 1, 2, ..., 8)$ are the eight generators of $SU(3)_C$ in the fundamental representation. The λ^α are named the Gell-Mann matrices. The λ^α is traceless and satisfy the commutation relations

$$[\frac{\lambda_a}{2}, \frac{\lambda_b}{2}] = if^{abc}\frac{\lambda_c}{2}, \tag{2.45}$$

where f^{abc} is the structure constant. It is real and totally antisymmetric. As for the electroweak theory, we introduce a gauge covariant derivative to ensure local gauge invariance. There are now eight independent gauge parameters, so in the covariant derivative there need to be eight unique gauge fields $G_a^\mu(x)$ $(a = 1, 2, ..., 8)$. The gauge covariant derivative is given by

$$D_\mu q_f \equiv [\partial_\mu + ig_s\frac{\lambda^a}{2}G^a_\mu(x)]q_f \equiv [\partial_\mu + ig_s G_\mu(x)]q_f. \tag{2.46}$$

The transformations of the $G_a^\mu(x)$ need to be

$$G_\mu \to (G_\mu)' = UG_\mu U^\dagger + \frac{i}{g_s}(\partial_\mu U)U^\dagger, \tag{2.47}$$

such that $D_\mu q_f$ and q_f transform in the same way.

The gauge invariant kinetic term is added as in the electroweak theory using a field strength tensor

$$\begin{aligned} G_{\mu\nu}(x) &\equiv -\frac{i}{g_s}[D_\mu,\ D_\nu] = \partial_\mu G_\nu - \partial_\nu G_\mu + ig_s[G_\mu,\ G_\nu] \equiv \frac{\lambda^a}{2} G^a_{\mu\nu}(x), \\ G^a_{\mu\nu}(x) &= \partial_\mu G^a_\nu - \partial_\nu G^a_\mu - g_s f^{abc} G^b_\mu G^c_\nu. \end{aligned} \tag{2.48}$$

It is different from the electromagnetic field tensor in that the third term contributes to the gluon self interaction while photon field has no self interaction. Under a $SU(3)_C$ gauge transformation,

$$G_{\mu\nu} \to (G_{\mu\nu})' = UG_{\mu\nu}U^\dagger, \tag{2.49}$$

and one can show that $\mathrm{Tr}(G^{\mu\nu}G_{\mu\nu}) = \frac{1}{2}G^{a,\mu\nu}G^a_{\mu\nu}$ is invariant. The final gauge invariant Lagrangian for QCD is thus

$$\mathcal{L}_{\mathrm{QCD}} = -\frac{1}{4}G^{a,\mu\nu}G^a_{\mu\nu} + \sum_f \bar{q}_f(i\gamma^\mu D_\mu - m_f)q_f. \tag{2.50}$$

A gluon mass term is forbidden since it would break the gauge symmetry. Expanding $\mathcal{L}_{\mathrm{QCD}}$ shows the quark and gluon interactions

$$\begin{aligned} \mathcal{L}_{\mathrm{QCD}} &= -\frac{1}{4}(\partial^\mu G^{a,\nu} - \partial^\nu G^{a,\mu})(\partial_\mu G^a_\nu - \partial_\nu G^a_\mu) + \sum_f \bar{q}^\alpha_f(i\gamma^\mu\partial_\mu - m_f)q^\alpha_f \\ &\quad - g_s G^\mu_a \sum_f \bar{q}^\alpha_f \gamma_\mu (\frac{\lambda^a}{2})_{\alpha\beta} q^\beta_f \\ &\quad + \frac{g_s}{2} f^{abc}(\partial^\mu G^{a,\nu} - \partial^\nu G^{a,\mu})G^b_\mu G^c_\nu - \frac{g_s^2}{4} f^{abc} f_{ade} G^{b,\mu} G^{c,\nu} G^d_\mu G^e_\nu. \end{aligned} \tag{2.51}$$

The first line in the above Lagrangian is the kinetic part of quark field and gluon field. The second line describes the interaction between quark and gluon. The third line are three-gluon and four-gluon self-interaction terms. The QCD coupling g_s decreases as the energy scale increases and vise versa. This is a property called asymptotic freedom. At low energy scale, QCD interactions cannot be calculated perturbatively. In this case, other approaches such as Lattice QCD are needed [52].

2.1.5 Parton Distribution Function

As mentioned in the previous section, due to color confinement, quarks cannot exist in isolation. They will bind together and form a hadronic state. For example, the bound state of two up quarks and one down quark is the well-known proton and the quantum numbers of the protons are given by those of the valence quarks.

In addition to valence quarks, hadrons are also composed of gluons and quark-antiquark pairs. The gluons arise as they mediate the strong forces that bind quarks together. The gluons can split into virtual quark-antiquark pairs. These virtual quarks are called sea quarks. Sea quarks are extremely unstable and as a result they will annihilate back into gluons. At any time, there are an enormous amount of creations and annihilation of sea quarks happening inside a proton.

Valence quarks, sea quarks and gluons are called partons, and they all could take part in the interaction when two protons collide with each other. According to the QCD factorization theorem [53], the inclusive cross section of a proton-proton collision can be written as

$$\sigma(pp \to A) = \sum_{i,j} \int f_{q_i}(x_i, Q^2) f_{q_j}(x_j, Q^2) \hat{\sigma}(q_i q_j \to A) dx_i dx_j \tag{2.52}$$

The functions $f_{q_i}(x_i, Q^2)$ are the parton distribution functions (PDFs). The quantity $f_{q_i}(x_i, Q^2)dx_i$ gives the probability that a proton q_i comes from a proton and carries a fraction x_i of the proton's momentum. Here Q is the energy scale of the hard interaction and $\hat{\sigma}$ is the cross section at parton level. This factorization is correct up to a small correction: $\mathcal{O}(\frac{\Lambda_{QCD}}{Q})$, where Λ_{QCD} is the scale at which non-perturbative QCD effect takes over. Therefore, Q has to be large to ensure the correctness of the factorization formalism.

Since the PDFs represent the long-distance physics, they can not be calculated in QCD perturbation theory. There are generally two ways to obtain the PDFs, either experimentally or using lattice gauge theory. The former is much more common. The experimental determination begins by first parameterizing the PDFs at low energy scale by using either assumptions on the analytical form or the neural-net technology. Next a wide variety of experimental data, especially deep inelastic scattering data, are used to fit the PDFs. Figure 2.1 shows the PDF distributions at two different Q^2 values given by NNPDF group [54]. One observes that the valence quarks carry the largest fraction of momentum and the gluons the least fraction. Several groups prepare and continually update the PDFs such as CTEQ [55], MSTW [56] and HERAPDF [57].

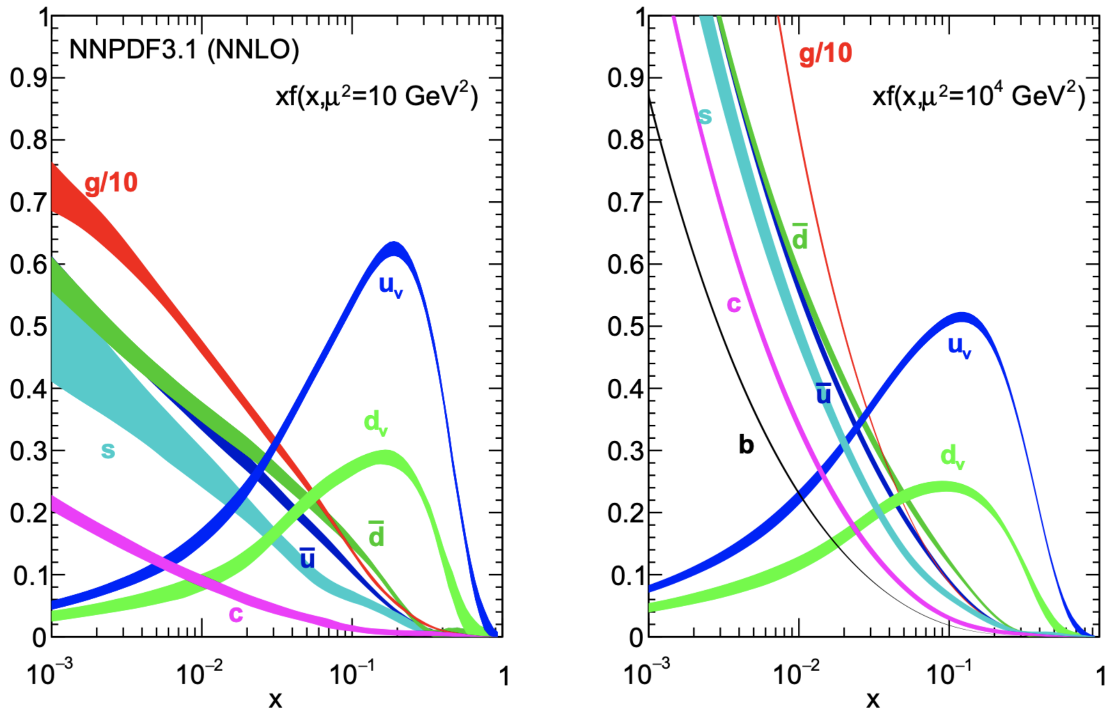

Figure 2.1: The NNPDF3.1 NNLO PDFs as a function of x evaluated at two different energy scales.

2.1.6 Shortcomings of the Standard Model

In the past few decades, although the Standard Model has achieved a great success in precisely predicting a huge range of SM measurements, there are several reasons why the SM is theoretically unsatisfactory. A few of the SM shortcomings are listed here.

- Theoretical problems of the Standard Model

  1) In the Standard Model, there are 19 free parameters: 12 mass parameters of quarks, charged leptons, weak gauge bosons and the Higgs boson, three gauge coupling constants, three mixing angles and a CP-violating phase of the CKM matrix. The Standard Model itself cannot predict the values of these parameters. Besides of this, it also cannot explain why there are three generations of quarks and leptons, why the right-handed neutrinos don't exist, and why the mass differences among these fermions are so large.

  2) The Standard Model is not able to unify the strong interaction with the electroweak interactions. In order to achieve this goal, we need a theory at

energy scale of about 10^{16} GeV, and the symmetry groups of this theory can spontaneously break to the SM symmetry groups at low energy. This kind of theory is called the Grand Unified Theory (GUT) [58, 59]. The Standard Model also cannot describe the gravitational effects. It has been proven that massless spin-2 particles are needed to generate the effect from general relativity [60]. But there is no spin-2 particle in the Standard Model.

3) The Standard Model can't answer why the electroweak energy scale, which is characterized by the vacuum expectation value of the Higgs field $\nu(\simeq 246$ GeV) is far less than the Plank scale ($\sim 10^{19}$ GeV). This is called the hierarchy problem.

Because the Higgs is a spin-0 scalar, in calculating the mass correction as shown in Figure 2.2 [61], a quadratic divergence from integral $\int d^4k(k^2 - m^2)^{-1} \sim \Lambda^2$ will appear. This arises from three contributions: fermion loop (especially the top loop $-\frac{3}{8\pi^2}\lambda_t^2\Lambda^2$), gauge loops ($\frac{1}{16\pi^2}g^2\Lambda^2$) and a self-interaction ($\frac{1}{16\pi^2}\lambda^2\Lambda^2$). For a Higgs mass of 125 GeV, Λ has to be around $\mathcal{O}(1$ TeV), which is close to the electroweak scale. Furthermore, if we want to unify gravity with the other three interactions, Λ needs to be at the Plank scale.

Apparently, in this case, the one-loop mass correction is way larger than the renormalized mass ($m_{ren} = m_{bare} - m_{correction}$). To obtain a Higgs mass at electroweak scale, the model parameters have to be tuned very carefully, which is a very unnatural operation. This is called the Fine-Tuning problem. Several theories have been proposed to overcome this problem including Supersymmetry, Large Extra Dimension [62], and the Composite Higgs model [63].

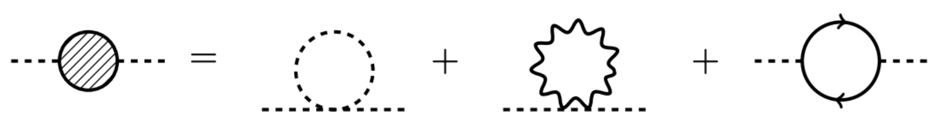

Figure 2.2: Correction on Higgs mass at one-loop level.

- Phenomena that can't be explained by the Standard Model

  1) In recent years, neutrino oscillations have been observed by many experiments [64, 65, 66, 67, 68]. Neutrino oscillations represent a flavor-changing process among neutrinos and reveal the fact that neutrinos must have non-zero mass. The mass eigenstates are mixed with the flavor eigenstates described in the

Standard Model. The origin of the neutrino mass cannot be explained by the Higgs Mechanism.

2) The existence of dark matter is another phenomenon that can't be explained by the Standard Model. Dark matter does not involve in any electroweak or strong interactions and its mass could be much larger than that of the SM particles. There is much experimental evidence for dark matter [69]. The SM has no answer as to the origin of dark matter.

3) The Standard Model cannot explain the matter–antimatter asymmetry problem. The measured antiproton-to-proton flux ratio in cosmic rays is approximately 10^{-4} [70] nowadays. A baryon abundance parameter, n_B/n_γ, is used to estimate the baryon asymmetry of the universe, where n_B is the number of baryons and n_γ represents the number of cosmic microwave background photons. It is measured with a value $\sim 10^{-10}$ [71, 72]. For this asymmetry to occur, a much larger value of CP violation must be present. In the SM, the CP violation can be introduced by a complex phase in the CKM matrix. A non-zero phase can give rise to different rates for a particle process and its corresponding antiparticle process and thus lead to the matter asymmetry. However, the measured CP violating phase [73, 74] is too small to account for that large imbalance between protons and antiprotons.

4) Another question for the SM is why no CP violation occurs in the strong interaction. This is called the strong CP problem. The QCD Lagrangian allows the existence of a CP-violating term. However, the contribution from this term is constrained experimentally to be negligible [75, 76].

2.2 Beyond the Standard Model Physics

2.2.1 Hidden Sector Model

Hidden sectors generally refer to particles that do not couple to SM particles via SM gauge interactions. They do not carry any SM charge, therefore they are undetectable. However, hidden sectors can be connected to the Standard Model via small effective couplings called portals. In this analysis, the focus is on the Higgs portal where a Higgs boson can decay to non-SM particles. According to the ATLAS and CMS results on the branching ratio of the Higgs boson, there is still room for the Higgs boson to decay into BSM particles. The upper limit of Higgs branching ratio into undetected particles is about 22% [77, 78], making this scenario attractive.

A simple model that interprets the coupling between the Higgs boson and long-lived hidden sectors [79]. In this model, besides the standard model groups, another $U(1)_{hid}$ group is introduced. The gauge sector of this extra $U(1)_{hid}$ group only couples to the Standard Model through the kinetic mixing with the $U(1)_Y$ hypercharge gauge boson. This model also assumes there exists a hidden scalar Φ with non-zero vacuum expectation value and thus can break the $U(1)_{hid}$ symmetry. The Higgs Lagrangian under this consideration is written as

$$\mathcal{L}_{\text{Higgs}} = |D_\mu \phi|^2 + |D_\mu \Phi|^2 + \mu^2 |\phi|^2 + m_\Phi^2 |\Phi|^2 - \lambda |\phi|^4 - \rho |\Phi|^4 + \eta |\phi|^2 |\Phi|^2, \quad (2.53)$$

where ϕ is the SM Higgs doublet defined in (2.31) and Φ is a $SU(2)_L$ singlet. After diagonalizing the mass matrix, two physical states exist after symmetry breaking, the Higgs-like boson H and a hidden scalar S. From the last term $\eta|\phi|^2|\Phi|^2$ of the Lagrangian, we can get a three-body interaction between the H and two S scalars. This indicates a hidden sector pair production from the Higgs portal. The hidden sector S can decay to a fermion-antifermion pair via Yukawa coupling. Since the coupling between H and S is small, S could have a relatively long lifetime. At the LHC, we can thus look for displaced jets created from the decay of these long-lived hidden scalars. Figure 2.3 shows the Feynman diagram for the displaced jets production.

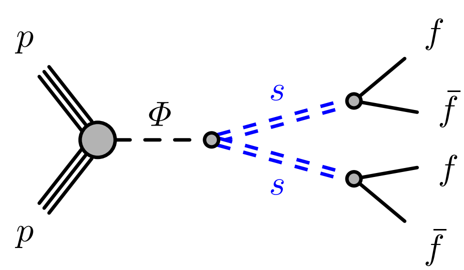

Figure 2.3: Feynman diagram for the Higgs decaying into a hidden scalar pair.

2.2.2 Baryogenesis

Several baryongenesis mechanisms are dedicated to explaining the matter asymmetry in our universe [25, 26, 27]. As a benchmark model, we focus on the baryogenesis that is triggered by the out-of-equilibrium decay of a weak-scale particle χ [80]. This model is interesting because χ is a meta-stable weakly interacting massive particle (WIMP) that is accessible at the LHC energies and could have a macroscopic decay length within the ATLAS detector.

In this model, in the early universe, χ is in thermal equilibrium with the SM matter and anti-matter. As the universe cools, the SM particles eventually do not have enough energy to create heavy χ particles. As the rate of expansion of the universe increases, χ particles freeze-out and their annihilation ceases. After freeze-out, the χ decays via baryon- or lepton-number-violating interactions. In the presence of CP violation, this leads to baryon asymmetry.

In our benchmark model, we consider χ to be a SM gauge-singlet field. The production mechanism satisfies the Z_2 symmetry, which implies that they are produced in pairs at the LHC. The lowest dimension operator coupling a singlet χ to the SM is the Higgs portal. The simplest theoretical realization is the Yukawa coupling of a scalar and a pair of χ, where the scalar mixes with the SM Higgs. For the production via the Higgs portal, we can study two different regions. One is the on-shell region where χ is produced from an on-shell Higgs ($m_\chi < m_H/2$). In this region, we can expect a copious cross section, which is proportional to the effective coupling between the Higgs and χ pair. In this case, a strong constraint on the branching ratio of this Higgs exotic decay can be set. The other region is the off-shell region ($m_\chi > m_H/2$), where the cross section falls rapidly with increasing m_χ. The sensitivity of this kind of signal is not expected to be high. Since the displaced vertex search has a feature of low background, it is still interesting to study this region with the full Run 2 luminosity at the LHC.

The decay of χ is mediated by Z_2-breaking interactions. This decay can violate the lepton or baryon number and generate baryogenesis. The lowest-dimensional operator of such interaction is the coupling between a χ and three SM fermions. Figure 2.4 shows the Feynman diagram of this baryogenesis process via the Higgs portal.

The searching result for this model is not presented in the thesis. It will be added in the combined one-vertex and two-vertex search.

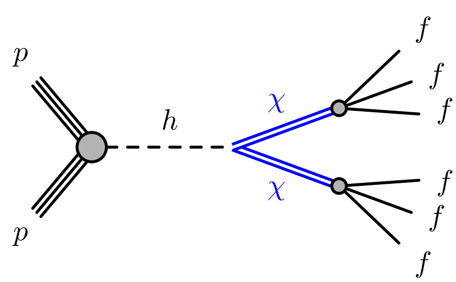

Figure 2.4: Feynman diagram for the baryogenesis process via the Higgs portal.

CHAPTER 3

The Large Hadron Collider and ATLAS Detector

3.1 The Large Hadron Collider

3.1.1 Overview

The Large Hadron Collider (LHC), located at the France–Switzerland border near Geneva, is now the largest proton-proton collider. It uses the 27 km tunnel from the Large Electron-Positron (LEP) collider. The LHC is designed to provide collisions with a maximum $\sqrt{s}$ = 14 TeV and started its beam commissioning in 2008. In November 2009, first collisions were achieved at $\sqrt{s}$ = 900 GeV [81]. On March 2010, collisions were achieved at $\sqrt{s}$ = 7 TeV which was about 3.5 times higher than the energy record at that time, and marked the beginning of the LHC physics program. From April 2015, the LHC started to operate at $\sqrt{s}$ = 13 TeV until the end of 2018 when the Long Shutdown 2 (LS2) took place. The period is called Run 2 and data collected during that period are used in this analysis.

Figure 3.1 shows the LHC accelerator chain [82] that produces a proton beam with 6.5 TeV energy. The protons are extracted from a bottle of hydrogen gas by stripping the electrons from the hydrogen atoms in an electric field. The protons then enter the Linear accelerator 2 (Linac 2) which uses radiofrequency (RF) cavities to accelerate the protons to the energy of 50 MeV. The proton beam is next injected to the Proton Synchrotron Booster (PSB) and accelerated to 1.4 GeV. Afterwards, the beam enters the Proton Synchrotron (PS), which further accelerates the beam to 25 GeV. Protons are then sent to the Super Proton Synchrotron (SPS), where they reach an energy of 450 GeV. Finally, protons are injected into the two beam pipes of the LHC, where one beam circulates clockwise and the other beam circulates counterclockwise. The beams will reach their maximum energy of 6.5 TeV.

The LHC also collides lead ions for some period per year. The lead ions follow a different accelerator chain which is Linac 3, the Low Energy Ion Ring (LEIR), the PS and the SPS.

The LHC uses proton-proton (pp) collision rather than electron-positron or proton-antiproton ($p\bar{p}$) collisions for several reasons. First, the proton beam induces much

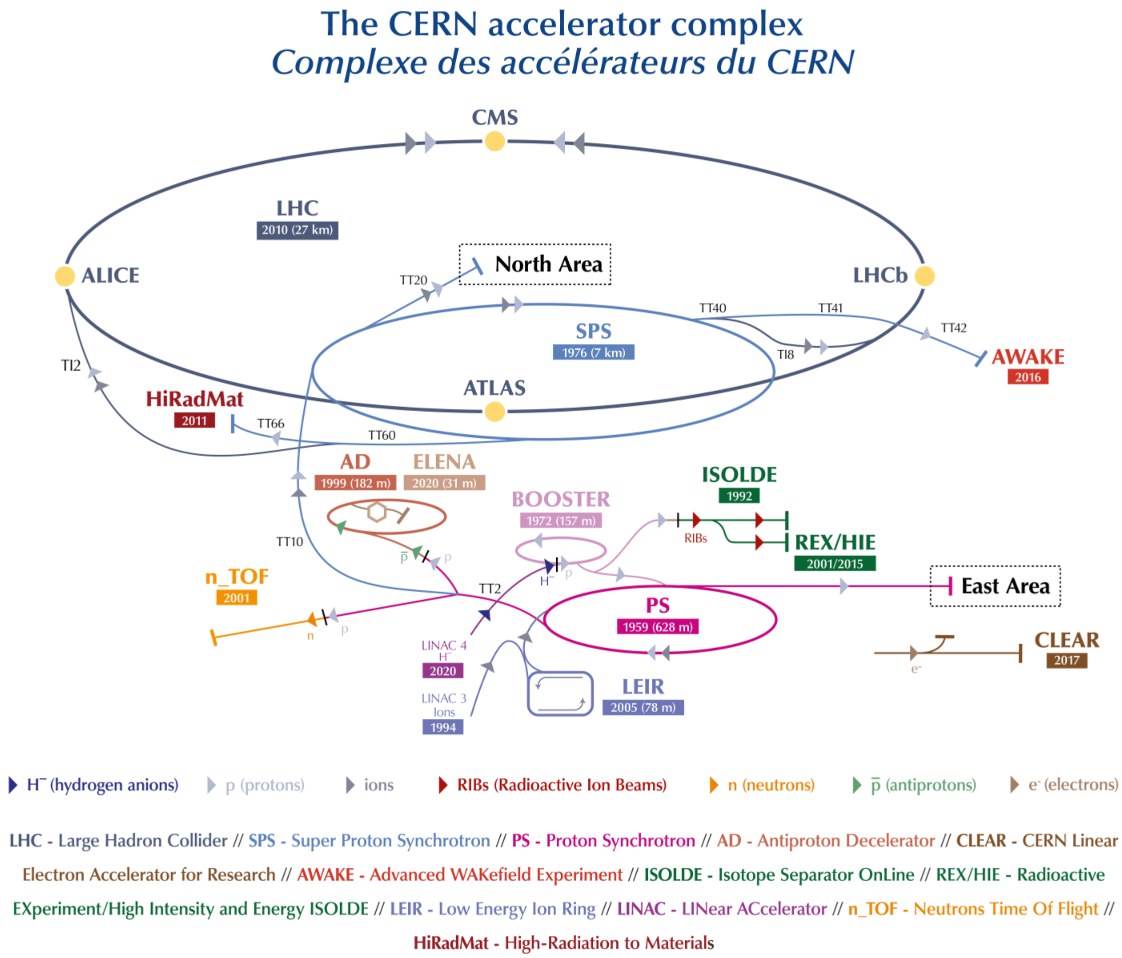

Figure 3.1: The LHC accelerator chain.

less synchrotron radiation than the lepton beam used in the LEP. When charged particles traverse perpendicular magnetic fields, they radiate photons and lose energy. The energy loss is proportional to the fourth power of the relativistic factor (γ^4). Since the proton is much less boosted than electron at the same beam energy, the synchrotron radiation losses of protons are much lower ($\sim 8 \times 10^{-14}$) than that of electrons [83]. Second, the LHC does not use antiprotons like the Tevatron because of the high luminosity requirement. Antiproton is very hard to produce. For example, in the Tevatron, antiprotons are made from the collision between 120 GeV protons and a Nickel target. Only 1-2 antiprotons along with many secondary particles are created from 10^5 protons, which is quite inefficient. Furthermore, a $p\bar{p}$ collision loses its advantage on cross section compared to pp collision when the energy is high, as the sea quarks and antiquarks in the proton carry a higher momentum when energy increases. However, unlike the LEP and the Tevatron accelerators, the LHC needs two rings for the two proton beams. Each beam pipe has its own magnet channels and vacuum systems. In order to minimize the cost, the LHC magnet has a "2-in-1" design where the two beams have separate magnet coils with opposite field polarities but share the same cryostat and powering infrastructure.

There are 1232 15-meter long, 35 ton super-conducting dipole magnets that provide bending for the proton beams. These superconducting systems operate in superfluid helium at 1.9 K. According to the magnetic rigidity equation $B[\mathrm{T}]R[\mathrm{m}] = 3.34 \cdot p[\mathrm{GeV/c}]$ and considering about the 60% occupation of the circumference, these dipole magnets have to produce a magnetic field of 8.3 T, in order to achieve the maximum beam energy of 7 TeV.

During the operation of the LHC, it is unavoidable that some particles have a slightly different momentum or position/angle offset to the design configuration. So, besides dipole magnets, the LHC also uses pairs of quadrupole magnets to focus the particles in a tight beam. The paired two quadrupoles are differed by a ϕ angle of 90° in order to squeeze the beam both vertically and horizontally.

In addition to dipole and quadrupole magnets, the LHC uses many high order magnets (sextupole, decapole and octupole) in order to correct the corresponding high order component of the dipole field and help with beam focusing. When the beam enters the detector regions, a different magnet system called the "inner triplet" magnets is used. This system makes use of three quadrupoles to squeeze the beam more tightly so that the two beams coming from opposite directions can collide with small transverse cross section. These inner triplets are located at each of the four large LHC detectors, ATLAS (A Toroidal LHC ApparatuS), CMS (the Compact Muon Solenoid), ALICE (A Large Ion Collider Experiment) and LHCb (study of physics in B-meson decays at LHC).

The ATLAS and CMS experiments are designed as general purpose detectors to make measurements of SM processes and to search for BSM physics. Both experiments discovered the Higgs boson in 2012 [3, 4]. The ALICE experiment focus on studying the properties of the quark-gluon plasma and understanding the mechanism in QCD that confines quarks and gluons using heavy ion collisions. The LHCb experiment is designed to study b-quark physics and measure the CP violation in the b-hadron interactions.

Besides these four main experiments, there are three smaller experiments: TOTEM (TOTal Elastic and diffractive cross section Measurement), LHCf (Large Hadron Collider forward) and MoEDAL (Monopole and Exotics Detector at the LHC). The TOTEM Experiment measures the total pp cross section with the luminosity-independent method and study elastic and diffractive scattering at the LHC [84]. The LHCf experiment is designed to provide precise measurements of inclusive production cross section of forward neutral pions using pp or p-Pb collisions [85]. The MoEDAL is an experiment that dedicates to searching for magnetic monopoles, dyons and electrically charged stable massive particles [86].

3.1.2 Beam Injection Scheme

Proton beams at the LHC are accelerated by a longitudinal oscillating voltage generated by RF cavities. In order to be accelerated at the correct timing, the RF frequency has to be an integer multiple of the revolution frequency of the proton. Under the current operation condition, the RF frequency is tuned to be 400 MHz. In the RF field, the protons with slightly different momenta arriving earlier or later will be accelerated or decelerated.

As a result, the beam will be grouped into packs of protons, which are called "bunches". The bunch structure in each beam is referred to as the filling or injection scheme. Figure 3.2 shows the designed LHC bunch structure [87]. The maximum allowed number of bunches in each beam is 3564. Considering the time needed to switch on the magnets which divert the beam from the LHC into the dump ($\sim 3\mu$s) and other smaller time needed in the SPS and LHC injection, not all bunches are filled with protons and some of them are just empty, which are called empty bunches. The combination of these empty bunches is referred to as the abort gap. The standard design allows 2808 bunches per beam. Each bunch contains 1.15×10^{11} protons. The PS generates a batch of 72 bunches with 25 ns spacing. The SPS allows 4 batches (288 bunches) of input from the PS which are then sequentially transferred to the LHC main ring. The filling of each ring will take about 3 minutes.

The actual beam configurations used in the LHC Run 2 (2015-2018) are slightly different than the design parameters. In order to protect the equipment, for example, the transfer lines between the SPS and the LHC, from the potential damage caused by the high energy beam, the maximum number of the bunches in the SPS injection is reduced to nearly half of the design value. Different years had different limits, but they were all less than the 144 bunches per injection from the SPS. This together

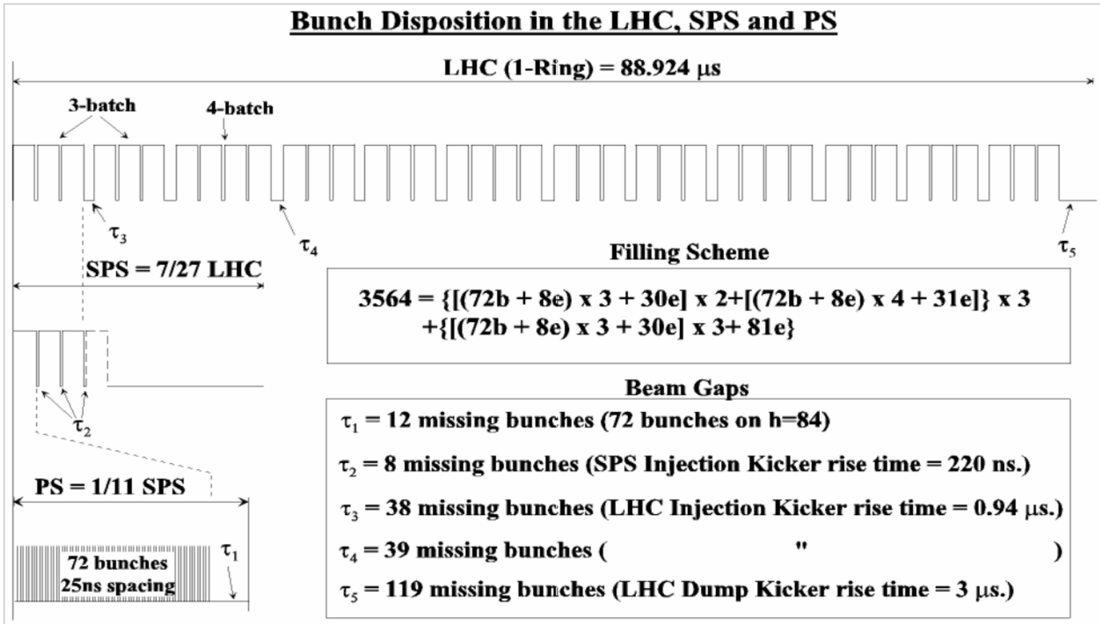

Figure 3.2: The bunch structure of the LHC proton beam.

with the improved abort gap gave rise to the maximum of 2556 bunches per beam in 2017 and 2018. Figure 3.3 shows the actual configurations of the number of bunches used in the Run 2 [88].

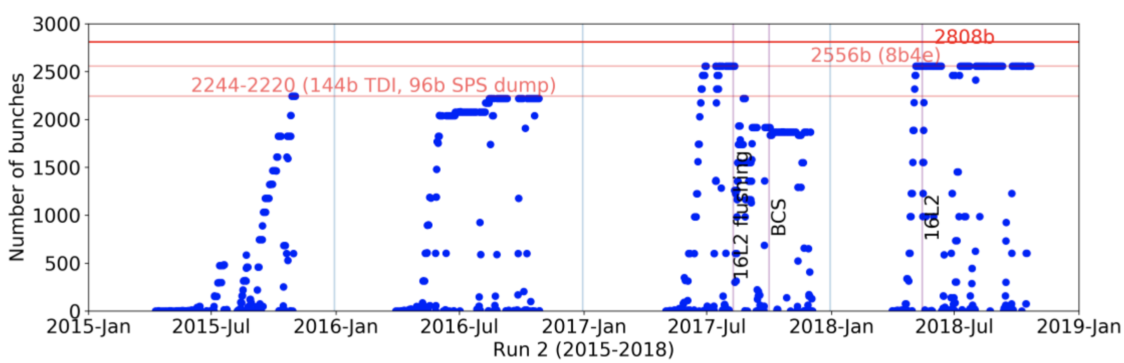

Figure 3.3: The number of bunches as a proton beam parameter used in the Run 2 at the LHC.

Since many protons are filled in a bunch, there could be multiple simultaneous collisions producing secondary vertices besides the hard-scattering interaction at the bunch crossing. These additional collisions are referred to as pileup. Pileup produces soft particles that deposit energy in the calorimeter cells that affects the measurement and reconstruction of objects that rely on calorimeter information. The amount of pileup, μ, can be calculated by the following formula [89]

$$\mu = \frac{\mathcal{L}\sigma_{inelastic}}{n_c f_{\text{rev}}} \tag{3.1}$$

where $\mathcal{L}$ is the instantaneous luminosity, $\sigma_{inelastic}$ is pp inelastic cross section, n_c is the number of colliding bunch pairs in the LHC and $f_{\text{rev}} = 11.245$ kHz is the revolution frequency [87]. The pileup calculated by this formula is called in-time pileup because it is from the same bunch crossing. The collisions coming from other bunch crossings are called out-of-time pileup.

3.1.3 LHC Luminosity

The instantaneous luminosity $\mathcal{L}$ is an important parameter in a collider experiment that measures the number of hard collisions that can happen at a certain time. The product of the instantaneous luminosity and event cross section σ gives rise to the event rate:

$$\frac{dN}{dt} = \mathcal{L} \cdot \sigma. \tag{3.2}$$

The integrated luminosity, $\int \mathcal{L}dt$, gives a measure of the total number of collisions that can happen within a certain period of time. Usually, to get the observed number of events, we have to apply an acceptance factor to N due to the inefficiencies from detector acceptance, triggering, object reconstruction, and event selection.

The instantaneous luminosity $\mathcal{L}$ is given by

$$\mathcal{L} = f\frac{n_1 n_2}{4\pi\sigma_x\sigma_y}, \tag{3.3}$$

where n_1 and n_2 are the numbers of particles inside two proton beams, f is the frequency at which the two beams collide, σ_x and σ_y are the beam transverse sizes. This equation implies that $\mathcal{L}$ can be improved by reducing the beam size. In 2016, the LHC adopted a new beam production scheme called Batch Compression Merging and Splitting (BCMS) [90] that greatly reduced the beam size and hence increased the peak luminosity by around 20%. The above expression assumes no crossing angle between two beams and no beam offsets, otherwise corresponding correction factors have to be included [91].

During the 2015-2018 data taking period, the total delivered luminosity for the pp collision by the LHC is 158 fb^{-1}. And the ATLAS detector recorded 147 fb^{-1}. The data that is good for physics study have a luminosity of 139 fb^{-1} and they are used in our analysis.

3.2 The ATLAS Detector

3.2.1 Overview

The ATLAS detector is shown in Figure 3.4 [92, 93]. The ATLAS detector has a cylindrical structure. It is 44 meters in length and 25 meters in height. The total weight is about 7000 tonnes.

The ATLAS uses a right-handed coordinate system that is defined as follows. The z-axis runs longitudinally through the detector and follows the beam directions. The x-y plane is perpendicular to the beam direction. The positive x-axis is defined as pointing from the interaction point to the center of the LHC ring and the positive y-axis is defined as pointing upwards. The azimuthal angle ϕ is defined on the x-y plane and the polar angle θ is measured with respect to the beam axis. In many cases, the pseudorapidity $\eta = -\ln\,\tan(\theta/2)$ is used to describe the direction of a particle rather than the polar angle θ. The pseudorapidity is an approximation of the rapidity $y = \frac{1}{2}\ln[(E + p_z)/(E - p_z)]$ when a particle is highly relativistic. The reason rapidity is used is that rapidity difference between two particles is invariant under Lorentz boost along the beam axis. Another frequently used variable is the angular separation between two objects defined as $\Delta R = \sqrt{\Delta\eta^2 + \Delta\phi^2}$.

The ATLAS detector has 4 main detecting system: the inner detector (ID), the electromagnetic calorimeter (ECal), the hadronic calorimeter (HCal) and the muon spectrometer (MS). The inner detector is the innermost system that surrounds the beam pipe. It provides position and momentum information of charged particles. It is also used in vertex finding and particle identification. The inner detector is surrounded by the two calorimeter systems. The ECal and HCal measure the energy of electromagnetic showers and the energy of hadronic showers respectively with good energy resolution. The muon spectrometer covers the outermost region of the detector. It measures the trajectory and momentum of muons.

There is a dedicated superconducting magnet system in the ATLAS detector to provide the magnetic field needed for the momentum measurement. It consists of a central solenoid and a system of three large air-core toroids: one barrel toroid and two endcap toroids. The central solnoid provides a magnetic field of 2 T for the inner detector. The barrel toroid and endcap toroids provides magnetic fields of approximately 0.5 T and 1 T for the muon detectors in the central and endcap regions, respectively.

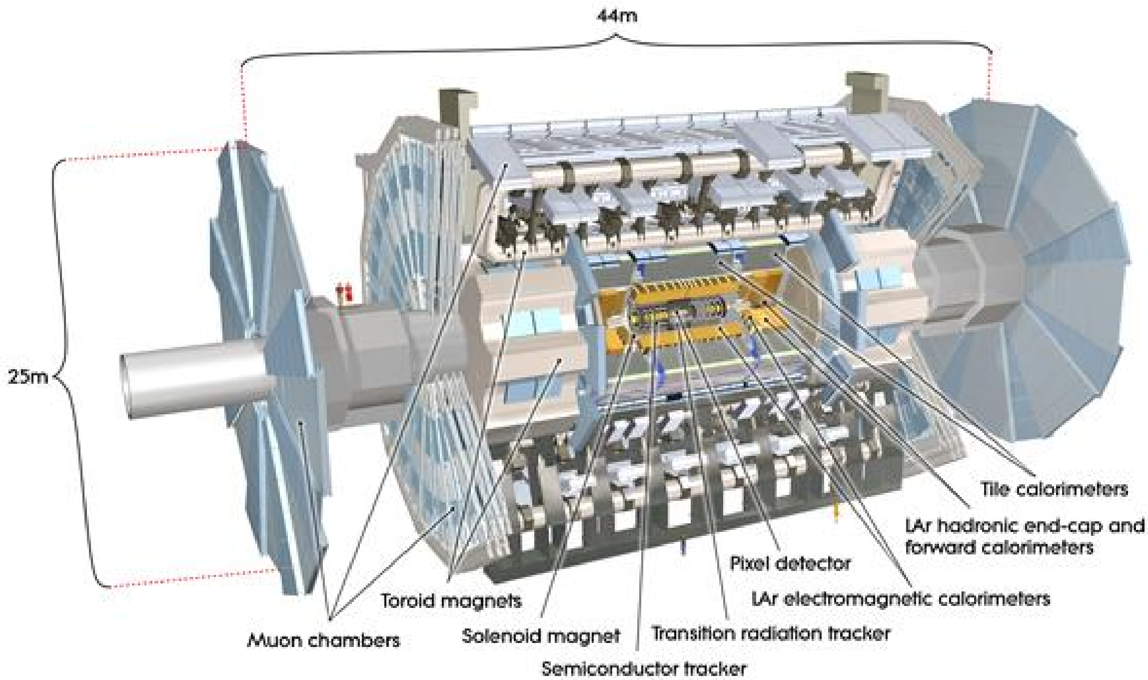

Figure 3.4: Structure of the ATLAS detector.

3.2.2 The Inner Detector

The ATLAS inner detector covers the range $|\eta| \leq 2.5$ and has a cylindrical layout with a length of about 7 meters and a radius of 1.15 meters. The layout is shown in Figure 3.5 [94]. The ID consists of three subdetectors: the pixel detector, the Semiconductor Tracker (SCT) and the Transition Radiation Tracker (TRT). The first two subdetectors use the technology of silicon detectors. The silicon detector is a semiconductor detector which will create an electrical signal when its depletion zone is ionized by a charged passing particle. The silicon detectors can be made into a form of pixels or a form of strips. The former form is used for the pixel detector and latter form is used by the SCT. The pixels can provide 3-dimensional position information while the tracker strips provide 2-dimensional position information.

The TRT is based on the technology of the straw drift tube, which is basically a proportional drift tube with a positively charged wire in the center. The wire will collect the electrons from the gas ionization caused by the charged paritcles and provides 2-dimensional position information.

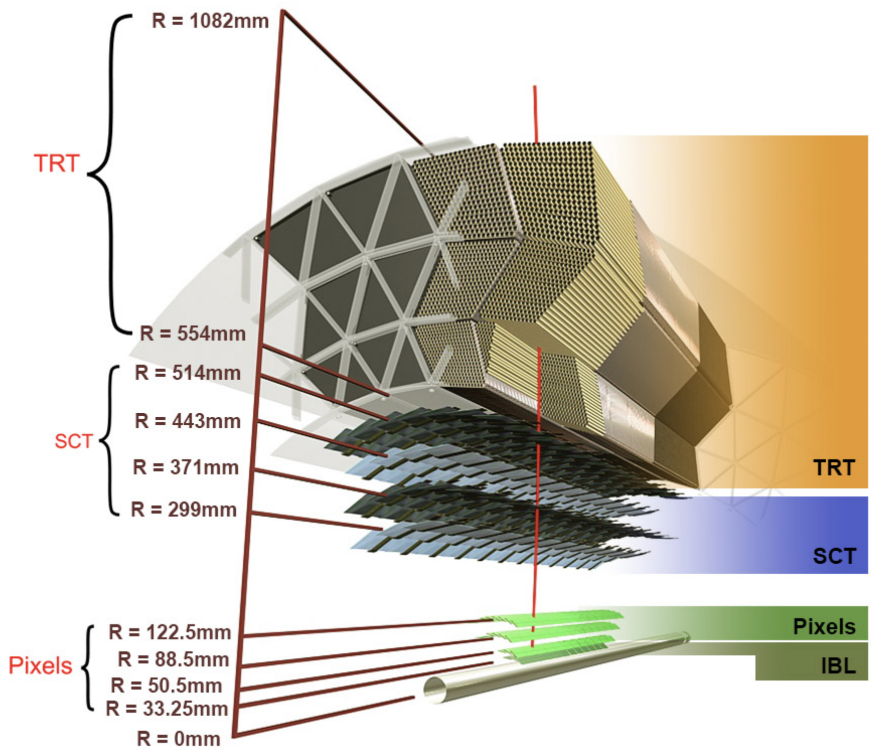

Figure 3.5: Schematic view of the ATLAS inner detector.

The pixel detector makes up the innermost part of the ID covering the pseudorapidity range $|\eta| \leq 2.5$. It has a barrel region and two identical endcap regions. The barrel region consists of three barrel layers and each of the endcap region is composed of three disk layers. There are a total amount of 1744 modules that consist of pixel sensors, front-end chips and flexible printed circuits mounted on these layers. In each module, there are 47232 pixels and 46080 readout channels, which in total gives rise to about 80 million channels, with 67 million in the barrel and 13 million in the endcaps. These channels cover an active area of 1.45 m^2 in the barrel and 0.28 m^2 in the endcaps [95].

The pixel detector is designed to have good resolution for reconstructing primary and secondary (for b-tagging) vertices for a peak luminosity of 1×10^{34} cm^{-1}s^{-1}. For Run 2, in order to improve tracking robustness and precision, and prevent the reduction of the readout efficiency due to the increasing luminosity, a new tracking layer called the insertable B-layer (IBL) [96] was added. It was placed between the beam pipe and the innermost pixel layer. The IBL is designed for an integrated luminosity of 550 fb^{-1} and a peak luminosity of 3×10^{34} $\mathrm{cm}^{-1}\mathrm{s}^{-1}$. It has 224 modules and approximately 6 million pixels to ensure good performance on vertexing and b-tagging.

The SCT surrounds the pixel detector covering radial distances from 299 mm to 560 mm. It is used for precise tracking, but has a low cost per unit area compared to the pixel detector. In the barrel region, there are 4 concentric layers with a total number of 2112 silicon-strip modules on them. The strip pitch is set to 80 μm in order to achieve the required tracking precision. In the endcap regions, there are 9 disks with 988 modules on each side. The strips in the endcaps are placed radially with constant azimuth. The mean pitch for the endcap strips is 80 μm. The spatial resolution obtained with a module is 16 μm in the $R\phi$ plane and 580 μm in z direction [97].

The TRT is the outermost subdetector in the ID. It provides accurate position and momentum measurements as well as discrimination between electrons and charged pions, since electrons and charged pions have different transition radiations in the TRT detector, which results in hits with different TRT straw pulse heights. The barrel region contains 52544 straws oriented parallel to the beam pipe. The two endcap regions each has 122880 straws radially aligned to the beam axis [98]. The length of a straw is either 144 cm or 37 cm depending on whether it is in the barrel or the endcaps. The detector geometry ensures that charged particles with $p_T > 0.5$ GeV and $|\eta| < 2$ will traverse at least 36 straws except the barrel-endcap transition region [93]. Each straw has a inner diameter of 4 mm and provides a resolution of 130 μm in the $R\phi$ direction.

3.2.3 Calorimeters

The calorimeters shown in Figure 3.6 are mainly designed to mearsure the energy of particles, but also contribute to the position measurement, the identification of jets and the measurement of missing transverse energy. There are two main calorimeter systems: the electromagnetic calorimeter (ECal) and the hadronic calorimeter (HCal). The electromagnetic calorimeter is designed to measure the energy deposited from particles that produce electromagnetic showers, mainly electrons and photons. In order to absorb the shower completely, the total thickness of the ECal is designed to be > 24 radiation lengths (X_0) in the barrel and > 26 radiation lengths in the endcap.

The hadronic calorimeter is used to measure the energy of particles that produce hadronic showers. The hadronic shower is characterized by the nuclear interaction length (λ), which is defined as the mean distance before an inelastic interaction happens. The total thickness of the ECal and HCal is 9.7 λ at $\eta = 0$.

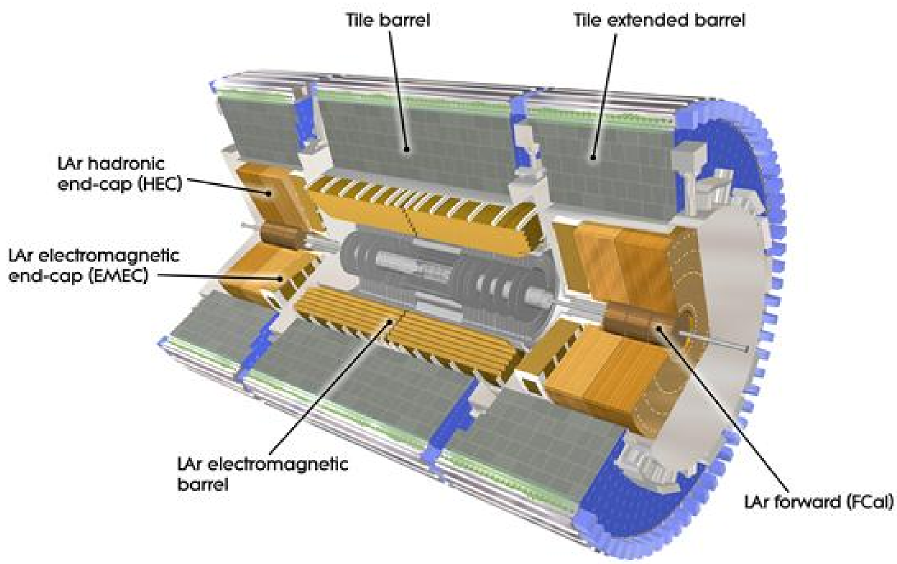

Figure 3.6: Schematic view of the ATLAS Calorimeters.

The ECal covers the region $|\eta| < 1.475$ in the barrel and $1.375 < |\eta| < 3.2$ in the endcaps and has a accordion geometry. The barrel region consists of two half-barrels separated by a small gap (6 mm) at $z = 0$. The endcap calorimeter at each side consists of two coaxial wheels: an outer wheel covering the region $1.375 < |\eta| < 2.5$ and an inner wheel covering the region $2.5 < |\eta| < 3.2$. The region $|\eta| < 2.5$ is designed for precision physics which contributes to particle identification and provide a precise position measurement in η. The region $|\eta| > 2.5$ has a coarser lateral granularity, but it is sufficient to satisfy the requirements of jet reconstruction and missing transverse energy measurement. In the region $|\eta| < 1.8$, there is a presampler that precedes the calorimeter to correct the energy losses in material upstream of the ECal. The ECal is a sampling calorimeter using lead absorber plates that are immersed in the liquid argon (LAr). There are accordion-shaped copper-kapton electrodes positioned between lead absorbers to collect the electrons from LAr ionization. The signals are collected by an approximate number of 190000 channels and are sampled every 25 ns [92].

The HCal uses three different techniques depending on the η. The tile calorimeter occupies the region $|\eta| < 1.7$. It is a sampling calorimeter using ion as the absorber and scintillating tiles as the active material. The tile calorimeter is segmented to three layers in depth with thickness of about 1.5, 4.1 and 1.8 λ. The radial depth of the tile calorimeter is approximately 7.4λ.

In the endcaps, the hadronic end-cap calorimeter (HEC) covers the region $1.5 < |\eta| < 3.2$. It is a LAr sampling calorimeter that uses copper as an absorber. This calorimeter at each endcap side consists of two wheels, each of which is further divided into two copper layers with different radius and thickness.

The forward calorimeter (FCal) provides coverage over $3.1 < |\eta| < 4.9$. The FCal consists of three layers, namely FCal1, FCal2 and FCal3. FCal1 is a copper-LAr calorimeter designed for electromagnetic measurements with a depth of 28 X_0. FCal2 and FCal3 use LAr and tungsten instead of copper and are designed for hadronic measurements. These three layers have a combined depth of 10 λ. Besides materials, each FCal consists of cylindrical electronodes arranged parallel to the beam pipe. Each electronode consists a tube at ground and a rod at 250 V inside the tube. LAr is filled in a small gap which is 0.27 mm, 0.38 mm and 0.50 mm for FCal1, 2 and 3 respectively between the tube and rod for a fast readout [99]. There are 3584 channels total on both endcap sides [92].

3.2.4 Muon Spectrometer

The muon spectrometer (MS) is the outermost part of the ATLAS detector covering the range $|\eta| < 2.7$. It is designed to measure the momentum of the charged particles that exit the calorimeters and provide trigger information for $|\eta| < 2.4$. Figure 3.7 shows its cross section [93]. In the barrel, there are three stations of tracking chambers that are used for track reconstruction. They are placed in three concentric cylindrical shells at radii of approximately 5 m, 7.5 m, and 10 m and extend to $|\eta| = 1$. In the endcaps, the tracking chambers cover the range $1 < |\eta| < 2.7$ and are arranged in three wheels that are perpendicular to the beam axis. These chambers are located at distance $|z|$ of about 7.4 m, 10.8 m, 14m and 21.5 m from the interaction point.

The Monitored Drift Tube (MDT) chambers are used for the precision measurement in range $|\eta| < 2.7$. The MDT chambers are given different names depending on their position. The naming scheme uses three letters (e.g. BIS), with the first letter referring to barrel or endcaps, the second letter referring to inner, middle and outer station and the third letter referring to large or small sector. These chambers consists of two multilayers, each with three or four layers of MDTs. These two multilayers are separated by a distance of 6.5 mm or 317 mm depending on whether they are in BIS chambers or BOS, BOL and BML chambers.

The MDT chambers provide an average position resolution of 35 μm. For the forward region, $2.0 < |\eta| < 2.7$, cathode strip chambers (CSCs) are used in the innermost layer for tracking. It provides a resolution of 40 μm in the R direction and about 5 mm in ϕ direction.

Besides the tracking chambers, there are three stations of resistive plate chambers (RPCs) and thin gap chambers (TGCs), used for triggering in the barrel and endcaps, respectively. The RPCs covers the region $|\eta| < 1.05$ and the TGCs cover the region $1.05 < |\eta| < 2.4$. These chambers can reliably respond within the 25 ns bunch crossing with a time resolution of 1.5 ns for the RPCs and 4 ns for the TGCs. There trigger chambers are also capable of measuring the coordinate of the tracks. The MDTs, CSCs, RPCs and TGCs are based on different techniques so that can meet needs for different measurements or triggering.

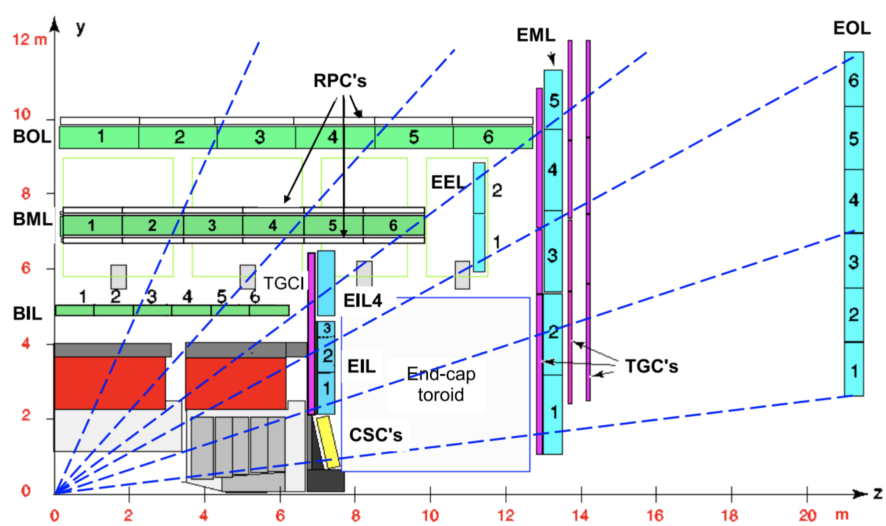

Figure 3.7: Cross section of the ATLAS muon spectrometer.

- **Monitored Drift Tubes**

  The MDT is an aluminum drift tube with a diameter of 29.970 mm. A tungsten-rhenium wire with a diameter of 50 μm is centered to the tube at a potential of 3080 V. The tube is filled with gas mixture of 93% Ar and 7% CO_2 at 3 bar absolute pressure. The MDT system measures the drift time of electrons which is then mapped to drift distances by using a time-to-distance transfer function. Each drift tube has an average spatial resolution of about 80 μm [100].

- **Cathode Strip Chambers**

  The CSCs are placed at the forward region to cope with a high rate of charged particles from the interaction. The limit of counting rate for the MDTs is at about 150 Hz/cm^2, while the CSCs can function up to a rate of 1000 Hz/cm^2. The CSCs are multiwire proportional chambers with the wires oriented in the radial direction. They are operated at 1900 V with a 80% Ar and 20% CO_2 gas mixture. In the ATLAS, the CSC system consists of a disk with 8 large chambers and a disk with 8 small chambers arranged in ϕ. Each chamber has four CSC planes and as a result, there are 4 measurements in η and ϕ along each track. Each of the plane provides a resolution of 60μm.

- **Resistive Plate Chambers**

  There are three RPC stations in the MS barrel. Two of them (RPC1 and RPC2) sandwich the middle MDT layer and the third one (RPC3) is located outside the outer MDT layer. The lever arm between RPC1 and RPC3 permits a high-p_T trigger to select tracks with momentum between 9 GeV and 35 GeV. And the inner two layers, RPC1 and RPC2 provide a low-p_T trigger for 6-9 GeV tracks. Each station consists of two detector layers that measure η and ϕ. The RPC detector is made of two resistive plates that are made of phenolic-melaminic plastic laminate. The two plates have a gap of 2 mm which is filled with $C_2H_2F_4$/Iso-C_4H_{10}/SF_6 (94.7/5/0.3) gas mixture. The electric field between the two plates is 4.9 kV/mm.

- **Thin Gap Chambers**

  There are four TGC layers in the MS endcap. Three of them are near the middle MDT station. TGC1 is placed in front of the EML wheel while TGC2 and TGC3 are placed behind the MDT wheel. The coincidence of these three layers is used for triggering. There is a fourth TGC layer placed in front of the innermost tracking layer. It is mounted with the MDTs and CSCs at a distance of about 7 m from the interaction point and forms the Small Wheel. The TGC itself is a multiwire proportional chamber with a 55% CO_2 and 45% n-C_5H_{12}

gas mixture. Its cathode strips and anode wires operating at 2900 V provide measurements on η and ϕ. The wire-to-wire distance is designed to be 1.8 mm in order to provide a good time resolution.

3.3 Long-lived Particle Search in ATLAS

In the ATLAS detector, there are a lot of searching strategies can be used for the long-lived particle (LLP) search. Following is a list of analyses with different signatures in the ATLAS expriment.

- **Displaced vertex** Depending on the decay positions and models, there are several searches for displaced vertex including our analysis. This dissertation documents the search for displaced vertices in the ATLAS muon spectrometer. The Hidden sector model is used as the theoretical benchmark model. In this scenario, a pair of LLPs can be produced via the Higgs portal and subsequently decay hadronically.

  A similar analysis considers the topology where one LLP decays in the ID and the other decays in the MS [101]. The displaced tracks in the inner detector can be reconstructed by large radius tracking (LRT) algorithm [102], which make use of the detector hits left over from standard tracking procedure. These hits are used to reconstruct tracks with loosened requirements on the transverse and longitudinal track impact parameters (d_0 and z_0) in order to increase reconstruction efficiency. The ID displaced vertex reconstruction takes both standard tracks and large-radius tracks as inputs. For the MS displaced vertex reconstruction, there is a dedicated standalone vertex finding technique which will be explained in Chapter 7. The combined ID-MS analysis should have better sensitivities to shorter lifetimes than the two displaced vertices in the muon spectrometer analysis.

  SUSY models include other LLP production and decay topologies. One such LLP search seeks for a displaced vertex in the inner detector and a muon [103]. Assuming the weak RPV coupling in the MSSM superpotential term, a top squark can be long-lived and will decay into a muon and a quark ($\tilde{t} \rightarrow \mu + q$). Another SUSY inspired search looks for displaced vertices in the inner detector and missing transverse momentum using split SUSY benchmark model [104]. In this model, a long-lived gluino ($\tilde{g}$) can decay to 2 quarks and a neutralino

($\tilde{\chi}_1^0$) which is a lightest supersymmetric particle (LSP). This decay happens via a massive virtual sqaurk mediator, thus the decay width of the gluino is suppressed. The LLPs covered by these SUSY analyses usually have very high mass. The current constrain is at $\mathcal{O}(1)$ TeV for lifetimes between $\mathcal{O}(10^{-2})$ ns and $\mathcal{O}(10)$ ns.

- **Displaced jets in the calorimeter** In addition to LLP signatures as displaced vertices in the ID or Muon Spectrometer, LLPs can also decay into hadronic jets. A related search that looks for LLP decaying to hadronic jets in the hadronic calorimeter (HCal) or at the outer edge of the electromagnetic calorimeter (ECal) is presented in Ref. [105]. These displaced jets have distinct features from the standard jets. Since they are displaced, they will not leave any activity in the Inner Detector and will result in a high ratio of energy deposited in the HCal versus ECal. This ratio is called the CalRatio. Another feature is that the displaced jet is narrower than the SM jet originating from the interaction point because the particles in the displaced jet have less time to become separated. Events are selected by the dedicated CalRatio trigger that makes use of these features.

- **Displaced leptons or lepton-jets** LLP searches have also been carried out using LLP decays into leptons [106] or lepton-jets [107]. One recent search uses a signature of displaced dimuon pairs [106]. Such decays can arise in a SUSY model that has a heavy long-lived neuralino state ($\mathcal{O}(100)$ GeV) and a "Higgs portal" model that couples the Higgs with a pair of light dark photons ($\mathcal{O}(10)$ GeV). Muons from high-mass states have large transverse momentum and large impact parameter and the muons from low-mass states have lower transverse momentum. A variety of triggers are employed in order to cover the wide kinematic range possible.

  Lepton-jets arise in the analysis that considers the FRVZ model [108, 109], where a Higgs boson can decay to a pair of dark fermions [107]. A dark fermion can decay to either one or two dark photons. Dark photons will decay to a fermion pair. For this particular search, the mass of the dark photon is chosen to be small (between twice muon mass and twice tau mass). As a result, the dark photons are expected to be produced with large boosts, resulting in collimated groups of muons (muonic dark photon jet) and light hadrons (hadronic dark photon jet) in a jet-like structure. To select events with narrow jets in the HCal and non-prompt collimated muons, the muon narrow-scan trigger and CalRatio trigger are used. For this particular search, final states with both two dark photons and four dark photons are used. Final states with combinations of muonic and hadronic dark photon jets are also considered.

- **Exotic LLP signatures** In addition to the searches described above, even more exotic LLP signatures have been sought including disappearing tracks [110], tracks with anomolous ionization [111] and non-pointing photon [112]. A disappearing track refers to the case where a long-lived massive charged particle decays to lighter neutral particle but with small mass splitting plus a soft SM particle such as a pion. Since the neutral particle and the soft pion can not be reconstructed by the detector, the track of the massive charged particle disappears after the decay. Tracks with anomolous ionization can be caused by heavy charged long-lived particles. These heavy charged particles have low boost and when they travel through the detector, they will have a distinguishable dE/dx ionization compared to SM particles with unit charge. This analysis is described by [111]. Non-pointing photons refres to the photons originating from a displaced decay and thus can not be traced back to the primary vertex [112].

There are many other analyses out of the above list. In Figure 1.1, the most recent LLP analyses and their 95% exclusion limit on the liftimes [29] can be found.

CHAPTER 4

Data and Monte Carlo Samples

4.1 Data Samples

This thesis uses the pp collision data at $\sqrt{s} = 13$ TeV collected by ATLAS taken from July 2015 to October 2018. During the data-taking period, the peak instantaneous luminosity increased from 5×10^{33} cm^{-2} s^{-1} in 2015 to 1.9×10^{34}cm^{-2}s^{-1} in 2018. The average number of collisions per bunch crossing, $\langle\mu\rangle$, increased from ~ 13 in 2015 to ~ 36 in 2018 accordingly [113].

The data taking in ATLAS is separated into multiple runs, with each run standing for a data set that is continuously recorded by ATLAS. Each run is further divided into different LumiBlocks. A LumiBlock is a period of order 60 s during which instantaneous luminosity, detector and trigger configuration and data quality conditions are considered constant. There are periods in which detectors are not in normal condition, resulting in LumiBlocks with a bad quality. This kind of LumiBlocks are not used for physics analysis. The LumiBlocks with good data quality are provided by ATLAS in a set of xml files which are called Good Run List (GRL). All data used in this analysis were recorded during LumiBlocks with good detector quality.

Figure 4.1a shows the integrated luminosity versus time in ATLAS. The "Good for Physics" integrated luminosity has the data quality criteria applied and is calculated from the LumiBlocks that are included in the GRL. The efficiency resulted from data quality selection is shown in Figure 4.1b. The data samples from 2015 plus 1016, 2017, and 2018 with the GRL applied have integrated luminosity of 36.2 fb^{-1}, 44.3 fb^{-1} and 58.5 fb^{-1}, respectively. Therefore the total integrated luminosity in Run 2 is 139 fb^{-1}. The total uncertainty is 2.4 fb^{-1}, which corresponds a relative uncertainty of 1.7% [114]. The luminosity measurement is given by the LUCID-2 detector [115].

4.2 Monte Carlo Samples

4.2.1 Signal Samples

Monte Carlo (MC) simulation is a commonly used method in the high energy physics to study the behavior of either signal or background processes as they might appear

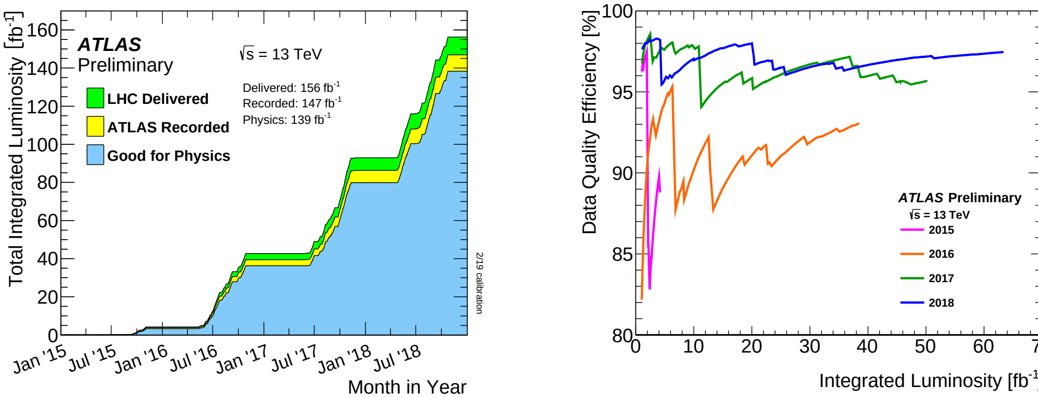

(a) (b)

Figure 4.1: Figure 4.1a shows integrated luminosity versus time delivered to ATLAS (green), recorded by ATLAS (yellow) and certified to be good quality data (blue) for pp collision at $\sqrt{s} = 13$ TeV in full Run 2. Figure 4.1b shows the data quality efficiency versus total integrated luminosity collected by the ATLAS experiment between 2015 and 2018.

in the ATLAS data. In our analysis, to study the LLP process, a set of MC samples that simulate the process of Higgs or Higgs-like boson decaying to displaced jets are produced.

The masses for the Higgs boson and scalar particles and proper lifetime are summarized in Table 4.1. The mass points are chosen to cover a wide range of phase space. The lifetimes are chosen based on the 2015+2016 CalRatio and MS displaced jets analysis. Figure 4.2 shows the signal efficiencies, which is the ratio of number of signal events passing event selections and total number of events, from the 2015+2016 CalRatio and MS displaced jets analysis. The red dashed line corresponds to the proper lifetime used for MC signal generation for this analysis, which increases the signal efficiency in the MS analysis but doesn't negatively affect the CalRatio analysis a lot, since the signal samples are shared by both of these analyses.

This MS analysis is sensitive to a wide range of mean proper lifetimes, but producing MC samples with multiple different mean lifetimes is extremely time consuming. A toy MC method is used to extrapolate the number of expected events to the range of mean proper decay lengths between 0 and 300 m. For each mass point, a toy sample with 2 million events is produced. For each LLP in the toy sample, a random decay length is calculated based on an exponential distribution. The physical LLP decay position in the detector is then determined by using the decay length and the

LLP 4-momenta from the toy sample. Then the overall probability of the event with different lifetimes to satisfy the signal selection criteria is then calculated from the efficiencies that satisfy each selection criterion. This procedure will be described in detail in Chapter 8. To validate this toy MC method, some of the MC samples are produced with two different lifetimes.

Model	m_H [GeV]	m_s [GeV]	N events	Lifetime $c\tau$ [m]
$H \to ss$	125	5	150k	0.127
		5	600k	0.411
		15	500k	0.580
		35	700k	1.310
		35	500k	2.630
		55	1000k	1.050
		55	450k	5.320
	60	5	600k	0.217
		15	300k	0.661
	200	50	200k	1.255
	400	100	200k	1.608
	600	50	300k	0.590
		150	300k	1.840
		150	150k	3.309
		275	1000k	4.288
	1000	50	300k	0.406
		275	300k	2.399
		275	150k	4.328
		475	1000k	6.039

Table 4.1: Mass parameters and lifetimes for the simulated Hidden Sector samples.

Signal MC events for the Hidden Sector model are generated with the following procedure. The signal processes at parton level are produced by the MadGraph generator MadGraph5_aMC@NLO [116] of version 2.6.2. The signal model used for Higgs boson to LLP pair process is HAHM_variableMW_v3_UFO. Pythia8 [117] is used for modeling parton shower and hadronization. The A14 tune [118] is applied to optimize the parameters in the hadronization and parton shower models. The parton distribution function set used for signals is NNPDF31LO. All the events are processed by a full simulation of the ATLAS detector by using GEANT4 toolkit [119].

In the Hidden Sector model, the couplings of the scalar to SM fermions are determined by the Higgs Yukawa coupling. Therefore, each long-lived scalar decays

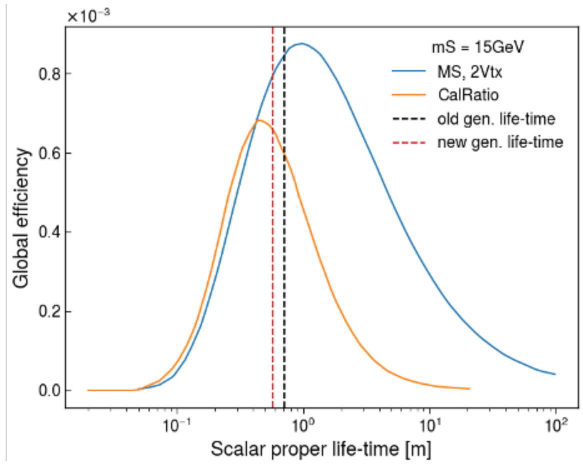

Figure 4.2: Lifetime optimization based on both of the signal efficienies from CalRatio and MS displaced jets analysis. Blue is the signal efficiency of the MS 2-vertex search from the 2015+2016 analysis. Orange is the signal efficiency from the 2015+2016 CalRatio analysis. The efficiencies in the plot are derived based on the Hidden Sector samples with a 125 GeV Higgs boson decaying to 15 GeV scalar pairs. Black dashed line is the lifetime used in the 2015+2016 analysis. Red dashed line is the new lifetime chosen for this full Run 2 analysis in order to increase the signal efficiency for the MS two-vertex search.

mainly to the heaviest fermion pair that is kinetically accessible, $b\bar{b}$, $c\bar{c}$, and $\tau^+\tau^-$. The branching ratios of these decays depend on the mass of the long-lived scalar (m_s). For $m_s \gtrsim 25$ GeV, their branching ratios are equal to 85%, 5%, and 8%, respectively. For the sample with $m_s = 475$ GeV, the long-lived scalar decays 100% to $t\bar{t}$. Only the dominant gluon-gluon fusion production mode is considered in the analysis.

The event output from detector simulation is saved in Raw Data Object (RDO) format, which is used as the input for event reconstruction. Event reconstruction will be described in Chapter 6. It is a software-based procedure using a data-processing framework called Athena. Athena release version 21 is used to reconstruct the simulated or real data in the analysis. The output from reconstruction used in this analysis is Analysis Object Data (xAOD), which is a format that contains sufficient event information and is readable by ROOT [120]. Different caches are used for reconstruction according to the data-taking years: AtlasOffline_21.0.20 is used for 2015 and 2016, Athena_21.0.53 is used for 2017 and Athena_21.0.77 is used for 2018. The xAOD samples have a very large size and thus are not convenient to use. According to the needs of the physics analysis, they are further processed by the Athena Derivation Framework, producing derived xAOD (DAOD) files, which are commonly referred to as derivations, with all the needed AOD objects but reduced size. The derivation for MC simulation is produced by AthDerivation_21.2.56.0. For data derivations, a different cache AthDerivation_21.2.108.0 is used as it contains the single jet trigger needed for the scale factor study. The derivations are further used as input for the root-tuples using the analysis framework developed by our analysis team.

The pileup of Run 2 data-taking period is modeled by overlaying simulated pp events generated with PYTHIA 8.2 [121] using the NNPDF2.3LO set of parton distribution functions and the A3 tune [122] over the original hard-scattering event. To reproduce the distribution of average number of interactions per bunch crossing $\langle\mu\rangle$ observed in the data, MC events are reweighted following the procedure described in [123].

Since all the signal MC samples are produced at the leading order (LO), to check whether the next-to-leading order (NLO) effect, such as initial state radiations jets, will have any impact on the kinematics of LLPs, we did a preliminary study based on the CKKW-L merging scheme [124] with PYTHIA8. In this scheme, jets are regularized by a cut off t_{MS} which is called merging scale. Soft and collinear jets below the merging scale are modeled by parton shower while the hard and well-separated jets above the scale are calculated by matrix elements. The merging scheme provides a way to combine these two parts properly. For this study, a process of Higgs boson decaying to two 25 GeV scalars was considered, and the value of t_{MS} was set to 40 GeV. Events in which one and two ISR jets were considered, and their effect on the p_{T} and η distributions are shown in Figure 4.3. Negligible effects are observed from the distributions. This supports of use of MC generation at LO.

Figures 4.4 and 4.5 show the distributions of the p_T, boost β, pseudorapidity η, ϕ, radial decay position R and longitudinal decay position z of the long-lived particles for a selection of the generated SM Higgs and non-SM Higgs-like boson MC benchmark samples.

4.2.2 Background Samples

QCD multi-jet MC simulations are used to help understand the background from jets and to quantify signal MC mismodelling. Multi-jet events are generated in different samples with different leading jet p_{T} ranges, which are called slices. In each slice, the leading jet p_{T} has an approximately flat distribution. To recover the normal p_{T}

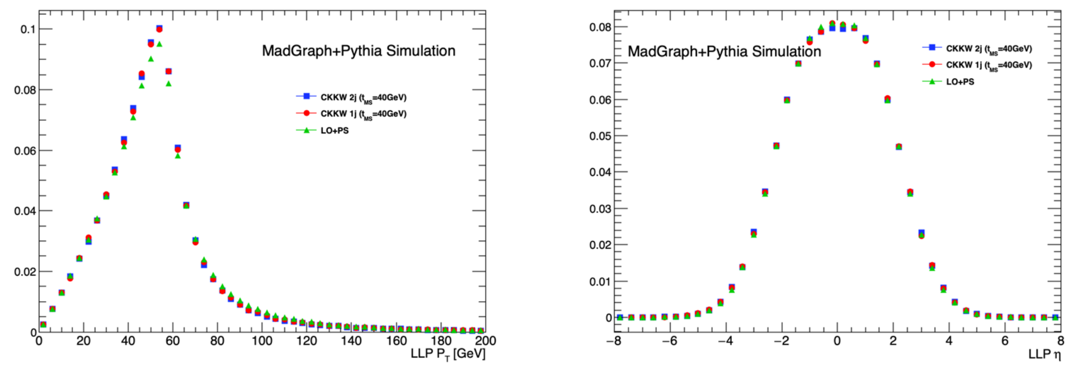

(a) (b)

Figure 4.3: The p_{T} and η distributions of LLPs with mass of 25 GeV from Higgs boson decays. Red and blue are the processes the processes with 1 and 2 ISR jets, respectively, based on the CKKW-L merging scheme. Green is the LO process with parton shower.

distribution, a weight w has to be applied to each event:

$$w = (\text{mcevt\_weight}) \cdot \epsilon_{\text{filter}} \cdot \sigma \cdot \mathcal{L}/N_{\text{evt}}, \tag{4.1}$$

where σ is the cross section of each slice and ϵ_{filter} is the filtering efficiency after flattening out the p_{T} spectrum. Table 4.2 lists the slices and its corresponding cross section.

Slice	Jet p_{T} [GeV]	σ [nb]	Slice	Jet p_{T} [GeV]	σ [nb]
JZ0W	0-20	7.8420×10^{7}	JZ7W	1800-2500	1.6214×10^{-2}
JZ1W	20-60	7.8420×10^{7}	JZ8W	2500-3200	6.2505×10^{-4}
JZ2W	20-60	2.4334×10^{6}	JZ9W	3200-3900	1.9640×10^{-5}
JZ3W	160-400	2.6454×10^{4}	JZ10W	3900-4600	1.1961×10^{-6}
JZ4W	400-800	2.5464×10^{2}	JZ11W	4600-5300	4.2260×10^{-8}
JZ5W	800-1300	4.5536	JZ12W	> 5300	1.0370×10^{-9}
JZ6W	1300-1800	2.5752×10^{-1}			

Table 4.2: Multi-jet slices with their corresponding leading jet p_{T} range and cross sections.

The naming scheme of each jet slice is JZXW, with "X" being the slice number and "W" meaning "weighted". The multi-jet samples are generated by Pythia8 generator using NNPDF23LO PDF set with A14 tune.

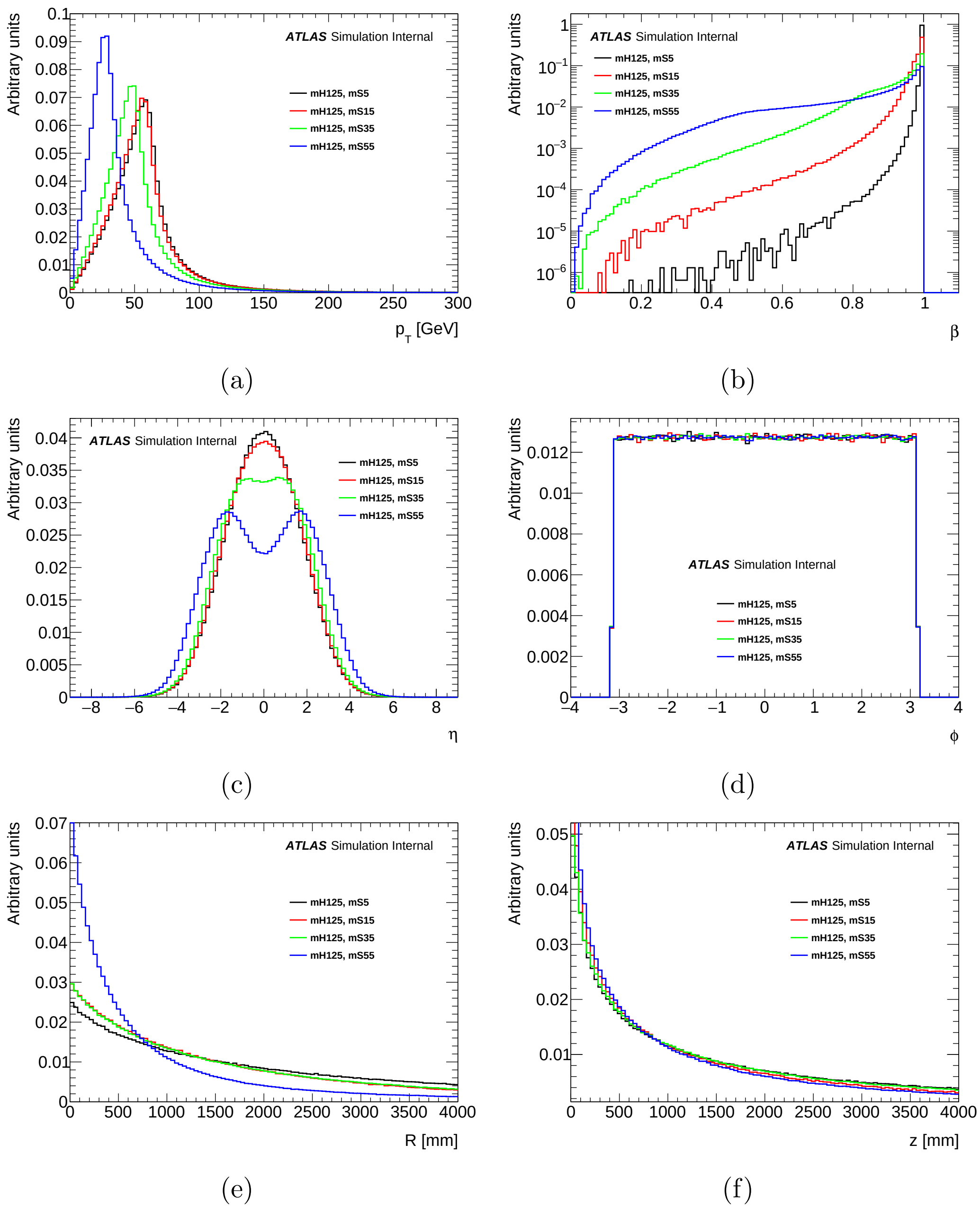

Figure 4.4: Truth-level distributions of the p_T, β, η, ϕ, R and L_z of the LLPs obtained from the generated MC samples of SM Higgs bosons decaying into long-lived scalars with mass shown in the plots. The distributions in each plot have the same normalization.

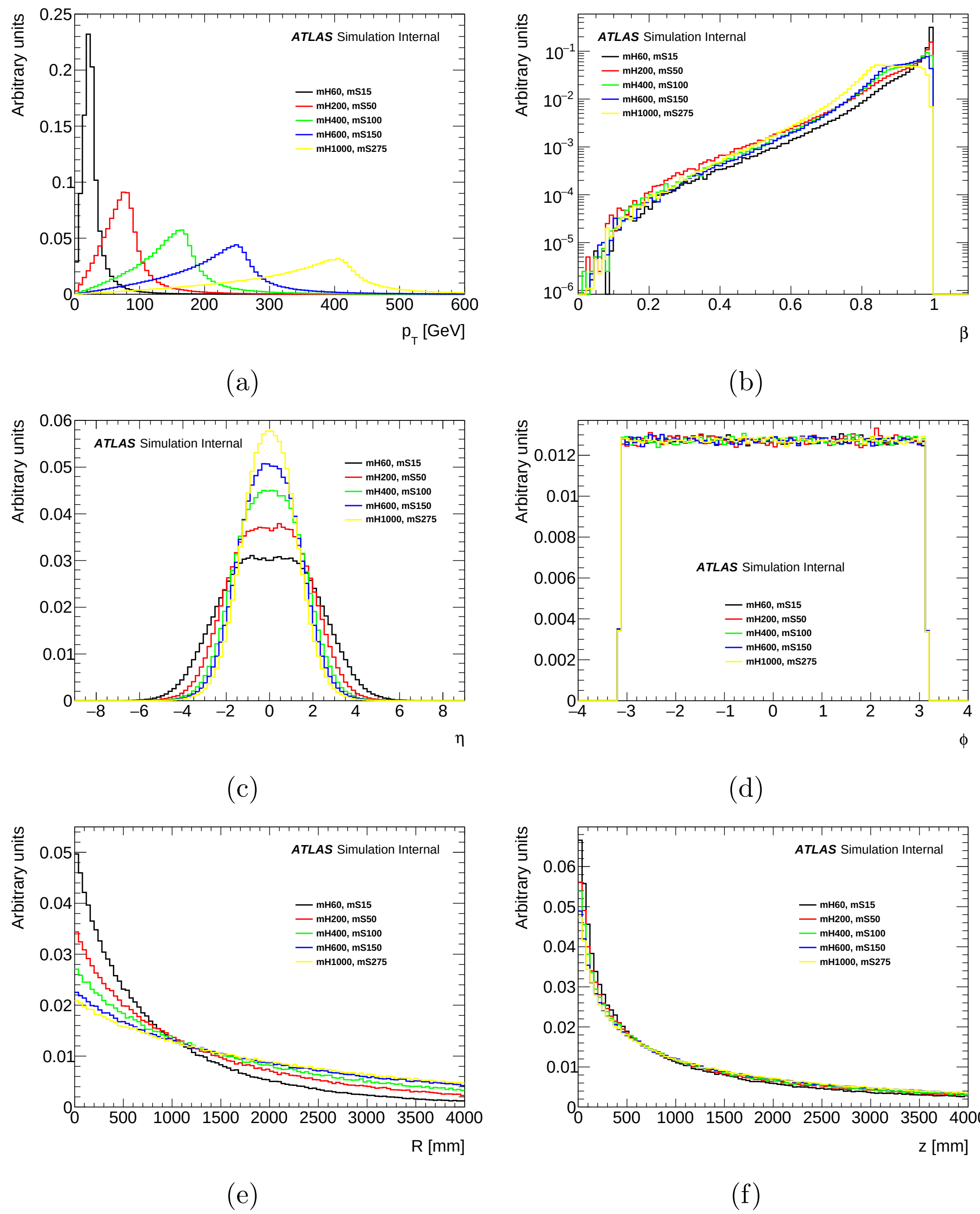

Figure 4.5: Truth-level distributions of the p_T, β, η, ϕ, R and L_z of the LLPs obtained from the generated MC samples of a non-SM Higgs-like boson decaying into long-lived scalars. The distributions in each plot have the same normalization.

CHAPTER 5

The ATLAS Trigger System

5.1 Introduction

At the LHC, the proton-proton bunch crossing occurs every 25 ns (40 MHz). Due to technological limitations, events can't be processed and stored at such a high rate. Thus, a trigger system is needed to decide which events can be used for physics and therefore recorded. For the ATLAS experiment, a two-level trigger system is used. The first level is a hardware-based trigger system called the Level-1 (L1) trigger. The Level-1 trigger uses custom electronics to trigger on reduced-granularity information from the calorimeters and muon detectors which could help identify isolated high transverse-energy (E_{T}) charged leptons, photons, jets as well as missing transverse energy. In Run 2, the L1 trigger system is able to reduce the event rate from 40 MHz to 100 kHz. The decision time for the L1 is fixed at 2.5 μs. The event data accepted by the L1 trigger are readout from the Front-End electronics and then sent to Read-Out Drivers, which perform initial processing and formatting. The Read-Out System takes the input from the Read-Out Drivers and buffers the data upon request to the second level trigger system called the High-Level Trigger (HLT). The HLT is a software-based trigger system that uses particle identification algorithms similar to those used in offline analysis to make selections, taking full granularity information as inputs. The HLT further reduces the event rate from 100 kHz to approximately 1 kHz. Figure 5.1 is the ATLAS Trigger and Data Acquisition (TDAQ) system in Run 2 [125].

5.2 Level-1 Trigger System

The L1 trigger in Run 2 uses several subsystems to make the decisions. The L1 calorimeter (L1Calo) trigger uses energy deposits in the calorimeters to select high-E_{T} objects as well as energy sums of interests. The L1 muon (L1Muon) trigger uses track information provided by muon trigger chambers to identify muon candidates. The L1 topological (L1Topo) trigger selects events by applying topological requirements to several trigger objects received from the L1Calo or L1Muon systems. There are

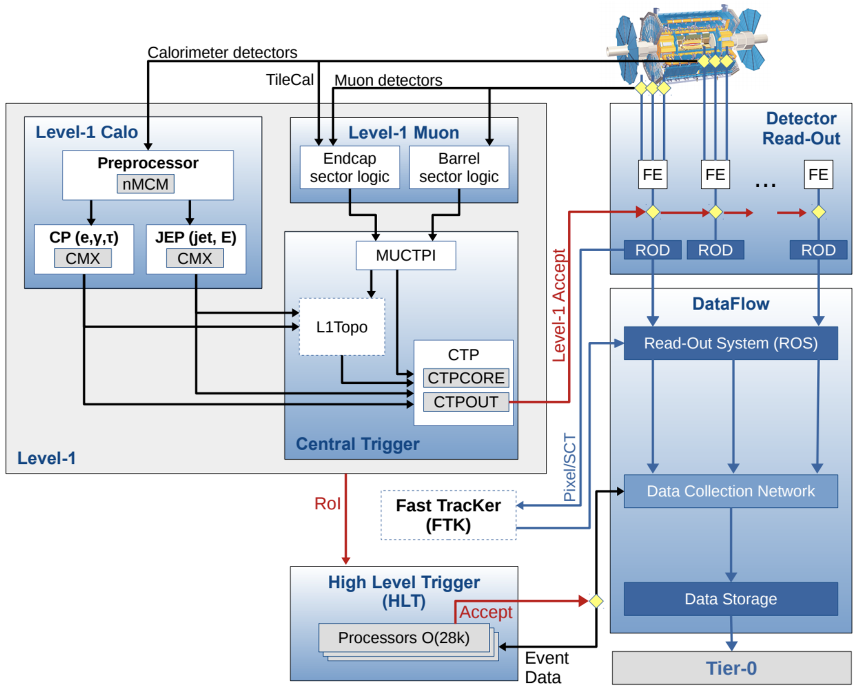

Figure 5.1: The ATLAS Trigger and Data Acquisition (TDAQ) system in Run 2.

other trigger subsystems like the L1 Zero Bias trigger which is used in our analysis for background estimation. The outputs from these triggers are sent to the Central Trigger Processor (CTP) to make the final trigger decision. In Run 2, the CTP can produce a trigger decision of 100 kHz which is a great upgrade compared to the 70 kHz limit in Run 1.

The L1Calo trigger takes input from about 7200 trigger towers of reduced granularity that are formed from calorimeter cells in all the ATLAS electromagnetic and hadronic calorimeters [126]. The trigger towers are mostly 0.1×0.1 in $\Delta\eta$ and $\Delta\phi$, but larger in parts of the endcaps and in the forward calorimeters. The analog data from the trigger towers are firstly sent to the PreProcessor for digitizing, filtering and calibrating. The data then are sent in parallel to the two algorithmic processors: the Cluster Processor (CP) and the Jet/Energy-sum Processor (JEP). The CP system identifies photon, electron and τ-lepton candidates with high transverse-energy above programmable thresholds. The JEP system is designed to identify jets and produce global sums of total, missing and jet-sum E_{T} by using somewhat coarser trigger towers of granularity of 0.2×0.2 in $\Delta\eta$ and $\Delta\phi$ called "jet elements". CP and JEP count hit multiplicities of different types of trigger objects and bits that indicate which thresholds were exceeded are sent to the CTP. The CTP implements a trigger menu based on logical combinations of the results from L1Calo system so as to meet needs of different physics analyses. The algorithms used by CP and JEP can be found in [127].

The L1Muon trigger uses hits from the RPCs (in the barrel) and the TGCs (in the endcaps) to select muon candidates. The muon candidates are categorized into two types: low-p_{T} and high-p_{T}. The low-p_{T} item corresponds to a coincidence of hits in two stations of trigger chambers, while the high-p_{T} item has a coincidence of hits in three stations. Usually the high-p_{T} trigger has lower efficiency compared to the low-p_{T} trigger due to the requirement of the third station in the coincidence.

Because of the increased luminosity and pileup in Run 2, the trigger in the endcaps is more complicated than in the barrel. In the endcaps, additional coincidences of hits are added to reduce background. For example, the coincidence requirements between the TGC stations of the middle layer (the Big Wheel) and TGC Forward/Endcap Inner chambers were added to reduce the background from charged particles emerging from the endcap toroid magnets and beam shielding. A coincidence between TGC chambers and the tile hadronic calorimeter is added to reject fake muons [128]. The p_{T} of a muon is estimated by looking at the degree of deviation of the hit pattern from that of a muon with infinite momentum. There are six pre-defined p_{T} thresholds that have labels like MU20 meaning $p_{\mathrm{T}} > 20$ GeV. MU10 and lower are so-called “low p_{T}” triggers. MU11 and higher are “high p_{T}” triggers. These L1 muon triggers have a geometric coverage of 99% in the endcaps and 80 % in the barrel. After a L1 muon candidate is found, its threshold and detector location information are sent to the CTP to make the trigger decision.

The L1Topo trigger was commissioned in 2016 for Run 2 analyses to help with L1 triggering. Without change, the existing Run 1 L1 trigger system would have seen increased thresholds and prescales applied to trigger items. This would result in significant loss in triggering efficiency for W’s, Z’s, and other physics objects of interest. The L1Topo trigger uses the angular and energy information of each trigger object provided by L1Calo and L1Muon in the event and computes topological angular selections (on $\Delta\eta$, $\Delta\phi$, ΔR, energy in object cone ...) and kinematic selections (on invariant mass, transverse mass, event H_{T} ...) providing a largely improved background rejection [129]. With these selections, the L1Topo can trigger on events with lower energy or even with exotic signatures. The L1Topo trigger is optimized for high speed data transmission. The latency is about 200 ns.

Besides these main trigger systems, there are several specialized L1 triggers. Relevant to this analysis is the Zero Bias Trigger. The Zero Bias trigger fires one revolution after a luminosity trigger. Events selected in this way do not require any parton-parton hard scatter and as such are random. The event rate is heavily prescaled but follows the instaneous luminosity. The Zero Bias trigger is useful for studies of non-collision backgrounds.

5.3 High Level Trigger

The HLT is a software-based system that uses information sent upon receipt of an L1 accept. The HLT runs fast trigger algorithms first to provide early rejections and then runs more precise and CPU-intensive algorithms to make final decision. In Run 2, most of the trigger algorithms were re-optimized to minimize the difference between the HLT and the offline analysis selections in order to reduce inefficiencies. In Run 1, there were separate Level-2 and Event Filter computer clusters. In Run 2, they were combined into a single computing farm of approximately 40000 Processing Units (PUs), which reduces the complexity and allows for dynamic resource sharing between algorithms. The PUs can make a decision typically within 300 ms. In the HLT, there are about 2500 independent trigger chains which are sequences of algorithms starting from feature-extraction algorithms that run within L1 region of interests (RoIs), then followed by higher precision reconstruction, and finally to a hypothesis algorithm that makes a final trigger decision based on the reconstructed features. The HLT has a processing time of about 200 ms. The output rate of the HLT in Run 2 was 1 kHz, a factor of 2.5 higher than in Run 1.

5.4 Muon RoI Cluster Trigger

The Muon RoI Cluster Trigger (`HLT_j30_muvtx_noiso`) is a signature-driven trigger used in this analysis that selects events with jet-like objects in the muon spectrometer. The trigger is efficient for the LLPs decaying to hadronic jets from the outer region of the HCal to the MS middle station. When they decay in the MS, the resulting hadronic showers tend to be reconstructed by the L1 Muon trigger system as a trigger cluster of muon RoIs centered on the LLP line-of-flight. In the barrel, a low-p_{T} muon RoI is generated by requiring a coincidence of hits in at least three of the four layers of the two inner RPC stations. For a high-p_{T} muon RoI, additional hits in at least one of the two layers of the outer RPC station are required. In the endcaps, a low-p_{T}

muon RoI is generated by requiring a coincidence of hits in at least three of the four layers of the two outer TGC stations, while a high-p_{T} muon RoI requires additional hits in two of the three layers of the innermost TGC station. A cluster of muon RoIs is defined as at least three (four) muon RoIs lying within a $\Delta R = 0.4$ radius in the MS barrel (endcaps). The clustering algorithm runs over each of the L1 muon RoIs and can be included in the algorithm more than once in order to maximize the number of RoI clusters found. The algorithm terminates when the number of unused RoIs is less than 3 or the algorithm has been performed three times. As long as one trigger cluster is found, this event would be considered to pass the trigger.

This HLT Muon RoI Cluster Trigger is seeded by the `L1_2MU10` trigger. This means the muon RoIs used to create clusters has to have $p_{\mathrm{T}} \geq 10$ GeV at L1. The p_{T} of a muon RoI is estimated by using the degree of deviation from the RPC/TGC hit pattern expected for a muon with infinite momentum. L1 muon RoIs are formed in a $\Delta\eta \times \Delta\phi = 0.2 \times 0.2$ region ($\Delta\eta \times \Delta\phi = 0.1 \times 0.1$ region) in the barrel (endcaps), and thus a cone with radius 0.4 is appropriate to select groups of RoIs.

When an LLP decays in the MS, it will leave no energy in the ID and calorimeters. A trigger cluster produced in this scenario would be isolated with respect to either calorimeter jets or ID tracks. However, the Muon RoI Cluster Trigger is "noiso", which means that it does not have any isolation requirements with respect to jets or tracks. This means the Muon RoI Cluster Trigger will select both LLP signal and background events. Further offline selection criteria must be applied to reduce the background allowed by this trigger.

5.4.1 Trigger RoI Mismodelling

The previous iteration of this analysis [130] showed that the L1 muon RoI simulation does not fully represent the efficiencies seen in data. Scale factors are applied to the Monte Carlo to correct for differences found with respect to data. Muon scale factors are generally calculated using a tag-and-probe method, using $Z \to \mu\mu$ events [131]. In this instance though, there are multiple muon RoI's clustered in a small cone. This feature can arise from jet punchthrough in the calorimeter where the resulting hadronic shower produced by a jet continues to the MS. This can occur because of the large longitudinal fluctuations associated with hadronic shower formation. The only SM process that contains a similar signature is high-p_{T} multi-jet events in which one of the jets punches through the calorimeters and continues to shower into the MS.

A jet is defined to be punch-through if it has at least 50 muon segments within a ΔR cone of 0.4 with respect to the jet axis. There is not a perfect or standard way to define a punch-through jet. We choose the number of muon segments in the jet cone to be 50, because signal events creating a vertex in the MS have on average at least 50 segments in a ΔR cone of 0.4 with respect to the LLP decay axis. The scale factors in this analysis are determined by performing a data–MC comparison in events passing the HLT_j400 and HLT_j420 triggers and a minimal di-jet selection ($p_{\mathrm{T}} > 30$ GeV, $\log_{10}(E_{\mathrm{HAD}}/E_{\mathrm{EM}}) < 0.5$, JVT > 0.59 if jet $p_{\mathrm{T}} < 60$ GeV). Leading and sub-leading jets are selected for comparison, because they show excellent agreement in all kinematic variables. A subset of leading and sub-leading jets with at least 50 muon segments is selected as a baseline sample of jets with muon spectrometer activity. For this selection, the number of L1 muon RoIs within $\Delta R = 0.4$ of the jet axis is calculated as a function of the leading and subleading jet p_{T}. Figure 5.2 shows the normalised distributions for both data and MC. The ratio of integral of the data and MC distributions with a cut at trigger level (at least 3 RoIs in the barrel and at least 4 RoIs in the endcaps) is calculated. This provides a measure of how many more muon RoIs are found in the cone of a hadronic shower, on average, in data compared to MC.

The MC RoI mismodelling factor is 1.24 ± 0.01 in the barrel and 1.20 ± 0.01 in the endcaps. The difference between barrel and endcaps is not unexpected, because the two regions of the detector use different L1 trigger technologies: RPC's in the barrel and TGC's in the endcap. This mismodelling factor is taken into account as a systematic uncertainty on the signal trigger efficiency (24% for the barrel and 20% for the endcaps).

5.4.2 Trigger Efficiencies

Trigger efficiencies are determined by calculating the fraction of truth LLP decays that produce a muon RoI cluster. A muon RoI cluster is determined to have originated from a given LLP if it is within $\Delta R = 0.4$ of the truth decay axis. The position of the muon RoI cluster is determined by calculating the Euclidean average of all muon RoIs falling in the $\Delta R = 0.4$ cone.

Only LLPs decaying in the fiducial barrel or endcap regions summarised in Table 5.1 are considered. This choice is driven by offline reconstruction.

Figure 5.3 shows the truth-based Muon RoI Cluster trigger efficiencies for LLPs decaying in the barrel and in the endcaps for SM- and non SM-like bosons decaying into long-lived scalars. The dependence on detector geometry can be seen by looking

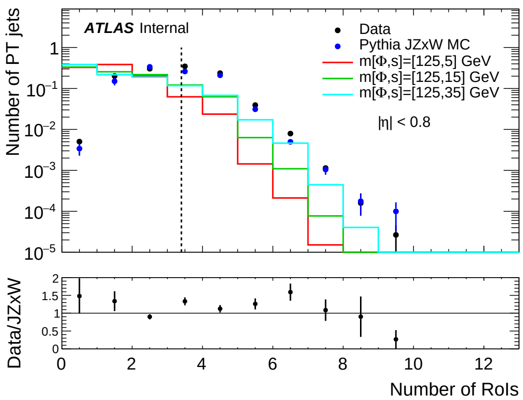

(a)

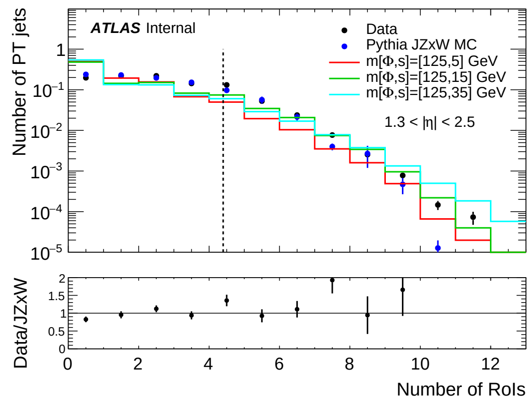

(b)

Figure 5.2: Normalised distributions of number of L1 muon RoIs within $\Delta R = 0.4$ of the jet axis as a function of the leading and subleading jet p_T for barrel (a) and endcaps (b). The black dots show 2015-2018 data. The blue dots are from the multi-jet MC simulation. The solid lines are a few signal benchmark samples. The verticle dashed line shows the cut applied at the trigger level.

Detector	**Fiducial Volume**
MS barrel	$3\,\mathrm{m} < L_{xy} < 8\,\mathrm{m}$, $\lvert\eta\rvert < 0.7$
MS endcaps	$L_{xy} < 10\,\mathrm{m}$, $5\,\mathrm{m} < \lvert L_z\rvert < 15\,\mathrm{m}$, $1.3 < \lvert\eta\rvert < 2.5$

Table 5.1: Fiducial volume definition for the MS barrel and endcap regions.

at the various detector boundaries depicted by dashed lines in the plots. In the barrel the trigger efficiency is very high when the LLP decays close to the end of the hadronic calorimeter ($r \sim 4$ m) and it substantially decreases as the decay occurs closer to the middle station of the muon spectrometer ($r \sim 7$ m). For decays occurring close to the middle station the charged hadrons and photons (and their EM showers) are not spatially separated and are overlapping when they traverse the middle stations (the same reasoning is applicable to decays in the endcap regions).

The dependence of the trigger efficiency on the transverse momentum of the long-lived particle is shown in Figure 5.4.

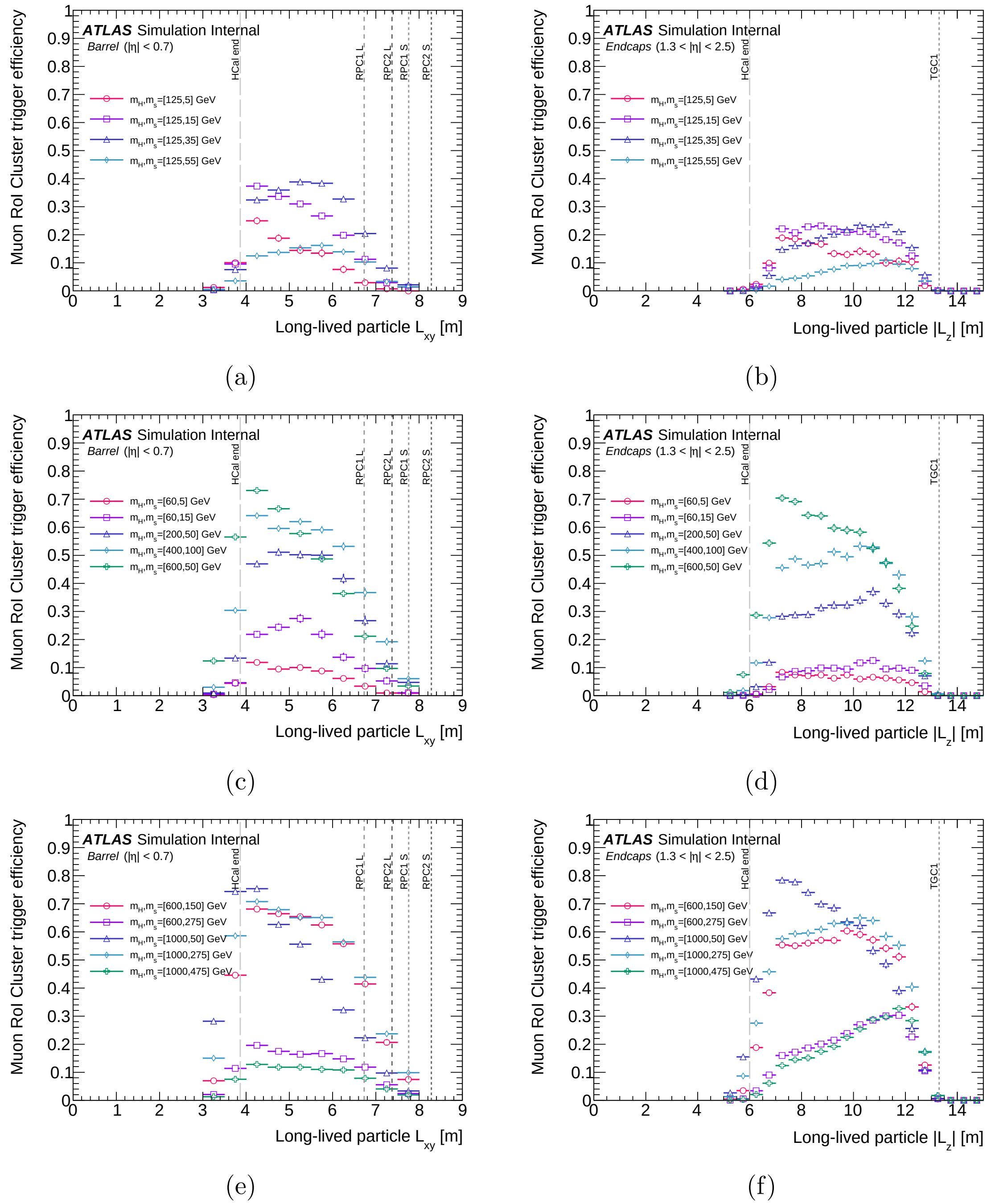

(a) (b) (c) (d) (e) (f)

Figure 5.3: Truth-based Muon RoI Cluster trigger efficiency for (a-b) SM-like Higgs benchmark samples, (c-e) non-SM Higgs benchmark samples. Plots on the left side are for the barrel, while those on the right side are for the endcaps. Efficiencies are computed for events where a single LLP decays in the MS, in order to not contaminate the trigger decision with a second MS decay.

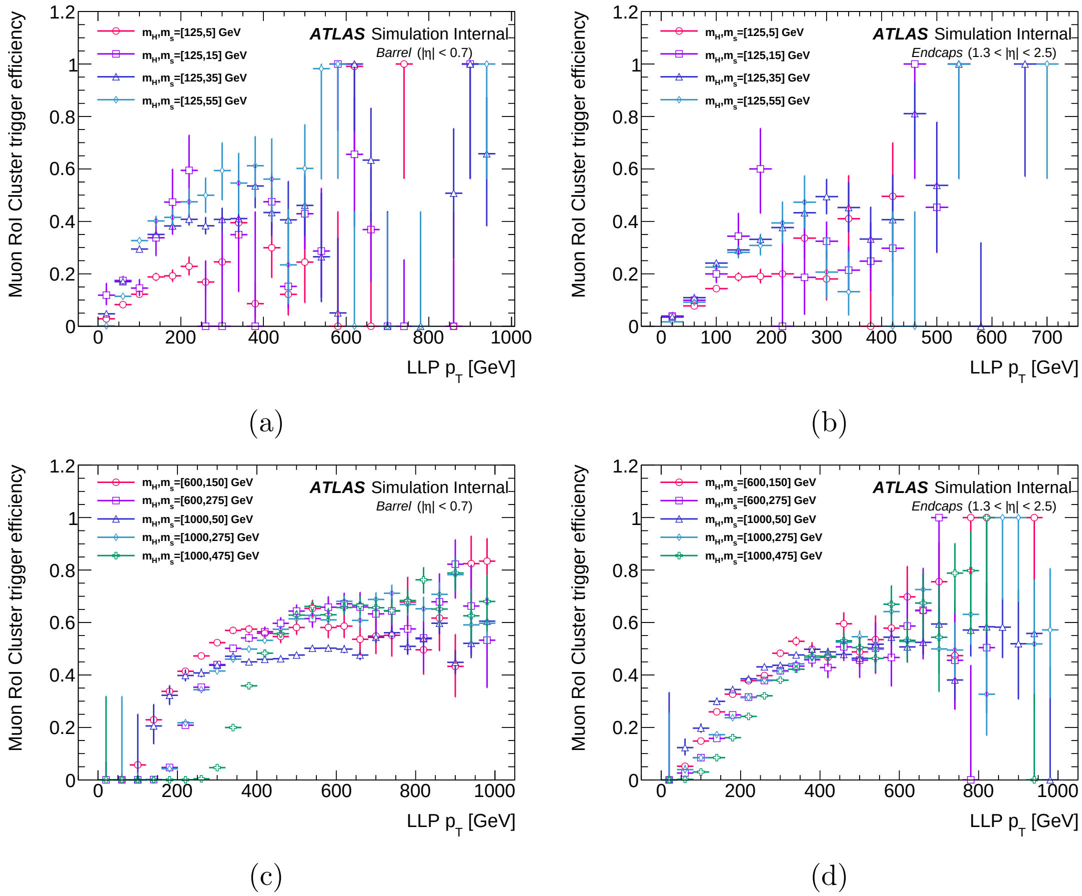

Figure 5.4: Truth-based Muon RoI Cluster trigger efficiency as a function of the LLP p_T for (a-b) SM-like Higgs benchmark samples, (c-e) non-SM Higgs benchmark samples. Plots on the left side are for the barrel, while those on the right side are for the endcaps. Efficiencies are computed for events where a single LLP decays in the MS, in order to not contaminate the trigger decision with a second MS decay.

CHAPTER 6

Event Reconstruction

Proton-proton collisions create a variety of objects in the ATLAS detector, like tracks and vertices in the ID and MS or clusters of cells of energy in the calorimeters. Event reconstruction is a process that constructs these objects based on digitized information from detector elements and then further identifies physics objects such as electrons, muon, and jets that were produced in the collision. In our analysis, LLP signal could leave isolated vertices in the muon spectrometer (MS). The event reconstruction of vertices in the MS is described in this chapter. Events are reconstructed using Athena release 21, which is a data processing framework, for both data and MC simulations in the full Run 2 analysis.

6.1 Track and Vertex Reconstruction

The track reconstruction in the Inner Detector uses an inside-out reconstruction strategy. The steps of reconstruction start by creating clusters in the pixel detectors and the SCT using connected cells, and drift circles in the TRT. A set of artificial neural networks (NN) are used to identify and split merged clusters [132]. The track finding technique uses a three-dimensional object called a space point which is transformed from a combinatorial grouping of clusters. For pixel detectors, the clusters can be directly transformed to space points since they already give a three-dimensional measurement.

For SCT clusters, they can't be transformed to three-dimensional space points directly since they can only give a precise measurement of directions that are orthogonal to the strip's direction. But since the SCT is built with a sandwich structure with two back-to-back strips differed by a stereo angle, the clusters on these two strips can be combined to construct the three-dimensional space points. These three-dimensional space points are used as seeds for track finding. The seeds can be constructed with space points in the pixel detectors only (PPP), the SCT only (SSS) or any combination (PPS or PSS). In Run 2, due to the addition of the IBL layer, seeds need to be associated to one other space point in a different detector layer making a 3+1 space points setup (referred to as PPP+1 etc.).

Once the space point seeds are found, the track finding process begins. The track finding algorithm uses the Kalman filter technique [133] that aims to find all track candidates within the silicon detector. The initial track finding includes real, fake (combinatorics), and duplicate tracks. Some candidates may share same detector hits and thus result in duplicate tracks. Some candidates may be formed from random combinations of hits, which are referred to as fake tracks. In order to eliminate fake and duplicate tracks, an ambiguity solving procedure is employed. The procedure uses a track scoring strategy that assigns a beneficial score to unique tracks with a good fit quality. The procedure further assigns a penalty score to tracks with shared measurements with other candidates and missing but expected measurements given a track trajectory (referred to as holes). Tracks that fail a certain score cut will be neglected for further processing. Successful tracks are extended to the TRT to complete the measurement in the outermost part of the ID. The tracks reconstructed in this inside-out procedure are required to have $p_{\mathrm{T}} > 400$ MeV.

The vertex reconstruction is based on tracks. The tracks to be considered in the vertex construction have to satisfy a series of cuts [134]: $p_{\mathrm{T}} > 400$ MeV; $|\eta| < 2.5$; number of silicon hits ≥ 9 if $|\eta| \leq 1.65$ and ≥ 11 if $|\eta| > 1.65$; IBL hits + B-layer hits ≥ 1; a maximum of 1 shared pixel hit or 2 shared SCT hits; pixel holes = 0; SCT holes ≤ 1. The vertex reconstruction strategy is outlined in the following steps [135]:

1. A seed position of the vertex fit is selected. The x and y coordinates are taken from the beam spot. The z coordinate is calculated as the mode of longitudinal position parameters (z_0) of tracks using the Half-Sample Mode algorithm [136].

2. An iterative primary vertex finding procedure is applied using seed positions and track parameters as inputs. The algorithm uses an iterative χ^2 minimization to find the optimal vertex position. Each input track is assigned a weight:

$$\omega(\hat{\chi}^2) = \frac{1}{1 + \exp(\frac{\hat{\chi}^2 - \chi^2_{cutoff}}{2T})}, \tag{6.1}$$

   where $\hat{\chi}^2$ is the χ^2 value calculated between the closest approach of the track and the vertex position in three dimensions. χ^2_{cutoff} is a constant and T controls the smoothness of the weighting procedure. The vertex position is recalculated using the weighted tracks and this process is iterated. The weight reflects how the track is compatible to the vertex. Tracks with larger χ^2 have lower weights and thus have less impact on the vertex position finding.

3. After last iteration, the tracks that are away from the vertex by more than seven standard deviations will be returned to the pool of unused tracks and are used as inputs for a new vertex finding iteration.

The above steps are repeated until no associated tracks are left or no more vertices can be found by using the remaining tracks. All vertices with at least two tracks are retained. Among them, the vertex with highest sum of squared transverse momenta of the tracks is assumed as the primary vertex associated with the hard scatter process.

6.2 Jet Reconstruction

Jets refer to the showers of particles arising from the hadronization of quarks and gluons. Jets are often seen as proxies for the underlying partons. Jets are reconstructed using charged particle tracks from the Inner Detector and energy deposits in the electromagnetic and hadronic calorimeters.

The first step of the jet reconstruction is to form topological clusters (topo-clusters) using topologically connected cells in the calorimeters. The topo-cluster formation begins by finding a calorimeter cell with a signal significance greater than 4 to serve as the seed. The signal significance is defined as the ratio of energy deposited in the cell to the noise. Both of the cell energy and noise are measured at the electromagnetic (EM) scale, which is the baseline scale that correctly measures the energy deposited in the calorimeter by particles from electromagnetic showers.

Each seed cell is called a proto-cluster. Its neighboring cells with signal significance greater than 2 are added to the proto-cluster. If the neighboring cell is a seed, the two proto-clusters are merged. This topo-cluster algorithm iterates until neighboring cells no longer satisfy the > 2 signal significance.[137].

Then the resulting top-clusters are used as input to jet finding algorithms. The algorithm used in our analysis is the anti$-k_t$ jet clustering algorithm with radius parameter $R = 0.4$ [138]. The anti$-k_t$ algorithm first defines the distance d_{ij} between topo-clusters i and j and the distance between topo-cluster i and the beam (B):

$$d_{ij} = \min(k_{ti}^{-2}, k_{tj}^{-2}) \frac{\Delta_{ij}^2}{R^2}, \tag{6.2}$$

$$d_{iB} = k_{ti}^{-2}, \tag{6.3}$$

where $\Delta_{ij}^2 = (y_i - y_j)^2 + (\phi_i - \phi_j)^2$ and k_{ti}, y_i and ϕ_i are transverse momentum, rapidity and azimuthal angle of topo-cluster i. The algorithm combines topo-cluster

i and j, if d_{ij} is smaller than d_{iB}. Once d_{iB} becomes the smallest parameter, i is defined as a jet and removed from the clustering list. The process continues until no distances are smaller than d_{iB}.

Equation 6.2 shows that the d_{ij} between a hard particle and a soft particle is much smaller than the d_{ij} between two soft particles. As a result, the soft particles tend to group with hard particles before they cluster among themselves. If a hard particle has no hard neighbors within a radius of $2R$, it clusters all the soft particles within a radius of R producing a conical jet. Jet reconstruction with this algorithm is not greatly affected by soft or collinear particles. So, this algorithm is infrared safe. If two hard particles are separated by $R < \Delta_{ij} < 2R$, two jets can still be reconstructed, but at least one of the jets will be partly conical. If the separation Δ_{ij} is less than R, the two hard particles are merged into one single jet.

The jets reconstructed are initially at the EM scale. The hadronic jet energy can be affected by many things including leakage, absorption in the Inner Detector, and pileup. The process of assigning the best energy to a jet is called jet energy scale (JES) calibration. The JES calibration consists of several stages as follows [139]:

- **Origin correction** The 4-momentum of jets are recalculated so that the origin is the hard-scatter vertex rather than the center of the detector. The jet energy is kept constant in the recalculation. This correction helps improve the jet η resolution.

- **Pileup correction** The pileup correction consists of a jet area-based subtraction and a following residual subtraction. Each jet is assigned an area A using ghost association method, where simulated particles with infinitesimal momentum ("ghost" particles) are added uniformly in solid angle to the event before jet reconstruction. The area A is defined to be proportional to the number of ghost particles associated to the jet after clustering using the k_t jet-finding algorithm [140] due to its tendency to include uniform background into jets. The p_{T} density of each jet is given by p_{T}/A. The event-by-event median p_{T} density ρ within $|\eta| < 2.0$ can therefore be obtained. The quantity ρA can be shown to give the global pileup correction to the jet p_{T} in $|\eta| < 2.0$ [141, 142]. For the region $|\eta| > 2.0$, there are additional p_{T} corrections that depend on number of primary vertices N_{PV} and μ. The correction, which is linear with regard to N_{PV} and μ, is also subtracted from the jet pt in this region.

- **Jet energy scale and η calibration** In hadronic showers, a large fraction of energy is not sampled. This invisible energy arises from binding energy, nuclear recoil, and secondary particles that are absorbed or undetected. Transitions between calorimeter subdetectors are also not ideal owing to edge effects and differences in technology and granularity. The jet energy scale and η calibration corrects these problems using MC samples generated with Pythia. The reconstructed jets after origin and pileup corrections are compared to the jets built from simulated particles, which are called truth jets. Comparison of truth jets with reconstructed jets are used to correct E^{reco} from E^{truth} and η^{reco} from η^{truth} [143].

- **Global sequential calibration** This calibration corrects the residual dependencies on the longitudinal and transverse features of jets, as well as the effect of jet punch-through after the above calibrations [139, 144]. MC simulation is used to correct these effects.

- ***In situ* calibration** A final stage of calibration corrects the difference between data and MC simulations. A series of p_{T} balance methods using well-understood reference objects are used. Z/γ+jets events provide correction factors for jets with p_{T} between 20 GeV and 1 TeV. The correction is then further extended to 2 TeV by using multi-jet events. The *in situ* calibration is only applied to data.

To ensure the reconstructed jets are real and associated with the hard-scatter vertex, a set of jet cleaning criteria are applied. The jets reconstructed from background sources are called "fake jets". There are three main sources of background. The first is beam induced background (BIB). Beam proton losses can occur upstream of the interaction point. The cascades created from these proton collisions can give rise to high energy muons that are able to reach the ATLAS detector, which could be reconstructed as fake jets. The second background is cosmic rays. Cosmic ray muon showers reaching the detector have a probability to be reconstructed as jets. The third background source is electronic calorimeter noise. The jet cleaning variables that are designed to remove these backgrounds are as follows:

- $Q_{\text{cell}}^{\text{LAr}}$ is a variable that measures the calorimeter cell signal pulse quality. It is a quadratic difference between the measured pulse shapes in the LAr calorimeter cells and the expected signal pulse shapes from simulation of the electronics response. The average jet quality $\langle Q \rangle$ is then defined as the averaged pulse quality $Q_{\text{cell}}^{\text{LAr}}$ of calorimeter cells in the jet. $\langle Q \rangle$ is normalized to $0 < \langle Q \rangle < 1$.

- $f_{\mathrm{Q}}^{\mathrm{LAr}}$, the fraction of the jet energy measured by the LAr calorimeter cells that have a poor pulse shape quality defined as $Q_{\mathrm{cell}}^{\mathrm{LAr}} > 4000$.

- $f_{\mathrm{Q}}^{\mathrm{HEC}}$, the fraction of the jet energy measured by the Hadronic Endcap Calorimeter (HEC) cells that have a poor pulse shape quality defined as $Q_{\mathrm{cell}}^{\mathrm{LAr}} > 4000$.

- E_{neg}, the sum of energy of all cells in the jet with negative energy that can be caused by sporadical electronic noise fluctuations.

- f_{EM}, the electromagnetic energy fraction, defined as the ratio of the energy deposited in the electromagnetic calorimeter to the total energy of the jet.

- f_{HEC}, the HEC energy fraction, defined as the ratio of the energy deposited in the HEC calorimeter to the total energy of the jet.

- f_{max}, the maximum energy fraction in any single calorimeter layer.

- f_{ch}, the jet charged fraction, defined as the ratio of the scalar sum of the p_{T} of the tracks coming from the primary vertex matched to the jet divided by the jet p_{T}.

Figure 6.1 shows the distributions of $\langle Q \rangle$, $f_{\mathrm{Q}}^{\mathrm{LAr}}$, $f_{\mathrm{Q}}^{\mathrm{HEC}}$ and f_{ch} for data samples enriched in both good jets and fake jets. Figure 6.2 shows the distribution of E_{neg}, f_{EM}, f_{HEC} and f_{max} in good jet enriched samples for both data and multi-jet MC and a fake jet enriched data sample [145]. In this analysis, the fake jets are identified by the BadLoose selection. The jets that satisfy at least one of the following BadLoose criteria are considered bad and are not used as jet candidates:

- $f_{\mathrm{HEC}} > 0.5$ and $|f_{\mathrm{Q}}^{\mathrm{HEC}}| > 0.5$ and $\langle Q \rangle > 0.8$

- $E_{\mathrm{neg}} > 60$ GeV

- $f_{\mathrm{EM}} > 0.95$ and $f_{\mathrm{Q}}^{\mathrm{LAr}} > 0.8$ and $\langle Q \rangle > 0.8$ and $|\eta| < 2.8$

- $f_{\mathrm{max}} > 0.99$ and $|\eta| < 2$

- $f_{\mathrm{EM}} < 0.05$ and $f_{\mathrm{ch}} < 0.05$ and $|\eta| < 2$

- $f_{\mathrm{EM}} < 0.05$ and $|\eta| > 2$

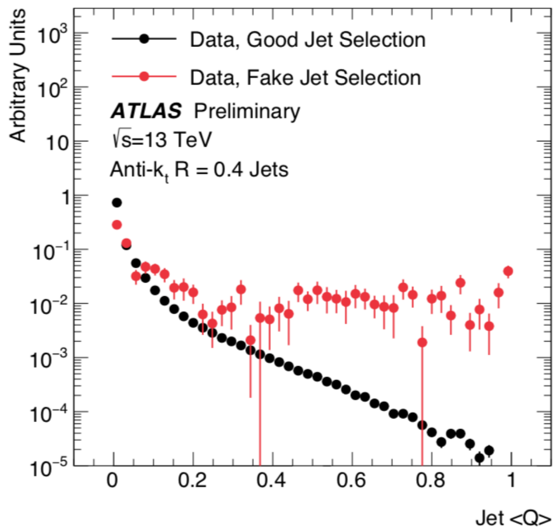

(a)

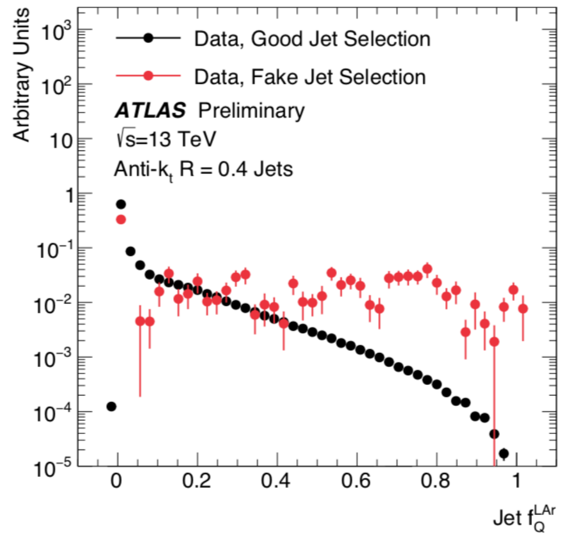

(b)

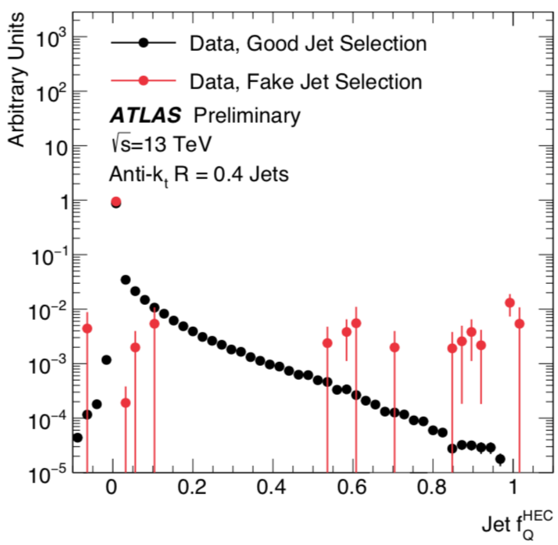

(c)

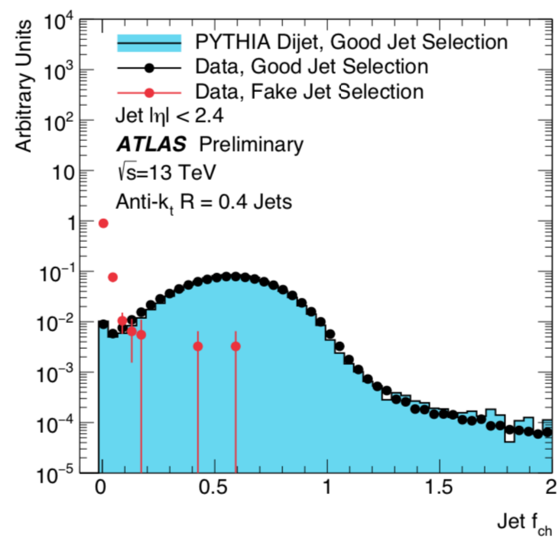

(d)

Figure 6.1: Distributions of $\langle Q \rangle$, $f_{\mathrm{Q}}^{\mathrm{LAr}}$, $f_{\mathrm{Q}}^{\mathrm{HEC}}$ and f_{ch} in both good jet enriched and fake jet enriched data sample. Black data points represent good jet selection. Red data points represent fake jet selection.

Besides these cleaning variables, a jet vertex tagger (JVT) is used in our analysis to exclude the jets from pileup. The JVT is calculated based on the variable $R_{p_{\mathrm{T}}}$ and corrJVF. The variable $R_{p_{\mathrm{T}}}$ is a ratio of the scalar p_{T} sum of all tracks that are matched to the jet and the hard-scatter primary vertex divided by the fully calibrated jet p_{T}. The value of $R_{p_{\mathrm{T}}}$ falls rapidly for jets associated with pileup. The variable corrJVF

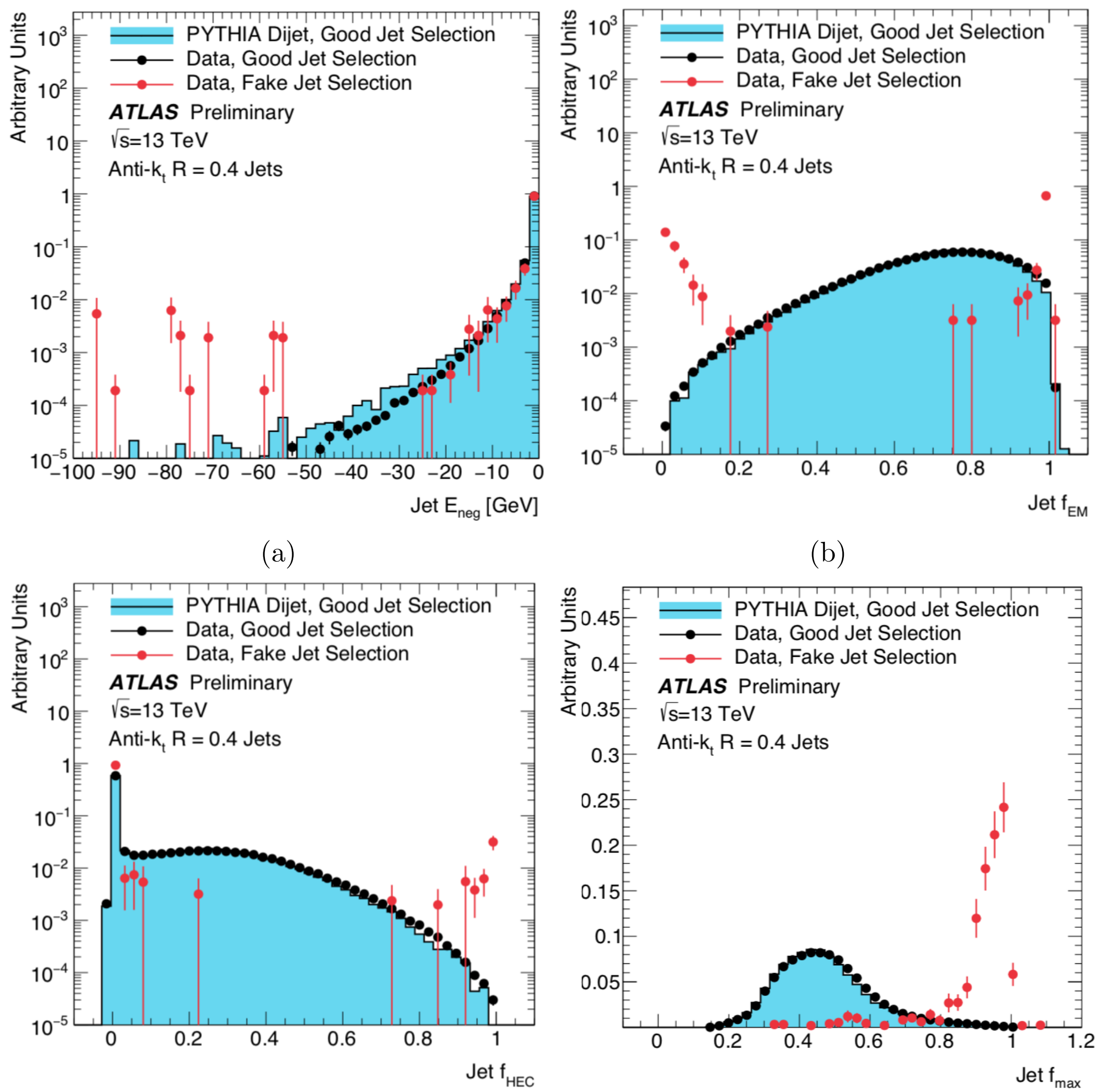

(a) (b) (c) (d)

Figure 6.2: Distributions of E_{neg}, f_{EM}, f_{HEC} and $f_{\max}$ in good jet enriched samples for both data and multi-jet MC and fake jet enriched data sample. Black data points represent good jet selection. Red data points represent fake jet selection. Blue histogram is multi-jet MC with good jet selection.

measures the number of tracks associated with jets originating from primary vertex, compared to the total number of tracks coming from all the interaction vertices. The JVT is calculated using $R_{p_{\mathrm{T}}}$ and corrJVF as a 2-dimensional likelihood, based on a k-nearest neighbor algorithm [146]. The JVT has values between 0 and 1. JVT $= -0.1$ is assigned to jets with no associated tracks. Generally speaking, a lower value of

JVT is more likely to be a jet associated with pileup.

6.3 Missing Transverse Momentum $E_{\mathrm{T}}^{\mathrm{miss}}$ Reconstruction

The vector sum of momentum in the transverse plane of all particles in an event should be zero since the proton beam is in z direction. Experimentally this is not the case with real event reconstruction. Weakly interacting stable particles like neutrinos are invisible to the detectors, so as are weakly interacting long-lived particles that decay outside of ATLAS. Particles that pass through non-measuring materials or escape the detector acceptance can be poorly reconstructed or not at all. These cases all contribute to a non-zero momentum sum in the transverse direction. The missing transverse momentum $E_{\mathrm{T}}^{\mathrm{miss}}$ is reconstructed based on the following equation [147]:

$$E_{\mathrm{T}}^{\mathrm{miss}} = \left\| -\sum_{\text{electrons}} \boldsymbol{p}_{\mathrm{T}}^{e} - \sum_{\text{photons}} \boldsymbol{p}_{\mathrm{T}}^{\gamma} - \sum_{\tau-\text{leptons}} \boldsymbol{p}_{\mathrm{T}}^{\tau} - \sum_{\text{muons}} \boldsymbol{p}_{\mathrm{T}}^{\mu} - \sum_{\text{jets}} \boldsymbol{p}_{\mathrm{T}}^{\text{jet}} - \sum \boldsymbol{p}_{\mathrm{T}}^{\text{soft}} \right\|. \tag{6.4}$$

The first five terms are referred to as hard terms that are from fully calibrated objects. The $E_{\mathrm{T}}^{\mathrm{miss}}$ reconstruction has a commonly used sequence, starting with electrons, then followed by photons, hadronically decaying $\tau-$leptons and finally jets. Since these objects could share the same calorimeter cells, an overlap removal procedure is carried out, starting with photons. Muons are reconstructed using only tracks in the ID and MS, but they have corrections on the energy lost in the calorimeter. Muon-jet overlap removal is also applied. The specific selections on these objects can be found in [147].

The last term in Equation 6.4 is referred to as the soft term. It is reconstructed from the transverse momentum measured by the detector but not matched to any of the hard reconstructed objects. It can be reconstructed by either calorimeter-based or track-based algorithms. The latter is used in our analysis and the corresponding soft term is called track soft term (TST). The $E_{\mathrm{T}}^{\mathrm{miss}}$ that uses track soft term is called TST $E_{\mathrm{T}}^{\mathrm{miss}}$. In the TST, the $\boldsymbol{p}_{\mathrm{T}}^{\text{soft}}$ is contributed by high-quality tracks originating from the hard-scatter vertex, but not associated with electrons, τ, jets and muons that contribute to the $E_{\mathrm{T}}^{\mathrm{miss}}$ reconstruction. The $E_{\mathrm{T}}^{\mathrm{miss}}$ reconstructed in this way is not sensitive to pileup since tracks are accurately matched to the primary vertex. However, it does not account for the contributions from soft neutral particles.

6.4 MS Vertex Reconstruction

6.4.1 Standard Muon Segment Reconstruction

Muon segments are locally reconstructed three-dimensional segments within different stations in the muon spectrometer. Muon segments are subsequently used as seeds for track finding in the MS. A segment is reconstructed as a straight line based on the hits in the MDT chamber. Muon segment candidates are initially formed from a pair of MDT hits, one in each multilayer. The pair of hits are required to be close enough so that they are associated with a real physical trajectory. The line formed by the pair of hits is required to roughly point to the interaction vertex in order to reduce background and random hit combinations. The drift circles from each of the two MDT hits form four lines that are used as four segment seeds, only one of which can serve as segment candidate.

The four seed lines are next extrapolated to the remaining tubes to find all associated hits. A hit is considered to be associated to the line when its drift circle is within 1.5 mm of the line. Seed lines with at least three associated hits are fitted as a straight line by minimizing

$$\chi^2 = \sum_{i=1}^{n} \frac{(R_i - r_i)^2}{\sigma_i^2}, \tag{6.5}$$

where R_i is the distance between line and MDT central wire, and r_i and σ_i are the measured drift radius and its error. The minimization procedure is described in [148]. The segments with the best χ^2 probability greater than 0.05 are kept. If a newly found segment is close to any previously found segment, the segment with less hits or same hits but larger χ^2 will be removed.

In order to improve the segment quality, fake segments from random combination of hits have to be removed. The corresponding criteria is given by the χ^2 per degree of freedom (χ^2/ndf). If a segment is found to have a χ^2/ndf greater than 10, the hit that has the largest χ^2 is removed from the segment and the χ^2/ndf is recalculated. This procedure is repeated until the χ^2/ndf is less than 10 or the number of associated hits is less than 3. For the latter case, the segment is removed from the list. The segments remaining after this procedure are next matched to the hits in the trigger chambers (RPCs in the barrel, TGCs in the endcaps). The number of matched trigger hits is used as one of the quality handles. When segments have shared MDT hits, only the segment with highest quality is kept.

In this analysis, the number of muon segments is used as a measure of activity in the MS. It is also used in the definition of punch-through jets.

The muon segment itself is not used for the MS vertex reconstruction because the standard MS tracking algorithm is designed for a relatively clean environment. The typical number of MDT hits left by a muon traversing the MS is about 20-25. However the number of cuts created by charged particles associated with a displaced vertex easily exceeds 100. With the large number of combinatorics, it is not possible for the standard reconstruction algorithm to combine segments from multiple chambers into a single track. Therefore a standalone MS vertex reconstruction method based on tracklet-finding technique is used [149], which is described in the following sections.

6.4.2 Tracklet Reconstruction

MS tracklets are constructed using segments in two MDT multilayers. Each segment is found separately in a multilayer and requires three or more associated MDT hits and a minimum χ^2 fit in the case of multiple segments. All the segments are required to have a χ^2 probability greater than 0.05.

To find the single multilayer segments that belong to the same charged particle, segments in multilayer 1 (ML1) are matched to segments in multilayer 2 (ML2) using parameters $\Delta\alpha$ and Δb. The parameter $\Delta\alpha$ is the angle between the two segments. For the tracks outside a magnetic field, the segments will match as a straight line. For the tracks inside the magnetic field, it is just the bending angle and can be used to measure the track momentum resulted from low-p_{T} particles. The parameter Δb measures the distance between two segments. For two matched segments, the $|\Delta b|$ is required to be less than 3 mm. A small $|\Delta b|$ means that the selected two segments are tangent to the same drift circle and thus are consistent with being from the same charged particle. The paired set of single-multilayer segments is called a tracklet. Figure 6.3 shows an example of tracklet with its parameters.

The segments from each multilayer are refit into a single straight line segment if $|\Delta\alpha| < 12$ mrad. For chambers that are outside the magnetic field, the BIS and BOS MDT chambers in the MS barrel and the chambers in the MS endcap, paired segments are always combined and refitted by using at least 6 MDT hits with the innermost and outermost hits used as seeds.

In the MS barrel, the momentum of a tracklet is calculated by a formula with form $p = k/|\Delta\alpha|$, which is derived from a $|\Delta\alpha|$ versus $1/p$ fit using a sample of pions that traverse the chamber. The parameter k varies for different barrel chambers.

Different barrel chambers can have different spacing between MDT multilayers and thus have different allowed maximum bending angle. Due to the bending restriction, the minimum tracklet momentum is determined to be about 0.8 GeV. The uncertainty of momentum measurement is propagated from $\Delta\alpha$ measurement, which can be shown to be $\sigma_p/p \approx 0.06 \cdot p/\text{GeV}$ in the BML chambers, $\sigma_p/p \approx 0.08 \cdot p/\text{GeV}$ in the BMS chambers and $\sigma_p/p \approx 0.13 \cdot p/\text{GeV}$ in the BOL and BIL chambers.

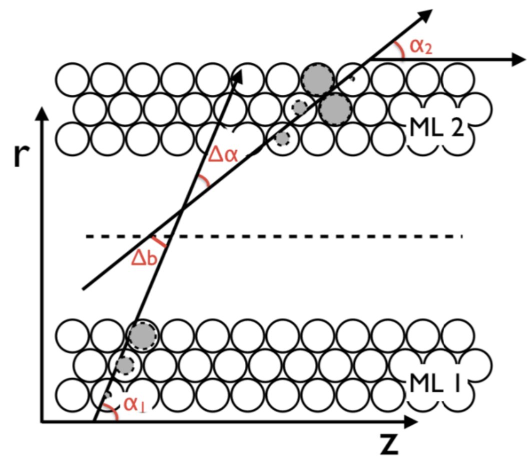

Figure 6.3: An example of tracklet reconstructed in a MS barrel MDT chamber. The parameter $\Delta\alpha$ is the angle between the two segments, which is defined as $\Delta\alpha = \alpha_1 - \alpha_2$. The parameter Δb is defined to be the minimum distance from one segment at the middle plane of the MDT chamber to the other straight line segment.

6.4.3 MS Barrel Vertex Reconstruction

Most of the MDT chambers in the MS barrel are immersed in a magnetic field whereas all the MDT chambers in the MS endcap are outside the magnetic field [149]. Trackets formed in the barrel will bend whereas those in the endcap will not. Thus the MS vertex reconstruction algorithms differ between barrel and endcap. The MS vertex reconstruction in the barrel is described in the following steps. Figure 6.4 shows schematically how the MS vertex reconstruction in the barrel is performed. [149].

1. The tracklets are grouped into clusters of tracklets using a cone algorithm. The position of each tracklet is used as a seed. Tracklets within $\Delta\eta = 0.7$ and $\Delta\phi = \pi/3$ of the tracklet cluster direction are added to the cluster. The position of the cluster center is updated each time a new tracklet is added. After the

iteration on the tracklets reaches its end, the position of the cluster is calculated to be the average position of the tracklets in the cluster. This process continues until there are less than three unused tracklets or no more clusters with more than three tracklets can be found.

2. The line-of-flight of the decaying particle is calculated in θ and ϕ. The θ variable is determined by the line connecting the interaction point and the centroid of all tracklets in the cluster. The ϕ determination is more complicated due to the lack of precision in the MDT ϕ measurement. The ϕ direction is initially calculated as an approximate value by averaging the ϕ coordinates of the tracklets in the cluster. This approximate ϕ and the η of the line-of-flight are then used to constuct a cone with radius of $\Delta R = 0.6$. Finally, the ϕ direction of the line-of-flight is determined by averaging all the RPC-phi measurements within this cone. The ϕ resolution (~ 50 mrad) determined in this way is still much larger than the resolution in θ (~ 12 mrad).

3. Due to the lack of precision in ϕ measurement and the inhomogeneous magnetic field, the vertex reconstruction in barrel is performed in a single $r - z$ plane where the line-of-flight lies. All the tracklets in the cluster are mapped onto this $r - z$ plane by a ϕ rotation.

4. A series of lines that are parallel to the z direction are constructed in the $r - z$ plane starting from $r = 3.5$ m. They are placed in a way such that the spacing between two adjacent lines is uniform along the direction of the line-of-flight. The spacing is set to be 25 cm. As a result, there are 15 lines at $\eta = 0$ and 22 lines at $|\eta| = 1$.

5. The tracklets are back-extrapolated in the $r - z$ plane, using their momentum and charge information and the full magnetic map, to the series of lines defined in the previous step.

6. At each line, if there are more than three extrapolated crossing it, the weighted average z position of these tracklets where they cross the line is calculated and used as the position of a vertex candidate. A χ^2 minimization procedure is preformed. The vertex is assumed to be located at the average z position. The χ^2 probability associated to this assumption and the χ^2 value for each tracklet are calculated. If the χ^2 probability is less than 0.05, then the tracklet with the largest χ^2 is removed. Then the vertex position and total χ^2 are recalculated.

This procedure iterates until the vertex has a χ^2 probability greater then 0.05 or there are less than 3 tracklets remaining.

7. The reconstructed vertex is chosen to be the vertex with largest number of tracklets. If there are two vertices with the same number of tracklets, the vertex with minimum χ^2 is the reconstructed vertex. The position of the vertex is the radius and z position calculated on the line.

8. In the search for LLP, the reconstructed vertex has additional criteria based on the number of MDT and RPC hits to ensure good quality. These are described later in the event selection.

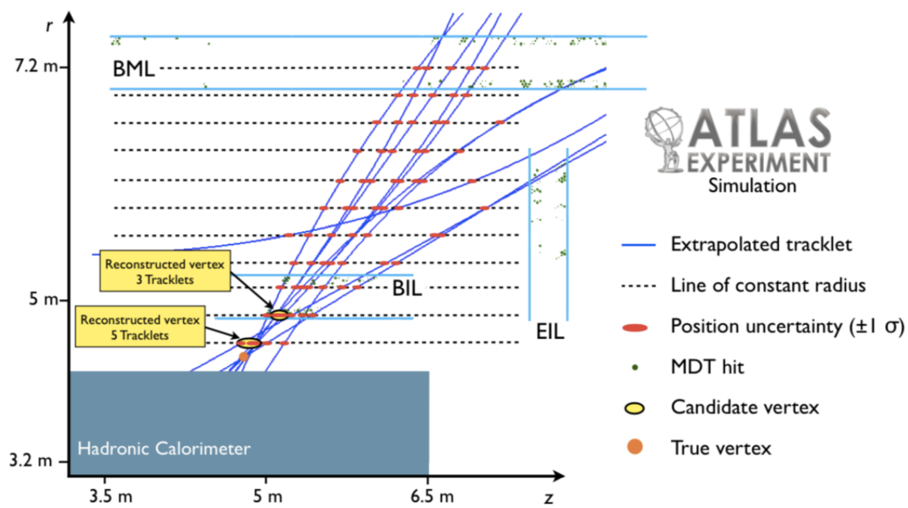

Figure 6.4: Schematic plot that shows the MS vertex reconstruction in the barrel.

6.4.4 MS Endcap Vertex Reconstruction

In the MS endcap region, a toroid magnet is placed between the inner (EIL) and middle (EML) MDT stations. Charged particles passing through the toroid are of course bent, however the tracklets created by the charged particles are straight lines since the MDT's themselves are not immersed in a magnetic field. For the MS vertex reconstruction in the MS endcap region, the tracklets must be back-extrapolated into the toroid. The measurements of tracklets are only made after the magnet. The MS vertex reconstruction in this region is described below. Figure 6.5 shows a schematic figure of the reconstruction process.

1. Tracklets are grouped into tracklet clusters using the same algorithm that is used in the barrel.

2. The line-of-flight is determined in the same way as that used in the barrel. The only difference is that TGC-phi measurements are used instead of RPC-phi measurements to calculate the ϕ direction. The resolution in the line of flight in both θ and ϕ are comparable to that in the barrel.

3. The straight-line tracklets in the cluster give equations of form $b_i = -r\tan\theta_i + z$ with two constraining parameters on the i-th tracklet in the cluster: b_i which is intercept and θ_i which is the angle of the tracklet. The position of the vertex is then found using a least squares regression fit. The formula that give the vertex position are [150]

$$r_{\text{vertex}} = \frac{(\sum \frac{\tan\theta_i}{\sigma_i^2})(\sum \frac{b_i}{\sigma_i^2}) - (\sum \frac{\tan\theta_i}{\sigma_i^2})(\sum \frac{b_i\tan\theta_i}{\sigma_i^2})}{(\sum \frac{1}{\sigma_i^2})(\sum \frac{\tan^2\theta_i}{\sigma_i}) - (\sum \frac{\tan\theta_i}{\sigma_i^2})^2}, \tag{6.6}$$

$$z_{\text{vertex}} = \frac{(\sum \frac{\tan\theta_i}{\sigma_i^2})(\sum \frac{b_i}{\sigma_i^2}) - (\sum \frac{1}{\sigma_i^2})(\sum \frac{b_i\tan\theta_i}{\sigma_i^2})}{(\sum \frac{1}{\sigma_i^2})(\sum \frac{\tan^2\theta_i}{\sigma_i}) - (\sum \frac{\tan\theta_i}{\sigma_i^2})^2}. \tag{6.7}$$

4. The distance of closest approach between the tracklet and the vertex is checked. If the farthest distance is larger than 300 mm, the corresponding tracklet is removed and the vertex position refitted. The iteration continues until the farthest distance is less than 300 mm.

5. The MS endcap vertex is considered to be reconstructed if it has at least three tracklets. If multiple vertices are found, only the vertex with largest number of tracklets is kept. The position of the vertex is determined by r_{vertex}, z_{vertex} and ϕ calculated in the previous steps. Figure 6.5 shows the vertex reconstruction in the MS endcaps [149].

6. As for MS vertices found in the barrel, selection criteria using the number of MDT and TGC hits are applied in the event selection to ensure the vertex is of high quality.

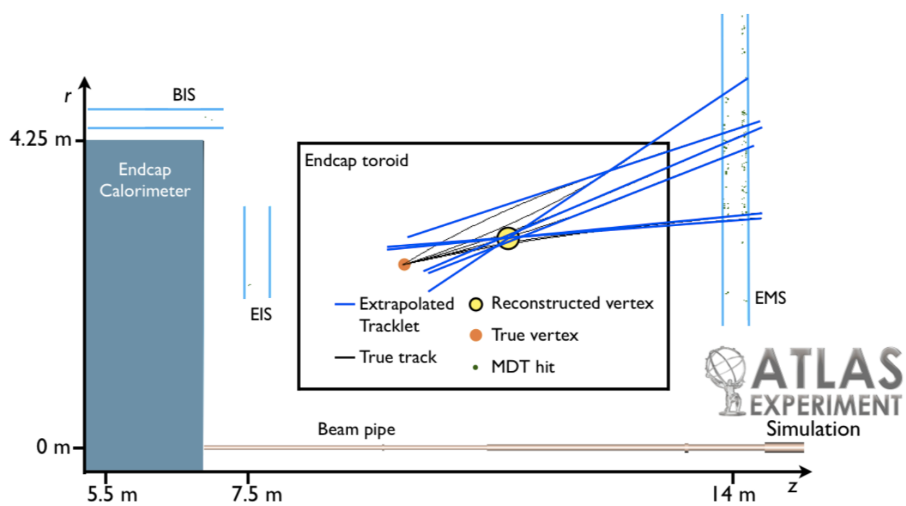

Figure 6.5: Schematic plot that shows the MS vertex reconstruction in the endcaps.

CHAPTER 7

MS Vertex Identification

This thesis studies the LLP decays that produce hadronic showers in the muon spectrometer. The shower width and track multiplicities depend on the LLP signal mass and boost. The vertex associated with the LLP decay can be reconstructed using the method described in Section 6.4. Background processes can also give rise to vertices in the MS that will be reconstructed as well. The goal of this chapter is to provide the criteria that select the vertices from LLP decays and suppress the vertices from background processes, and thus enhance the signal significance.

7.1 MS Vertices in the Overlap Region

For a decay that occurs in the overlap region between the MS barrel and endcaps, its hits are split between barrel and endcap vertex reconstructions. This results in two problems. First, fewer hits are used in each reconstruction and thus result in a reduced vertex reconstruction efficiency in this region. Second, there is a chance that two vertices are reconstructed from a single LLP decay, since both of the barrel and endcap reconstruction algorithms are applied.

Figure 7.1a shows the fraction of duplicated vertices that are from a single LLP decay as a function of η. It can be seen that most of the duplicated vertices are from the barrel-endcap overlap region. Figure 7.1b shows the vertex reconstruction efficiency with good vertex criteria, described in the next section, applied and duplicated vertices removed. The reconstruction efficiency is relatively low in the region 0.8 - 1.3 and is thus removed from the analysis to reduce uncertainties.

From the background study in 2015+2016 analysis, the probability to have a punch-through jet in the transition region between the barrel and endcap calorimeters ($0.7 < |\eta| < 1.2$) that does not satisfy the criteria used for jet isolation is much higher than in other regions of the detector [130]. To reduce the risk of background contamination from punch-through jets, the vertices reconstructed in the region between $0.7 < |\eta| < 1.2$ are not considered. Considering both the overlap region in the MS and transition region in the calorimeter, the detector fiducial region excludes $0.7 < |\eta| < 1.3$.

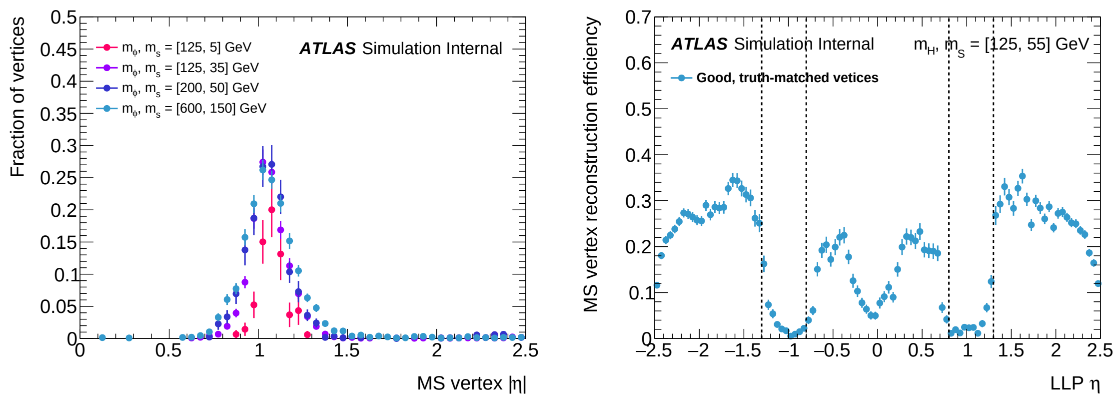

(a) (b)

Figure 7.1: (a) Fraction of vertices coming from long-lived particles that match *two* otherwise good MS vertices. The simulated MC samples shown are scalar decays (ϕ) to lighter scalar pairs (s). (b) The efficiency to reconstruct a MS vertex as function of η, for the sample that has a Higgs decaying to 55 GeV scalar pairs. Dashed lines mark the excluded region.

7.2 Good Vertex Criteria

The vertices reconstructed in the MS can either originate from a displaced signal decay or from background processes. To achieve good signal efficiency while suppressing background processes, a set of good vertex criteria (GVC) based on detector hits and track and jet isolation are used.

7.2.1 Number of Associated Hits

The number of hits recorded by the MDT, RPC and TGC chambers is used as a criteria to distinguish the signal vertices from the background from noise bursts and punch-through jets. The displaced hadronic decay in the MS is expected to create more activity in the detectors than the punch-through jet in general. Therefore, a minimum number of hits is required for MDT chambers as well as RPC and TGC trigger chambers. The minimum hit criteria applied are: $N_{\mathrm{MDT}} > 300$ and $N_{\mathrm{RPC+TGC}} > 250$. These criteria are applied in the vertex reconstruction algorithm.

Besides punch-through jets, noise bursts can happen occasionally in a localized area in the MS. Noise bursts will lead to a large number of hits in the MDT chambers, the combination of which can lead to a large probability that a vertex is reconstructed. In order to reject these vertices from noise, a maximum number of number of MDT hits is required. The number of MDT hits in the vertex cone is set to be $N_{\mathrm{MDT}} < 3000$. The upper limit of 3000 MDT hits is selected such that most of the signal events satisfy this selection. The minimum number of RPC/TGC hits also helps suppress the background from noise, since the noise burst in the MDT chamber is not expected to be coherent with the noise in the muon trigger chambers.

7.2.2 Vertex Isolation Criteria

Jets that punch through the calorimeter can create vertices in the muon spectrometer that mimic the behavior of signal LLPs. These jets will leave a fraction of energy deposited in the calorimeters and tracks in the inner detector if the hadronized particles are charged. However, a neutral LLP will deposit no energy in the detector, until it decays in the MS, which means that the signal vertex should not be associated with any calorimeter jets or tracks. Therefore, the angular distance between the MS vertex and calorimeter jets and ID tracks can be used to reject the background events from punch-through jets. A set of isolation criteria are developed in this analysis based on this property. The vertices considered for establishing the isolation criteria have to satisfy the η and number of hits requirements described in the previous sections.

The first criteria isolate vertices from calorimeter jets. Only jets with $\log_{10}(E_{\mathrm{HAD}}/E_{\mathrm{EM}}) < 0.5$ are considered for isolation. This is so that the true vertices from displaced decays that occur near the end of the calorimeters are not rejected. Additionally, a set of jet criteria (jet $p_T > 30$ GeV and JVT > 0.59 if jet $p_T < 60$ GeV) are applied to select the jets used for vertex-jet isolation. These selections are used to prevent true vertices from being discarded by the isolation with jets from pileup or underlying events.

Vertex isolation criteria are applied using using jets and ID tracks. The isolation criteria are defined using a ΔR cone around the vertex. The isolation criteria using jets are given in Table 7.1. The criteria are determined by comparing reconstructed vertices in signal MC and multi-jet MC samples. Figures 7.2a and 7.3a show how the signal and background acceptances change with varying isolation cone size in both the barrel and the endcaps.

The isolation criteria using tracks further suppresses the number vertices formed by punch-through jets. Jets may be poorly reconstructed due to calorimeter cracks but will still leave a signature in ID. The tracks considered for vertex isolation are chosen to have transverse momentum $p_{\mathrm{T}} > 5$ GeV. The isolation cone size is set to be 0.3 for barrel and 0.6 for endcaps. The isolation criteria are given in Table 7.1.

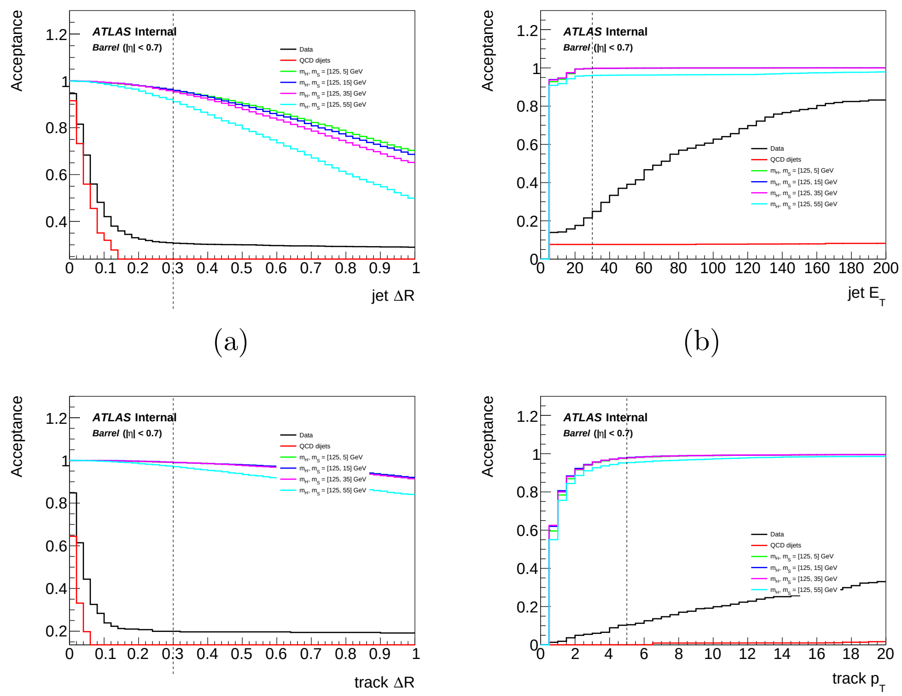

(a) (b)

(c) (d)

Figure 7.2: Signal and background acceptance for vertices that pass jet or track isolation criteria in the barrel. The dashed line is actual isolation cut used in the analysis. Muti-jet slices JZ4W-JZ12W are used in the plots.

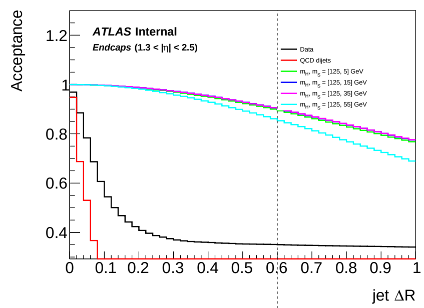

(a)

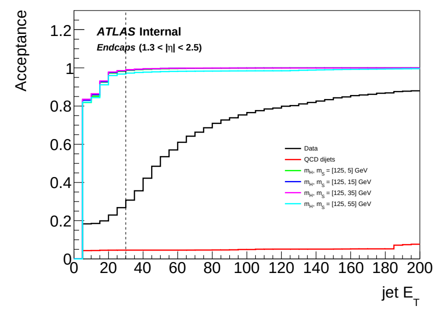

(b)

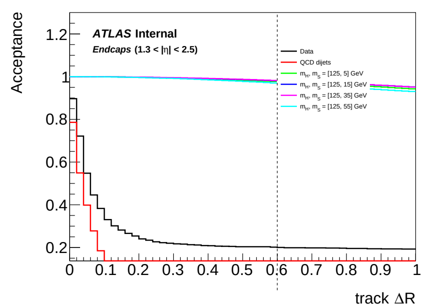

(c)

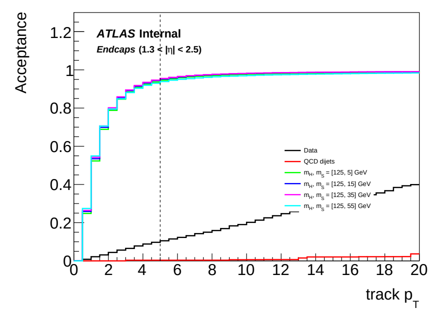

(d)

Figure 7.3: Signal and background acceptance for vertices that pass jet or track isolation criteria in the endcaps. The dashed line is actual isolation cut used in the analysis. Muti-jet slices JZ4W-JZ12W are used in the plots.

Requirement	Barrel	Endcap
MDT hits	$300 \leq N_{\mathrm{MDT}} < 3000$	$300 \leq N_{\mathrm{MDT}} < 3000$
RPC/TGC hits	$N_{\mathrm{RPC}} \geq 250$	$N_{\mathrm{TGC}} \geq 250$
> 5 GeV track isolation	$\Delta R > 0.3$	$\Delta R > 0.6$
Track $\lvert\Sigma\vec{p_{\mathrm{T}}}\rvert$ in 0.2 cone	< 10 GeV	< 10 GeV
> 30 GeV jet isolation	$\Delta R > 0.3$	$\Delta R > 0.6$

Table 7.1: Summary of criteria for good MS vertices in the barrel and endcap regions.

Figure 7.2c and 7.3c show how signal and background acceptance vary with the ΔR used for track isolation.

A second isolation criteria is used to remove the cases where there is no high-momentum track, but the sum of track momentum in a small cone around the vertex is very high. The vector sum of momentum of all tracks within a $\Delta R = 0.2$ cone is calculated. If the size of the p_{T} sum is greater than 10 GeV, the vertex is rejected.

The good vertex criteria are summarized in Table 7.1. Figure 7.4 shows the vertex reconstruction efficiencies in the barrel and endcaps before and after application of the GVC, for the highest and lowest scalar produced by a 125 GeV Higgs-like boson.

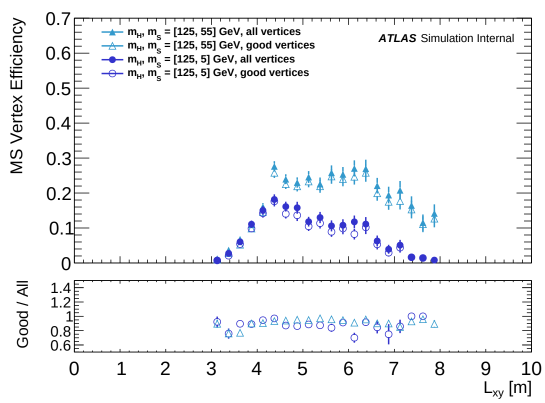

(a)

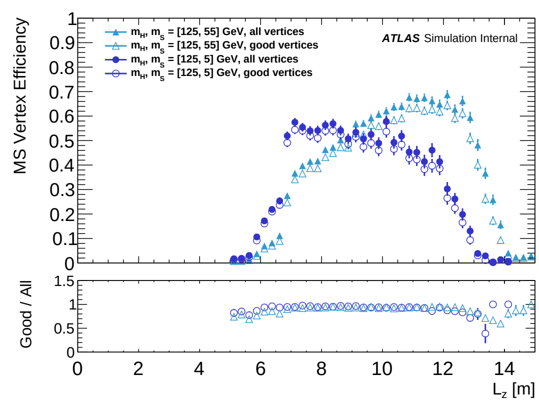

(b)

Figure 7.4: The MS vertex reconstruction efficiency in the barrel (a) and endcaps (b), with and without the good vertex criteria applied, for the highest and lowest scalar produced by a 125 GeV Higgs boson.

7.3 Vertex Reconstruction Efficiency

The vertex reconstruction efficiency is defined as the fraction of LLPs that leave a vertex that satisfies the good vertex criteria in the MS fiducial region. In the barrel, the vertex reconstruction is calculated as a function of the radial position L_{xy} and in the endcaps, it is calculated as a function of the longitudinal position L_z. Their distributions are shown in Figure 7.5. The dashed lines represent various detector boundaries.

For the scalar mass of 5 GeV the barrel MS vertex reconstruction efficiency is about 20% near the calorimeter face ($r \sim 4$ m) and it substantially decreases as the decay occurs closer to the middle station ($r \sim 7$ m). For decays occurring close to the middle station the vertex reconstruction efficiency decreases because the charged hadrons and photons (and their corresponding EM showers) are not spatially separated and are overlapping when they traverse the middle station. This reduces the efficiencies for track reconstruction and, consequently, vertex reconstruction. The efficiency slightly increases for scalar masses of 15 and 35 GeV, but then drops for a scalar mass of 55 GeV. This is due to the smaller boost received by the higher mass scalar that leads to a spatially wider decay and correspondingly lower efficiency.

The efficiency for reconstructing vertices in the MS endcaps reaches 70%. Because there is no magnetic field in the region in which endcap tracklets are reconstructed, the vertex reconstruction algorithm does not have the same constraints that are present in the barrel. Consequently, the endcap vertex reconstruction is more efficient for signal events, but also less robust in rejecting background.

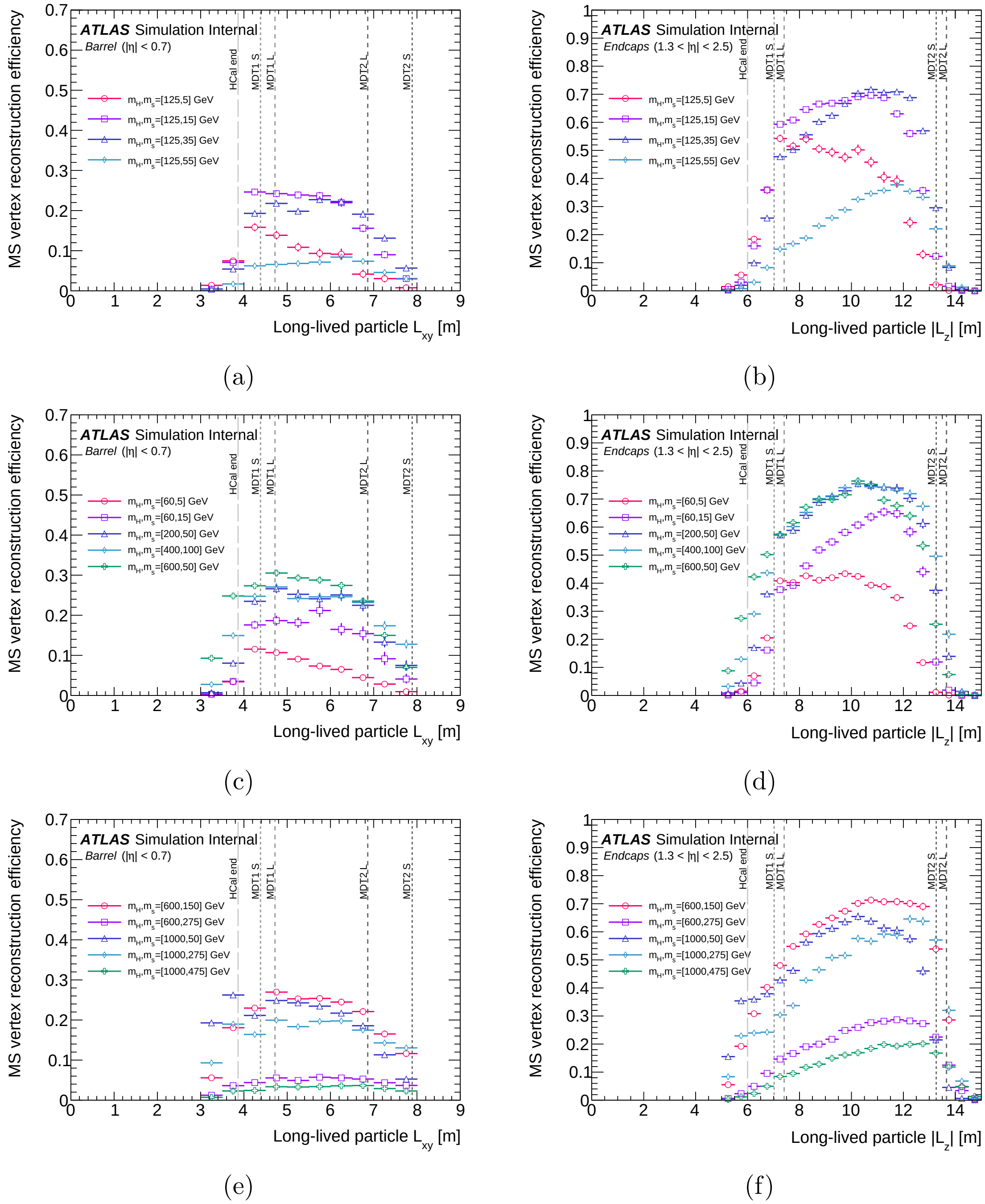

Figure 7.5: Truth-based MS vertex reconstruction efficiency for (a-b) SM-like Higgs benchmark samples, (c-f) non-SM Higgs benchmark samples. Plots on the left side are for the barrel, while those on the right side are for the endcaps.

7.4 Vertex Residuals

The vertex reconstruction algorithms in the MS barrel and endcaps are tuned to maximize the vertex-finding efficiency at the expense of vertex-position resolution [149]. As a result, the position of a vertex does not necessarily represent the actual decay position of the corresponding LLP accurately. To study the accuracy of the vertex position, the vertex position residuals, which are defined as the difference between the truth LLP decay position and the reconstructed vertex position, are calculated for several distance and angular variables. Figures 7.6, 7.7, 7.8, 7.9 show the distribution of vertex residuals in η, ϕ, R, and z for various Higgs and scalar boson samples.

The residuals behavior in the barrel and endcaps are different due the different strategies used for the reconstruction. In the endcaps, there is a large shift away from zero observed in R and z distributions. This is because, for an LLP that decays inside the endcap toroid, its line-of-flight is preserved while the trajectories of its decay products are bent by the magnetic field. The tracklets are reconstructed after the magnetic region. When they are back-extrapolated back into the magnetic field as straight lines, the vertex position will be shifted to larger values of $|z_{\mathrm{reco}}|$ and r_{reco} with respect to the true position. This shift decreases when the decay occurs near the outer edge of the toroid where the charged decay products are bent less and the straight line approximation is more valid.

To quantitatively describe the accuracy of the vertex position, the resolution of each variable for each signal sample is calculated in the barrel and endcap region respectively and listed in Tables 7.2, 7.3, 7.4, 7.5. The vertex resolution is defined as the RMS of the normalized residual distribution, where the normalized residual is the residual divided by the truth decay position for each of the variables η, ϕ, R, and z.

Sample	η	ϕ	R [m]	z [m]
$m_{\mathrm{H}} = 125$ GeV, $m_{\mathrm{S}} = 5$ GeV	0.058	0.084	0.25	0.34
$m_{\mathrm{H}} = 125$ GeV, $m_{\mathrm{S}} = 15$ GeV	0.072	0.081	0.20	0.34
$m_{\mathrm{H}} = 125$ GeV, $m_{\mathrm{S}} = 35$ GeV	0.094	0.096	0.19	0.46
$m_{\mathrm{H}} = 125$ GeV, $m_{\mathrm{S}} = 55$ GeV	0.11	0.12	0.22	0.68

Table 7.2: Summary of resolutions for MS vertices in the barrel region for various Higgs samples.

Sample	η	ϕ	R [m]	z [m]
$m_{\mathrm{H}} = 125$ GeV, $m_{\mathrm{S}} = 5$ GeV	0.033	0.072	0.28	0.25
$m_{\mathrm{H}} = 125$ GeV, $m_{\mathrm{S}} = 15$ GeV	0.037	0.076	0.27	0.24
$m_{\mathrm{H}} = 125$ GeV, $m_{\mathrm{S}} = 35$ GeV	0.050	0.10	0.31	0.24
$m_{\mathrm{H}} = 125$ GeV, $m_{\mathrm{S}} = 55$ GeV	0.072	0.14	0.41	0.24

Table 7.3: Summary of resolutions for MS vertices in the endcap region for various Higgs samples.

Sample	η	ϕ	R [m]	z [m]
$m_{\mathrm{H}} = 60$ GeV, $m_{\mathrm{S}} = 15$ GeV	0.071	0.081	0.18	0.30
$m_{\mathrm{H}} = 200$ GeV, $m_{\mathrm{S}} = 50$ GeV	0.10	0.099	0.23	0.57
$m_{\mathrm{H}} = 400$ GeV, $m_{\mathrm{S}} = 100$ GeV	0.12	0.10	0.25	0.70
$m_{\mathrm{H}} = 600$ GeV, $m_{\mathrm{S}} = 150$ GeV	0.13	0.11	0.28	0.80
$m_{\mathrm{H}} = 1000$ GeV, $m_{\mathrm{S}} = 275$ GeV	0.14	0.12	0.32	1.03

Table 7.4: Summary of resolutions for MS vertices in the barrel region for various scalar samples.

Sample	η	ϕ	R [m]	z [m]
$m_{\mathrm{H}} = 60$ GeV, $m_{\mathrm{S}} = 15$ GeV	0.043	0.083	0.30	0.23
$m_{\mathrm{H}} = 200$ GeV, $m_{\mathrm{S}} = 50$ GeV	0.055	0.10	0.33	0.26
$m_{\mathrm{H}} = 400$ GeV, $m_{\mathrm{S}} = 100$ GeV	0.066	0.11	0.37	0.29
$m_{\mathrm{H}} = 600$ GeV, $m_{\mathrm{S}} = 150$ GeV	0.073	0.12	0.39	0.30
$m_{\mathrm{H}} = 1000$ GeV, $m_{\mathrm{S}} = 275$ GeV	0.093	0.13	0.45	0.33

Table 7.5: Summary of resolutions for MS vertices in the endcap region for various scalar samples.

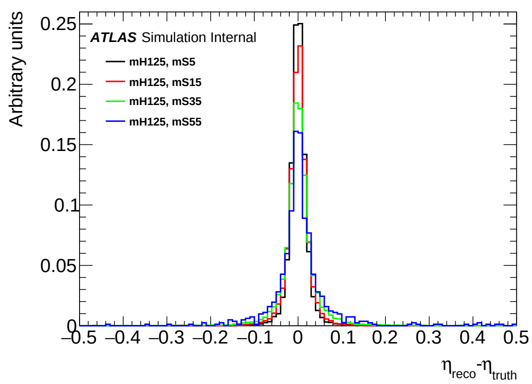

(a)

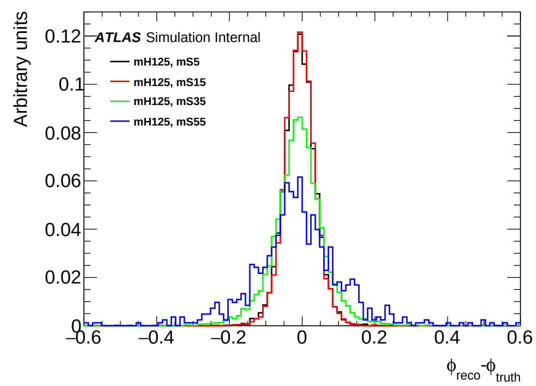

(b)

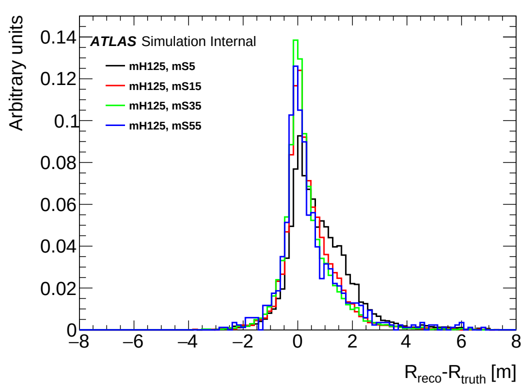

(c)

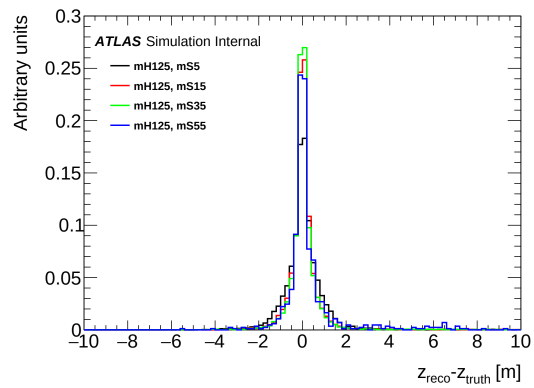

(d)

Figure 7.6: Residuals in (a) η, (b) ϕ, (c) R, and (d) z coordinates for decays in the MS barrel for various Higgs samples.

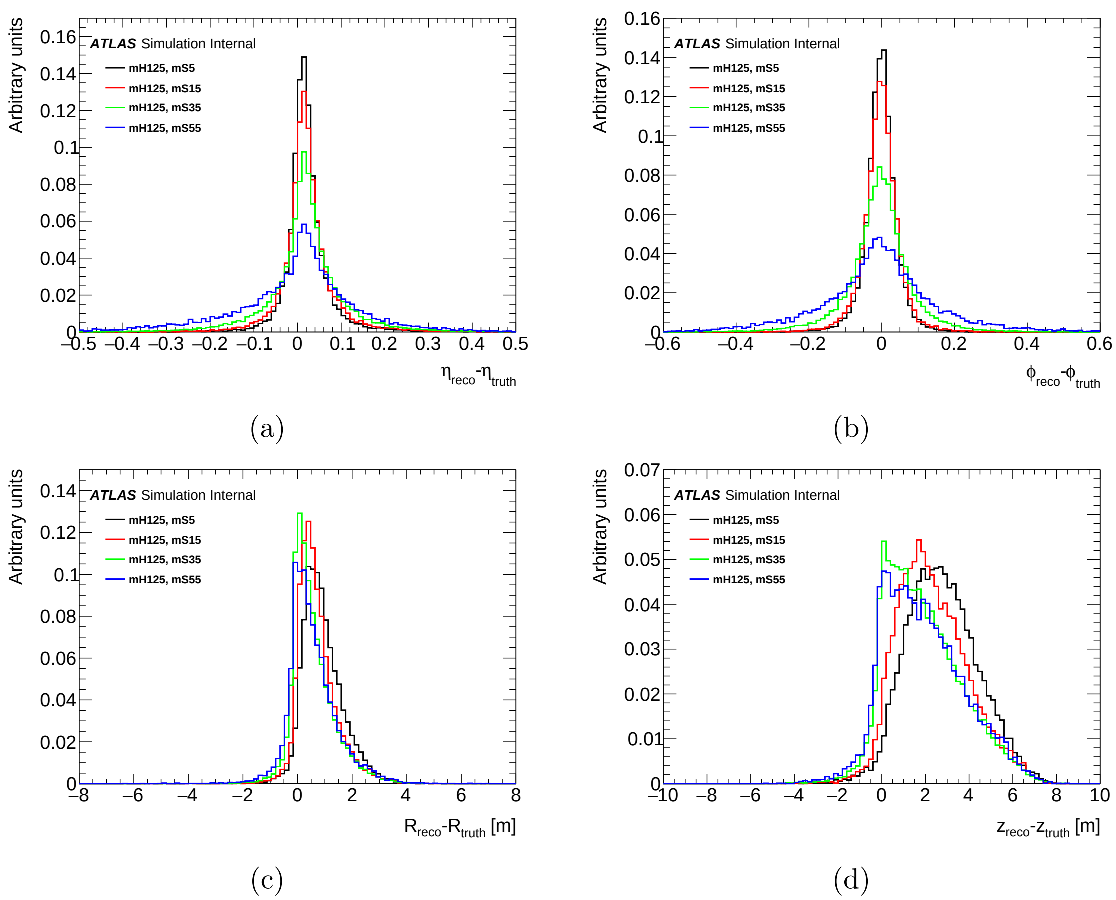

Figure 7.7: Residuals in (a) η, (b) ϕ, (c) R, and (d) z coordinates for decays in the MS endcap for various Higgs samples.

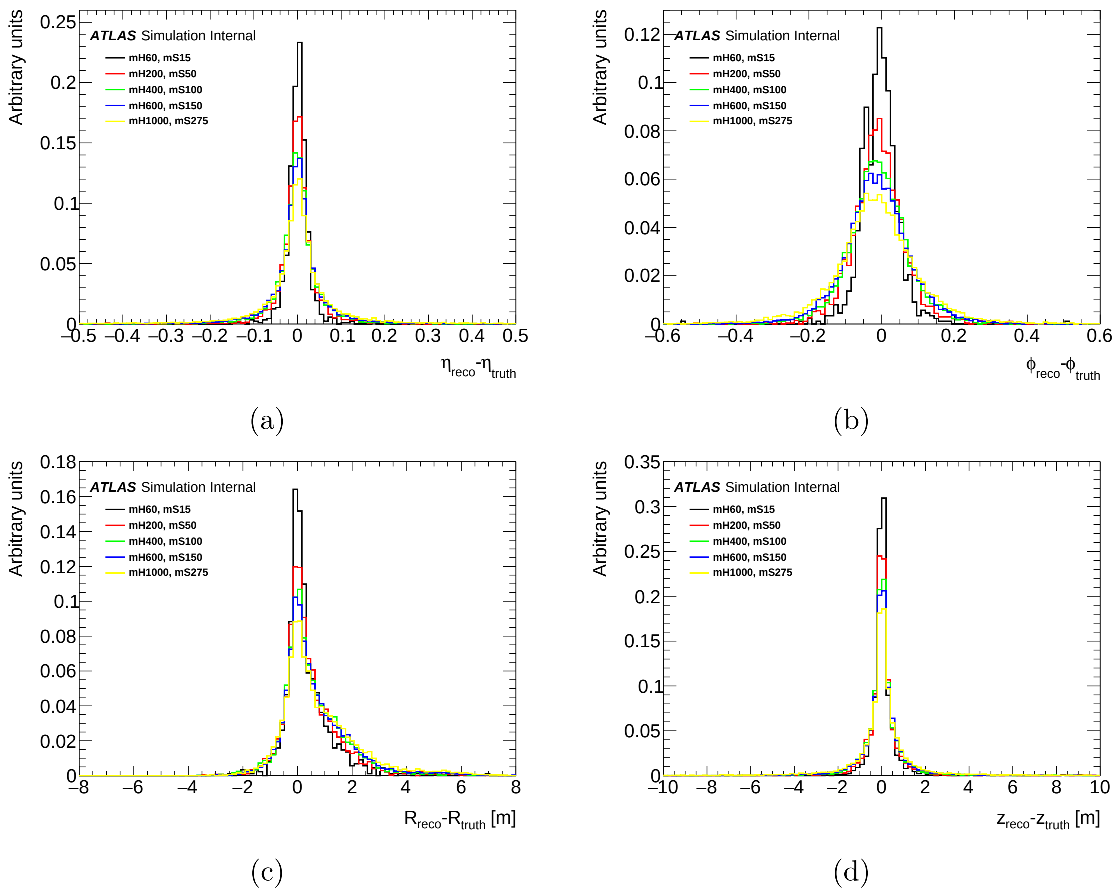

Figure 7.8: Residuals in (a) η, (b) ϕ, (c) R, and (d) z coordinates for decays in the MS barrel for various scalar samples.

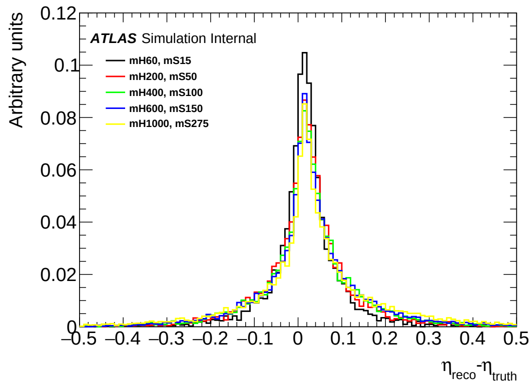

(a)

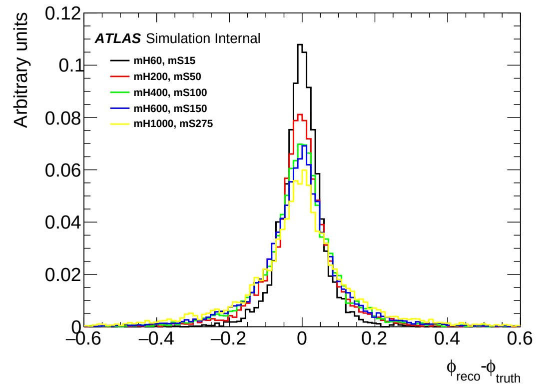

(b)

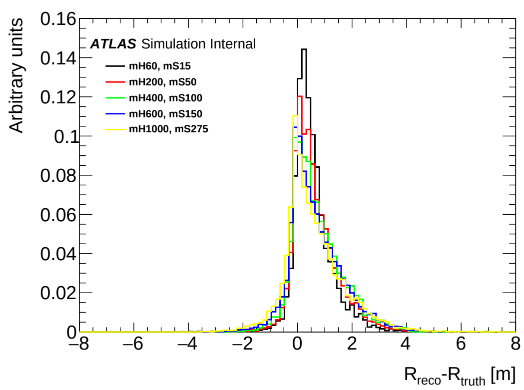

(c)

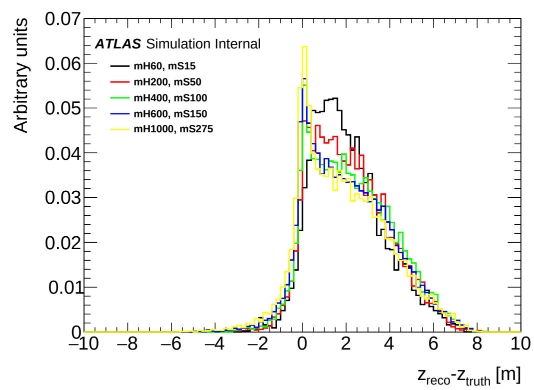

(d)

Figure 7.9: Residuals in (a) η, (b) ϕ, (c) R, and (d) z coordinates for decays in the MS endcap for various scalar samples.

7.5 Scale Factors in the Vertex Reconstruction

Possible mismodelling in the MC simulation could lead to a vertex reconstruction efficiency that is different than the one in the real detector. The effects of mismodelling can be quantified by comparing the average number of tracklets in a cone surrounding a punch-through jet in data and QCD multi-jet MC. Events in this study are required to pass the HLT_j400 and HLT_j420 triggers. Also, only the leading and subleading jets in p_{T} for each event are considered. The jet selection criteria are: $p_{\mathrm{T}} > 30$ GeV, $\log_{10}(E_{\mathrm{HAD}}/E_{\mathrm{EM}}) < 0.5$, JVT > 0.59 if jet $p_{\mathrm{T}} < 60$ GeV. Punch-through jets are defined by the requirement of having more than 50 associated muon segments within a ΔR cone of 0.4.

Figure 7.10 shows the tracklet distribution in a $\Delta R = 0.4$ cone around the punch-through jet in the MS barrel and endcap. At least three tracklets are required in the barrel and at least 4 tracklets are required in the endcaps. The difference between data and MC is used as a scale factor, which is calculated as the ratio of integral of the multi-jet MC and data normalized distributions above the cut on the number of tracklets. The scale factor on the number of tracklets in the jet cone is 0.80 ± 0.01 in the barrel and 0.75 ± 0.01 in the endcaps. This indicates that the number of tracklets created by the hadronic shower is about 20% larger in the MC compared to the data in the barrel, and 25% larger in the endcaps.

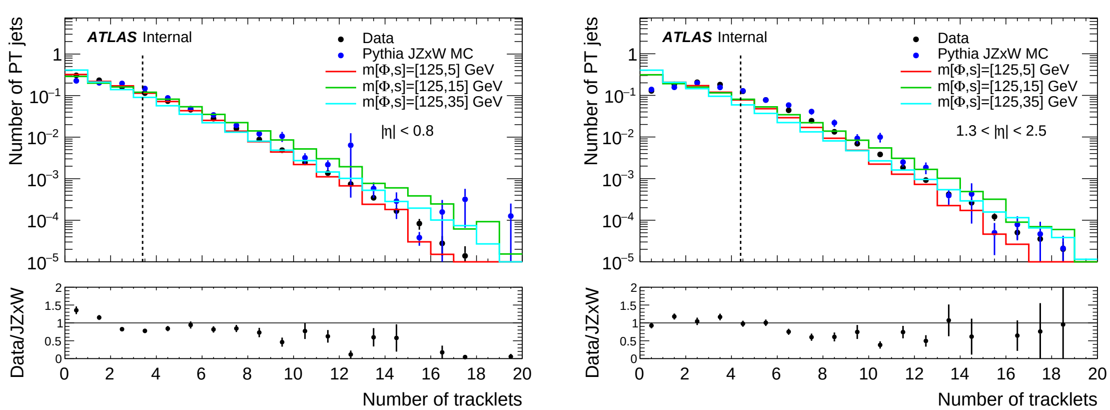

(a) (b)

Figure 7.10: Tracklets distribution within $\Delta R = 0.4$ of the punch-through jet axis for barrel 7.10a and endcaps 7.10b. The black dots show 2015-2018 data while the blue dots are the multi-jet MC simulations. The vertical lines show the cut applied at vertex reconstruction level. The solid lines are some signal benchmark samples.

To better model real detector vertex reconstruction in MC, vertices in the MC are reconstructed by removing a fraction of the tracklets according to the tracklet scale factors in the barrel and endcaps. That is to say, 20% of tracklets are removed randomly for barrel and 25% of tracklets are removed for endcaps before applying reconstruction algorithms. The vertex reconstruction efficiency using a reduced number of tracklets are compared with the original efficiency. The MC efficiencies are shown in Figure 7.11 for the 35 GeV scalar sample. The number of reconstructed vertices in the nominal and reduced number of tracklet samples are given in Tables 7.6, 7.7, 7.8 and 7.9. The ratio is used as a scale factor for the vertex reconstruction in MC. For simplicity, the final scale factor is taken to be the average over all benchmark samples. The averaged scale factor in the barrel is 0.73 and the averaged scale factor in the endcaps is 0.91.

Another way to correct the tracklet mismodelling is to reweight the MC tracklet distribution bin-by-bin to match the data distribution. The weight applied to the tracklet is then applied to each vertex according to the number of the associated tracklets. The scale factor can then be calculated by comparing the vertex reconstruction efficiencies derived from weighted vertices and unweighted vertices. The difference between the two methods are taken to be a systematic uncertainty on the scale factor, which is 11% in the barrel and 13% in the endcaps.

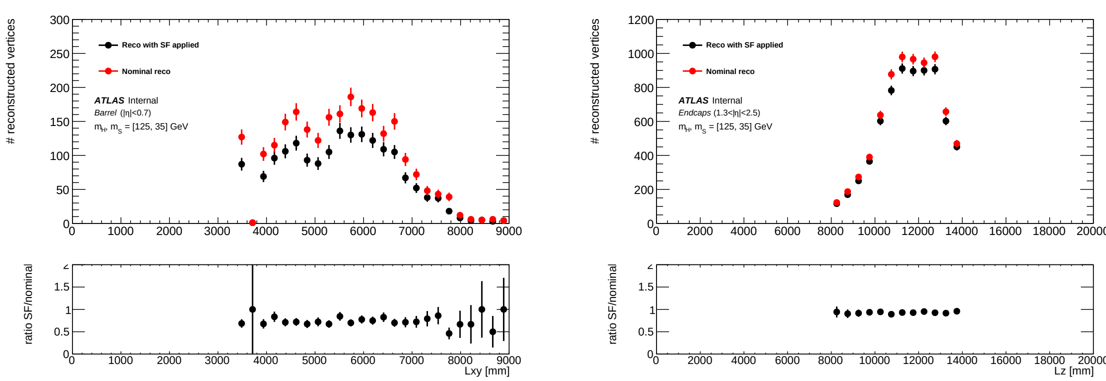

(a) (b)

Figure 7.11: Vertex reconstruction efficiency after the tracklet scale factor is applied compared with efficiency after nominal reconstruction for 35 GeV scalar samples mediated by the SM Higgs. Left is in barrel and right is in endcaps.

Sample $m_{\mathrm{H}} = 125$ GeV	nVertices reconstructed with nominal reco	nVertices reconstructed after SF is applied during reco	vertex SF
$m_{\mathrm{S}} = 5$ GeV	266	193	0.726
$m_{\mathrm{S}} = 15$ GeV	2723	2047	0.752
$m_{\mathrm{S}} = 35$ GeV	2414	1765	0.731
$m_{\mathrm{S}} = 55$ GeV	720	531	0.738

Table 7.6: Summary of effect of vertex scale factor on vertex reconstruction efficiency in the barrel, for samples mediated by the SM Higgs.

Sample $m_{\mathrm{H}} = 125$ GeV	nVertices reconstructed with nominal reco	nVertices reconstructed after SF is applied during reco	Vertex SF
$m_{\mathrm{S}} = 5$ GeV	2072	1864	0.900
$m_{\mathrm{S}} = 15$ GeV	11887	11031	0.928
$m_{\mathrm{S}} = 35$ GeV	15224	14118	0.927
$m_{\mathrm{S}} = 55$ GeV	5982	5525	0.924

Table 7.7: Summary of effect of vertex scale factor on vertex reconstruction efficiency in the endcaps, for samples mediated by the SM Higgs.

m_H [GeV]	m_S[GeV]	nVertices reconstructed with nominal reco	nVertices reconstructed after SF is applied during reco	Vertex SF
60	5	1921	1403	0.730
	15	1417	1085	0.766
200	50	3481	2617	0.752
400	100	6536	4463	0.683
600	50	17060	12943	0.759
	150	11254	7736	0.687
1000	50	10414	7144	0.686
	275	15598	11546	0.740
	475	3077	2071	0.673

Table 7.8: Summary of effect of vertex scale factor on vertex reconstruction efficiency in the barrel for non-SM Higgs samples.

m_H [GeV]	m_S[GeV]	nVertices reconstructed with nominal reco	nVertices reconstructed after SF is applied during reco	Vertex SF
60	5	20440	18162	0.889
	15	12104	11085	0.916
200	50	17408	16218	0.932
400	100	20690	18002	0.870
600	50	29403	27765	0.944
	150	25759	22333	0.867
1000	50	12996	12001	0.923
	275	26006	24194	0.930
	475	28078	23805	0.848

Table 7.9: Summary of effect of vertex scale factor on vertex reconstruction efficiency in the endcaps for non-SM Higgs samples.

CHAPTER 8

Search for Two Displaced Vertices in the Muon Spectrometer

8.1 Analysis Overview

This analysis targets on a BSM process in which a pair of long-lived particles are produced that each decay hadronically. This analysis focuses on the case where each long-lived particle (LLP) decays into the MS. A benchmark process for this event is the production of LLPs produced via the Higgs portal as described in Section 2.2. This analysis is sensitive to other models in which a pair of LLP particles are produced as well.

SM particles originating from the pp collisions, except for neutrinos, will more or less leave some activities in the ID or calorimeters. It is rare to have a displaced vertex of more than tens of cm from SM processes. The requirement of a second displaced vertex will further suppress the SM background from collision, since the probability to have two displaced background vertices is extremely small. While the SM background is negligible, there are other sources of background that give rise to MS vertices that appear displaced. These backgrounds include:

- Because there are large fluctuations associated with the hadronic shower process, remnants of the shower can escape the calorimeter and enter the MS. These are referred to as punch-through jets. Due to mis-measurement on jets that contain only neutral hadrons or jets that go into crack region, punch-through jets may not be reconstructed and therefore make the MS vertex look displaced.
- Beam-halo muons can create showers in the MS and fake an isolated MS vertex.
- Cosmic ray muons can create showers in the MS and fake an isolated MS vertex.
- Bursts of noise in detectors and electronics can create large numbers of hits in the MDT and trigger chambers. The combination of these hits can be reconstructed as an isolated MS vertex.

These sources of background are not well modeled by any MC simulations. We therefore use a data-driven method to estimate the background in the two MS vertex search.

8.2 Analysis Cutflow

Signal-like events are selected using an analysis cutflow summarized in Table 8.1. In the pre-selection stage, events are required to pass the HLT_j30_muvtx_noiso trigger and also pass the standard ATLAS event cleaning selections. These criteria are used to remove problematic regions of the detector or incomplete events. When a detector problem occurs in the liquid argon system, the tile calorimeter system or the SCT inner detector system, or an event has missing information, error flags will be added to the event so that the problematic events can be removed by the event cleaning selection. Each event is required to have one primary vertex with at least two good tracks, which reduces the non-collision background occurring during a bunch crossing.

Events with two or more MS vertices are selected. Each MS vertex must pass the selection criteria described in Section 7.2. The MS vertex section are slightly different depending on whether the vertex is in the barrel or endcap region. If a second muon RoI is present in the event, the second vertex must be matched to the second cluster since a long-lived particle will very rarely leave a cluster of muon RoIs in a different angular region to an MS vertex. In addition to the basic selection, an data event must pass the good runs list, in which each part of the detector must be fully operational and output uncorrupted data.

8.3 Background Estimation

The number of background events is estimated by a data-driven method which uses data from both main stream (collision data of interest for physics studies) and zero-bias stream (data collected by the zero-bias trigger). The estimation is based on the assumption that there is no correlation between finding one MS vertex and finding another. In this case, the number of background is estimated by the product of the number of triggered data events with one MS vertex and the probability to have another MS vertex. The formula used is shown as follow:

$$N_{\mathrm{2Vx}} = N^{\mathrm{1cl}} \cdot P^{\mathrm{Vx}}_{\mathrm{noMStrig}} + N^{\mathrm{2cl}}_{\mathrm{1UMBcl}} \cdot P^{\mathrm{Vx}}_{\mathrm{Bcl}} + N^{\mathrm{2cl}}_{\mathrm{1UMEcl}} \cdot P^{\mathrm{Vx}}_{\mathrm{Ecl}}. \tag{8.1}$$

This equation can be separated into two parts with different number of trigger clusters. The first term has only one cluster. The N^{1cl} in the first term is the number of main stream data events that fire the Muon RoI Cluster trigger and have only one trigger cluster matched to a MS vertex. $P^{\mathrm{Vx}}_{\mathrm{noMStrig}}$ measures the probability that a vertex randomly occurs from any process without firing the trigger. This term is

Level	Cut	Value
Preselection	Trigger	HLT_j30_muvtx_noiso
	Event cleaning	Standard ATLAS event cleaning
	Primary vertex	At least one (standard ATLAS selection)
	MS Vertex multiplicity	At least 2
MS Vertex selection	MDT hits	$300 < \text{nHits} < 3000$
	RPC hits	$\text{nHits} > 250$ ($\lvert\eta_{vx}\rvert < 1.0$)
	TGC hits	$\text{nHits} > 250$ ($1.0 < \lvert\eta_{vx}\rvert < 2.5$)
	Min. vertex tracklets	3 (4) in barrel (endcaps)
	MS Overlap region veto	$0.8 < \lvert\eta_{vx}\rvert < 1.3$
	HCal crack veto	$0.7 < \lvert\eta_{vx}\rvert < 1.3$
	Trigger matching	$\Delta R(\text{vx, muon RoI Cluster}) < 0.4$
		If a second trigger cluster is present, vertex matches cluster
Jet selection for vertex isolation	p_{T}	> 30 GeV
	$\log_{10}(E_{\mathrm{HAD}}/E_{\mathrm{EM}})$	< 0.5
	JVT	JVT > 0.59 if jet $p_{\mathrm{T}} < 60$ GeV
Event selection	Vertex Isolation	See Table 7.1

Table 8.1: Description of the selection criteria used for the 2 MSVtx channel. Details of vertex selection are described in Chapter 7.

calculated by data collected by zero-bias trigger HLT_zb_noalg_L1ZB. The number of events with one vertex N[1Vx] in the zero-bias data are counted. $P^{\mathrm{Vx}}_{\mathrm{noMStrig}}$ is given by N[1Vx] divided by the total number of zero-bias events N[Events]. As a result, the first term represents the number of background events with two vertices, of which one vertex is matched to the cluster and the other is not.

The second and third terms represent the cases where there are two trigger clusters. In the formula, barrel and endcaps are treated separately. This is because triggers in the barrel and endcaps have different requirements on the number of RoIs, and the vertex reconstruction strategies are different as mentioned in the previous sections. The $N^{\mathrm{2cl}}_{\mathrm{1UMBcl}}$ or $N^{\mathrm{2cl}}_{\mathrm{1UMEcl}}$ is the number of data events that have one vertex and two clusters with one cluster matched to the vertex and the other unmatched. The letter "B" stands for the case where the unmatched cluster is in the barrel and "E" stands for the case in the endcaps.

If a second vertex occurs, it must be matched to the unmatched cluster. The probability that a MS vertex has a matching trigger clusters is given by $P^{\mathrm{Vx}}_{\mathrm{Bcl}}$ or $P^{\mathrm{Vx}}_{\mathrm{Ecl}}$, depending on the detector region. Its value is given by the ratio of the number of events in main stream data with one matched vertex/cluster pair (N[1BCluVx] or N[1ECluVx]) divided by the number of events with one cluster (N[1BClu] or N[1EClu]). The combination of second and third terms in Equation 8.1 gives the number of background events with two vertices and each of the vertices are matched to a cluster.

Since the Muon RoI Cluster trigger and MS vertex reconstruction are based on cone algorithms of either muon RoIs or tracklets, if the decay positions of two LLPs are close to each other, there is a chance that the two clusters or two vertices created by the two LLPs can not be resolved. To eliminate such events, in the analysis, any events with two vertices are required to have a $\Delta R = 1.0$ separation. This is a sufficient separation for any cone algorithm with $\Delta R = 0.4$, like the one used in the trigger cluster reconstruction.

The value of each parameter used for Equation 8.1 is listed in Table 8.2. The zero-bias data is collected at a fixed rate of 7 Hz. This means that the zero-bias data could severely undersample the runs with high instantaneous luminosity, which thus leads to a different pileup profile than the main stream data. To match the pileup distribution of the main stream data, each of the zero-bias events is assigned a weight that is defined as the ratio of the number of events occurring in the main stream data at a given pileup μ, divided by the number of events occurring in the zero-bias data

Stream	Quantity	Value
ZeroBias	N[Events]	115707416 ± 10757
	N[1Vx]	53 ± 7
	$\rightarrow P^{\text{Vx}}_{\text{noMStrig}}$	$(4.6 \pm 0.6) \times 10^{-7}$
Main	$N^{1\text{cl}}$	674775 ± 821
	$N^{2\text{cl}}_{1\text{UMBcl}}$	$3^{+2.43}_{-1.17}$
	$N^{2\text{cl}}_{1\text{UMEcl}}$	$0^{+1.35}_{-0.00}$
	N[1BClu]	38509130 ± 6206
	N[1BCluVx]	124648 ± 353
	$\rightarrow P^{\text{Vx}}_{\text{Bcl}}$	$(3.24 \pm 0.009) \times 10^{-3}$
	N[1EClu]	15598939 ± 3950
	N[1ECluVx]	550127 ± 742
	$\rightarrow P^{\text{Vx}}_{\text{Ecl}}$	$(3.53 \pm 0.005) \times 10^{-2}$

Table 8.2: Numbers of events in the 13 TeV dataset passing the Muon RoI Cluster trigger and the zero-bias trigger HLT_zb_noalg_L1ZB. Vertices are required to pass the isolation criteria described in Section 7.2, These values are necessary to calculate the background prediction. The notation is explained in the text. Uncertainties are statistical only. The probabilities needed to compute the background from events containing MS vertices from non-signal processes are also reported. $P^{\text{Vx}}_{\text{Bcl}}$ and $P^{\text{Vx}}_{\text{Ecl}}$ are the probabilities of finding one MS isolated vertex in events passing the Muon RoI Cluster trigger that have a single cluster that is matched to a vertex in the barrel or endcaps, respectively. The probability of finding an MS isolated vertex not matched to a cluster of muon RoIs is given by $P^{\text{Vx}}_{\text{noMStrig}}$.

at the same pileup μ. After reweighting the zero-bias events, the value of $P^{\text{Vx}}_{\text{noMStrig}}$ is re-calculated to be $(4.61 \pm 0.63) \times 10^{-7}$.

The final background estimation and the number of observed events in 2015-2018 data are summarized in Table 8.3. Figure 8.1 shows the number of background per average pileup per integrated luminosity at each data-taking year. The distribution is almost flat, which indicates that the background is not only affected by the luminosity, but also the pileup.

Expected background events	Observed events
0.32 ± 0.05	0

Table 8.3: Background estimation and observed events in 2015-2018 data.

The background estimation method is validated using two background dominated

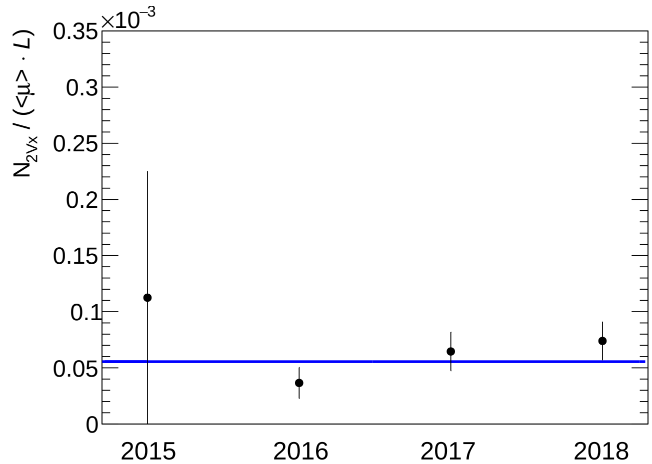

Figure 8.1: Number of background events per average pileup per integrated luminosity at each data-taking year from 2015 to 2018.

validation regions based on the inverted vertex-track isolation criteria and the vertex-jet isolation criteria shown in Table 8.4.

One validation region is defined by selecting events with two non-isolated vertex-cluster pairs. The number of events with two vertex-cluster pairs is observed to be 1 using the full Run 2 data. The term with two muon RoI clusters, $N^{2\text{cl}}_{1\text{UMBcl}} \cdot P^{\text{Vx}}_{\text{Bcl}} + N^{2\text{cl}}_{1\text{UMEcl}} \cdot P^{\text{Vx}}_{\text{Ecl}}$, predicts $1.561^{+0.289}_{-0.241}$ events in the same region. The prediction is statistically consistent with the observation.

The term with one muon RoI cluster, $N^{1\text{cl}} \cdot P^{\text{Vx}}_{\text{noMStrig}}$, is validated by applying the inverted isolation criteria to $N^{1\text{cl}}$ but not to $P^{\text{Vx}}_{\text{noMStrig}}$, which gives the number of events in another validation region with one non-isolated vertex-cluster pair and one isolated vertex. The reason to have a second validation region is that $P^{\text{Vx}}_{\text{noMStrig}}$ will underestimate the probability of there being a non-isolated vertex. Because the average activity in the detector is significantly lower in the zero-bias data than in the main stream data. In this validation region, $N^{1\text{cl}} \cdot P^{\text{Vx}}_{\text{noMStrig}}$ predicts 0.99 ± 0.20 events and 0 events are observed.

8.4 Lifetime Extrapolation

8.4.1 Extrapolation Procedure

The fully simulated signal benchmark MC samples are only generated for a single proper lifetime. However, the analysis is sensitive to a wide range of proper lifetimes.

Requirement	Barrel	Endcap
MDT hits	$300 \leq n_{\mathrm{MDT}} < 3000$	$300 \leq n_{\mathrm{MDT}} < 3000$
RPC/TGC hits	$n_{\mathrm{RPC}} \geq 250$	$n_{\mathrm{TGC}} \geq 250$
>5 GeV track isolation	$\boldsymbol{\Delta R < 0.2}$	$\boldsymbol{\Delta R < 0.3}$
Track $\lvert\Sigma\vec{p_{\mathrm{T}}}\rvert$ in 0.2 cone	< 10 GeV	< 10 GeV
>30 GeV jet isolation	$\boldsymbol{\Delta R < 0.2}$	$\boldsymbol{\Delta R < 0.3}$

Table 8.4: Inverted isolation criteria (marked in bold) applied to MS vertices.

Instead of generating MC events at many lifetimes, the results from the simulated MC sample are extrapolated to larger and smaller lifetimes. A toy MC using only the long-lived particle 4-momenta, together with trigger efficiency and vertex reconstruction efficiency are used to perform this extrapolation to estimate the expected number of signal events for each sample, for a range of proper lifetimes between 0 m and 300 m (this is the range between which a useful limit can be set).

In order to determine if a criterion is passed based on an efficiency (*e.g.* will a LLP decay leave a good reconstructed vertex), a random number between 0 and 1 is generated. If the random number is less than the efficiency, the event passes the selection.

Two important efficiencies we need to consider here are trigger efficiency and vertex reconstruction efficiency. To implement the random probability strategy mentioned above, we need a trigger efficiency to determine if a LLP decay will fire the muon RoI cluster trigger and a vertex reconstruction efficiency to determine if a LLP decay will leave a good reconstructed vertex. In principle, the trigger and vertex efficiencies at a certain detector position have a dependence on the kinematic distribution of an LLP. The kinematic distribution of an LLP is different in the detector fiducial region for samples with different mean proper lifetimes. In order to make the efficiencies independent of lifetime, the trigger and vertex reconstruction efficiencies are parameterized as functions of LLP decay position and the LLP boost β, one of the LLP kinematic variables.

Since the trigger efficiency in the two MS vertex topology depends on both of the LLPs, it will be a function of four arguments (two LLP positions and two LLP boosts). Directly parameterizing the efficiency in this way will lead to large statistical uncertainties in each bin. Instead one uses a parameterization for a single MS vertex that has only two variables. Assuming that the two LLPs fire trigger independently, the trigger efficiency for the two MS vertex topology $\epsilon_{\text{trigger, 2LLP}}$ can be estimated by

$$\epsilon_{\text{trigger, 2LLP}}(\text{LLP}_1, \text{LLP}_2) = 1 - (1 - P_{\text{trigger, 1LLP}}(\text{LLP}_1))(1 - P_{\text{trigger, 1LLP}}(\text{LLP}_2)), \tag{8.2}$$

where $P_{\text{trigger, 1LLP}}$ is the trigger probability derived in the one MS LLP region. It is calculated by dividing the number of triggered events in a region with only one MS LLP that is separated to the other LLP, by the total number of events in the same region. An example of $P_{\text{trigger, 1LLP}}$ is shown in Figure 8.2.

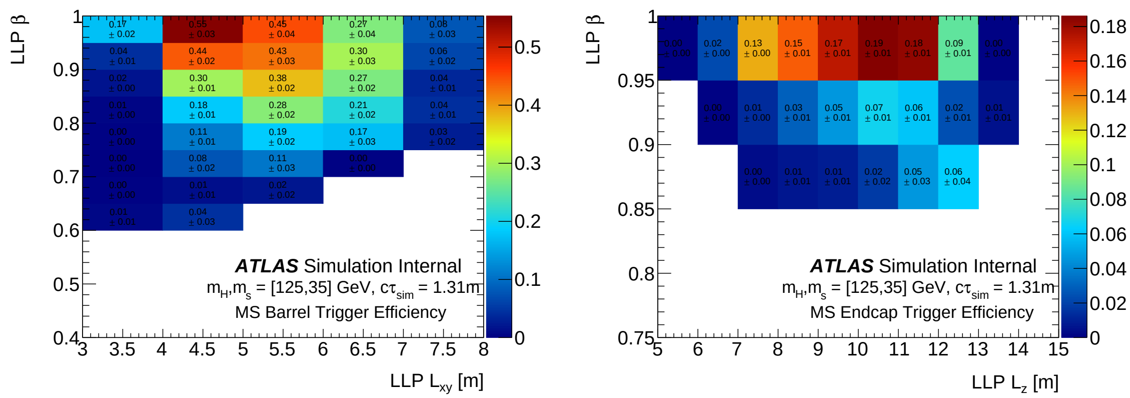

(a) (b)

Figure 8.2: (a) MS Barrel trigger probability in the one-LLP region. (b) MS Endcap trigger probability in the one-LLP region.

$P_{\text{trigger, 1LLP}}$ is not the same as the trigger efficiency defined in Section 5.4.2 due to the additional requirement on separation of the two LLPs. Because the calculation of the $P_{\text{trigger, 1LLP}}$ efficiency required that the two LLPs be well separated by a ΔR cut or that one of the LLPs decayed outside the detector. This was done in order to minimize contamination from one LLP decay on the decay of interest. If ΔR is 0, the estimated MS 2-vertex trigger efficiency $\epsilon_{\text{trigger, 2LLP}}$ will be highly overestimated. As ΔR increases, $P_{\text{trigger, 1LLP}}$ decreases and the statistical uncertainty increases. The ΔR cut for $P_{\text{trigger, 1LLP}}$ is relaxed to the point where the difference between the estimated trigger efficiency $\epsilon_{\text{trigger, 2LLP}}$ and the trigger efficiency directly calculated from the signal MC sample is within 1σ uncertainty. Signal MC samples with different parameters generally have different detector signature, so the ΔR cut needs to be tuned for each sample. The choice of ΔR values and corresponding results are listed in Table 8.5.

m_H	m_s	Lifetime [m]	ΔR	$f_{trig}^{toy\ estimation}$	$f_{trig}^{fullsim}$	% diff. (median)
125	5	0.127	3.0	$0.00183^{+0.00018}_{-0.00017}$	0.00173 ± 0.00011	5.8%
125	15	0.580	3.0	$0.00590^{+0.00022}_{-0.00021}$	0.00505 ± 0.00014	16.8%
125	35	1.31	3.0	$0.00386^{+0.00018}_{-0.00017}$	0.00385 ± 0.00008	0.3%
125	55	5.32	2.0	$0.00143^{+0.00013}_{-0.00013}$	0.00141 ± 0.00006	1.4%
60	5	0.217	3.0	$0.000492^{+0.000034}_{-0.000039}$	0.000501 ± 0.000032	1.8%
60	15	0.661	3.0	$0.000482^{+0.000049}_{-0.000050}$	0.000585 ± 0.000048	17.6%
200	50	1.255	3.0	$0.00713^{+0.00034}_{-0.00035}$	0.00666 ± 0.00020	7.1%
400	100	1.608	3.0	$0.01704^{+0.00048}_{-0.00048}$	0.01481 ± 0.00030	15.1%
600	50	0.590	3.0	$0.02487^{+0.00038}_{-0.00040}$	0.02634 ± 0.00039	5.6%
600	150	1.840	3.0	$0.02318^{+0.00042}_{-0.00042}$	0.02176 ± 0.00029	6.5%
600	275	4.288	2.0	$0.00533^{+0.00014}_{-0.00015}$	0.00480 ± 0.00008	11.0%
1000	50	0.406	3.0	$0.03181^{+0.00031}_{-0.00032}$	0.02935 ± 0.00034	8.4%
1000	275	2.399	3.0	$0.02952^{+0.00048}_{-0.00048}$	0.02762 ± 0.00033	6.9%
1000	475	6.039	2.0	$0.00552^{+0.00016}_{-0.00016}$	0.00529 ± 0.00008	4.3%

Table 8.5: Fraction of toy events passing trigger selection criteria with separated LLPs ($\Delta R > 1$) that both decay in the MS and the fraction of signal events passing trigger selection in the fully simulated signal samples.

For the two vertex reconstruction efficiency we use the efficiency calculated in the one MS vertex region $\epsilon_{\text{vtx reco, 1vtx}}$. The vertex reconstruction efficiency for the two MS vertex topology $\epsilon_{\text{vtx reco, 2vtx}}$ is

$$\epsilon_{\text{vtx reco, 2vtx}}(\text{LLP}_1, \text{LLP}_2) = \epsilon_{\text{vtx reco, 1vtx}}(\text{LLP}_1) \cdot \epsilon_{\text{vtx reco, 1vtx}}(\text{LLP}_2). \qquad (8.3)$$

An example of $\epsilon_{\text{vtx reco, 1vtx}}$ is shown in Figure 8.3.

The steps used in making the lifetime extrapolation for the two MS vertex topology are listed here:

1. Starting with $c\tau = 0.01$ m, generate a random decay position for each of the two LLPs, sampled from an exponential distribution, $f(t) = \exp -t/\beta\gamma c\tau$.

2. Calculate the physical decay position in the detector for each of the particles, using their stored 4-momenta.

3. Determine if the resulting decay position topology satisfies the two vertex fiducial region. There are three categories to check:

   (a) Barrel MS - Barrel MS: Two particles decaying with $|\eta| < 0.7, 3\,\text{m} < R < 8\,\text{m}$.

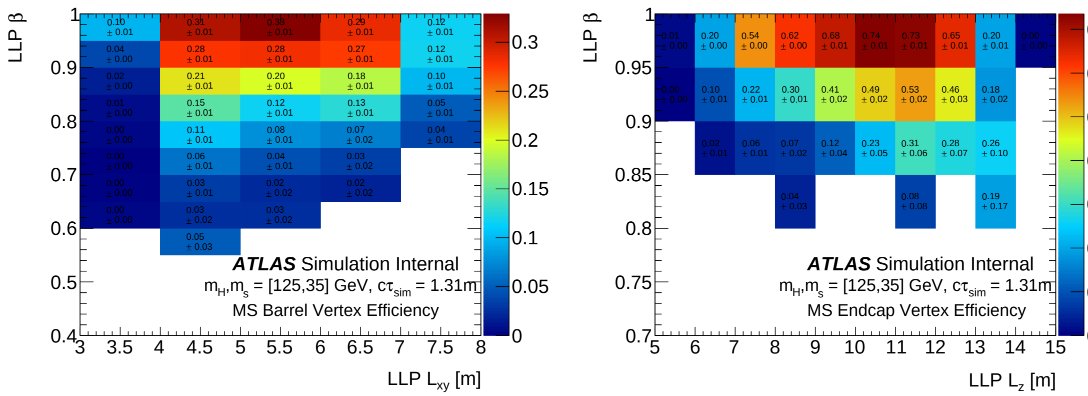

(a) (b)

Figure 8.3: (a) MS Barrel vertex reconstruction efficiency in the one-vertex region. (b) MS Endcap vertex reconstruction efficiency in the one-vertex region.

(b) Barrel MS - Endcap MS: One particle decaying with $|\eta| < 0.7, 3\,\text{m} < R < 8\,\text{m}$ and the other with $1.3 < |\eta| < 2.5, 5\,\text{m} < |z| < 15\,\text{m}$, $R < 10\,\text{m}$.

(c) Endcap MS - Endcap MS: Two particles decaying with $1.3 < |\eta| < 2.5, 5\,\text{m} < |z| < 15\,\text{m}$, $R < 10\,\text{m}$.

4. Each topology has a distinct set of trigger and vertex reconstruction efficiencies and thus a slightly different procedure. They are outlined individually below:

(a) Barrel MS - Barrel MS (BB)

i. Determine if the barrel decay with Δt, which is defined as how late the decay products of an LLP arrives at the last RPC trigger plane as compared to a particle traveling at speed of light c, is in time with respect to the level-1 barrel trigger response in data [151]. The decay is considered "in time" if its randomly generated probability is less than the efficiency for the RPC response at the particle's Δt.

ii. If the event is in time, determine if it will pass the RoI cluster trigger by using the estimated efficiency for the trigger $\epsilon_{\text{trigger, 2LLP}}$, where both of the LLPs decay in MS barrel.

iii. If the event passes the trigger, the MS vertex reconstruction efficiency $\epsilon_{\text{vtx reco, 2vtx}}$ is considered for barrel MS decays in triggered barrel MS - barrel MS events. Each LLP is considered individually. If both decays pass the vertex reconstruction efficiency, the event is counted as a good two vertex event.

(b) Barrel MS - Endcap MS (BE)

i. Determine if the endcap decay is in time ($\Delta t < 25\,\text{ns}$). If it is not, then see if the barrel decay is in time based on the efficiency for the RPC response.

ii. If the event is in time, determine if it will pass the RoI cluster trigger by using the estimated efficiency for the trigger $\epsilon_{\text{trigger, 2LLP}}$, where one of the LLPs decays in MS barrel and the other decays in MS endcap.

iii. If the event passes the trigger, the MS vertex reconstruction efficiency $\epsilon_{\text{vtx reco, 2vtx}}$ is considered for barrel MS decays in triggered barrel MS - endcap MS events and for endcap MS decays in triggered barrel MS - endcap MS events. If both decays "reconstruct" vertices, the event is counted as a good two vertex event.

(c) Endcap MS - Endcap MS (EE)

i. Determine if the endcap decay with smaller Δt (not necessarily the decay with larger β - this also depends on how far the particle travels before decaying) is in time ($\Delta t < 25\,\text{ns}$).

ii. If the event is in time, determine if it will pass the RoI cluster trigger by using the estimated efficiency for the trigger $\epsilon_{\text{trigger, 2LLP}}$, where both of the LLPs decay in MS endcap.

iii. If the event passes the trigger, the MS vertex reconstruction efficiency $\epsilon_{\text{vtx reco, 2vtx}}$ is considered for endcap MS decays in triggered endcap MS - endcap MS events. Each LLP is considered individually. If both decays "reconstruct" vertices, the event is counted as a good two vertex event.

(d) Steps 1 through 4 are repeated starting from $c\tau = 0.01$ m to $c\tau = 300.0$ m with an increment changed with the proper lifetime. The step size is changed because the scale on which the expected signal changes between $c\tau$ values becomes larger.

(e) The final result is the number of expected signal events as a function of proper lifetime for each topology (BB, BE and EE). These numbers are summed together and rescaled by (production cross-section)x(integrated luminosity)/(number of toy events) to obtain the number of expected signal events in 139 fb^{-1} of data.

As a final step, the estimated global signal efficiency is compared with the global signal efficiency directly calculated from the benchmark signal MC sample.The global efficiency includes both trigger and vertex reconstruction efficiencies. The difference is considered as a systematic uncertainty on the extrapolation method. In Table 8.6, we listed the comparison results for samples with different mass points.

m_H	m_s	Lifetime [m]	$\epsilon_{global}^{toy\ estimation}$	$\epsilon_{global}^{fullsim}$	% diff. (median)
125	5	0.127	$0.000178^{+0.000021}_{-0.000019}$	0.000155 ± 0.000040	14.8%
125	15	0.580	$0.000742^{+0.000033}_{-0.000034}$	0.000697 ± 0.000058	6.5%
125	35	1.31	$0.000552^{+0.000034}_{-0.000032}$	0.000509 ± 0.000029	8.4%
125	55	5.32	$0.000072^{+0.000009}_{-0.000008}$	0.000065 ± 0.000014	10.8%
60	5	0.217	$0.000035^{+0.000002}_{-0.000003}$	0.000038 ± 0.000008	7.9%
60	15	0.661	$0.000054^{+0.000005}_{-0.000006}$	0.000059 ± 0.000015	8.5%
200	50	1.255	$0.00112^{+0.00008}_{-0.00007}$	0.00101 ± 0.00008	10.9%
400	100	1.608	$0.00219^{+0.00012}_{-0.00012}$	0.00203 ± 0.00012	7.9%
600	50	0.590	$0.00268^{+0.00014}_{-0.00014}$	0.00295 ± 0.00013	9.2%
600	150	1.840	$0.00209^{+0.00011}_{-0.00010}$	0.00231 ± 0.00010	9.5%
600	275	4.288	$0.000177^{+0.000010}_{-0.000012}$	0.000226 ± 0.000017	21.7%
1000	50	0.406	$0.00220^{+0.00009}_{-0.00009}$	0.00216 ± 0.00009	1.9%
1000	275	2.399	$0.00130^{+0.00010}_{-0.00009}$	0.00139 ± 0.00008	6.5%
1000	475	6.039	$0.000097^{+0.000010}_{-0.000010}$	0.000139 ± 0.000013	30.2%

Table 8.6: Estimated global signal efficiency from extrapolation method and global signal efficiency from benchmark signal sample.

8.4.2 Parametrisation of the Expected Signal Events

The result of the toy MC is an expected number of signal events at each simulated proper lifetime, which is subject to statistical uncertainties from the number of toy events. To present a smooth limit, the expected event histograms are all fit with a Novosibirsk function [152]. The Novosibirsk function is defined as follows:

$$f(x; x_0, \sigma, \tau) = \exp\left[-\frac{1}{2}\left\{\frac{\ln^2\left(1+\Lambda\tau(x-x_0)\right)}{2\tau^2}+\tau^2\right\}\right], \tag{8.4}$$

$$\text{where} \qquad \Lambda = \frac{\sinh\left(\tau\sqrt{\ln 4}\right)}{\sigma\tau\sqrt{\ln 4}}. \tag{8.5}$$

An example of a fit in the $[m_H, m_s] = [125, 35]$ GeV, two MS vertex event topology case is shown in Figure 8.4.

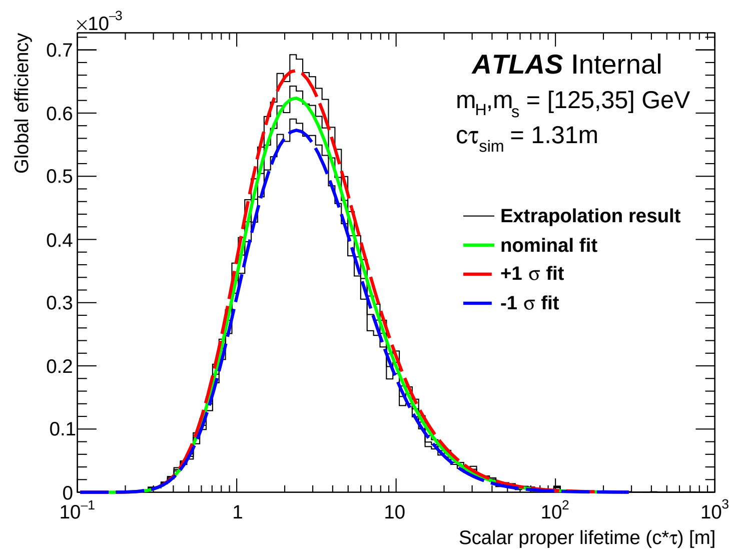

Figure 8.4: Signal efficiencies obtained from the extrapolation procedure outlined in Section 8.4 and fits using a Novosibirsk function. The three lines represent the nominal signal efficiency and the variation accounting for all statistical errors.

8.4.3 Extrapolation Results

Figures 8.5, 8.6 and 8.7 show the results of the lifetime extrapolation for samples with different masses and proper lifetimes.

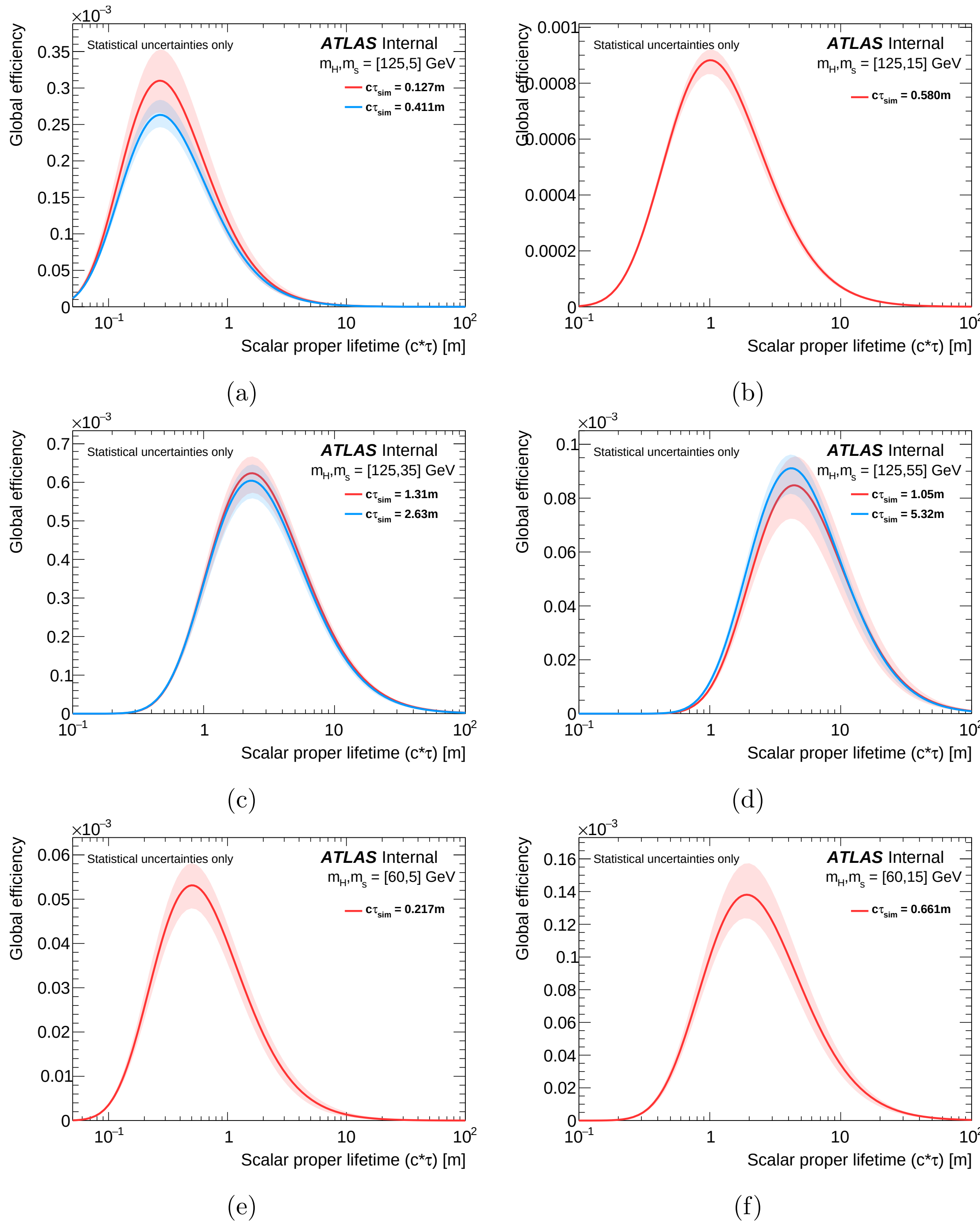

Figure 8.5: Extrapolated global signal efficiencies for different samples. The plots show agreement between extrapolations performed with official MC samples with different lifetimes for $H \to ss$ decays. Uncertainties are the result of statistical uncertainties of the efficiencies input into the extrapolation.

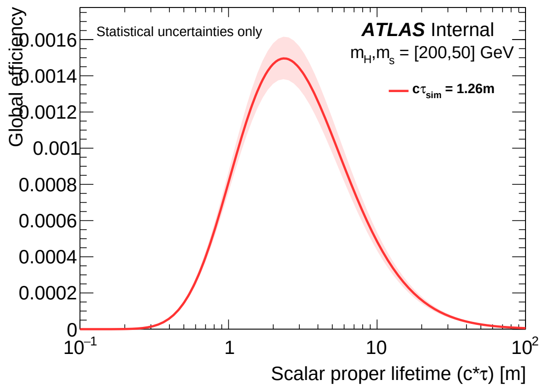

(a)

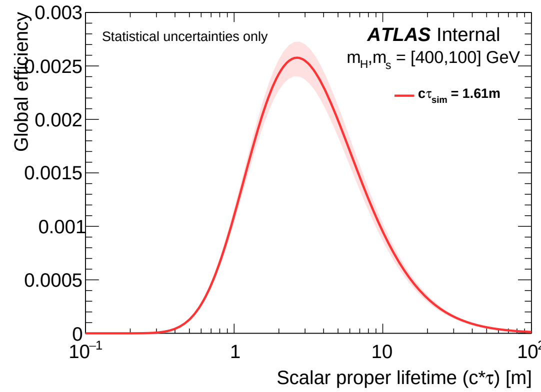

(b)

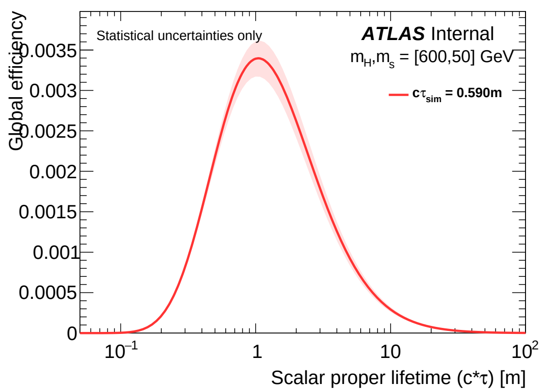

(c)

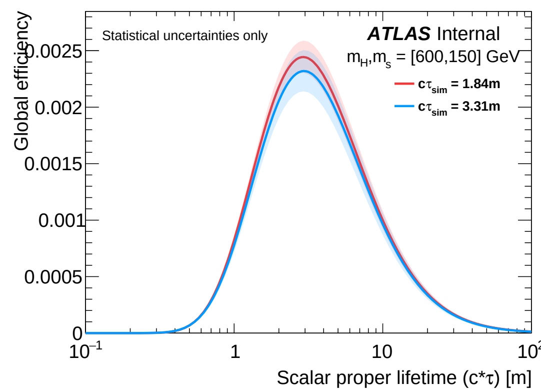

(d)

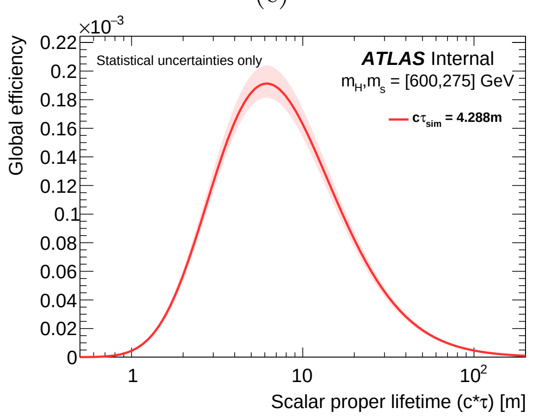

(e)

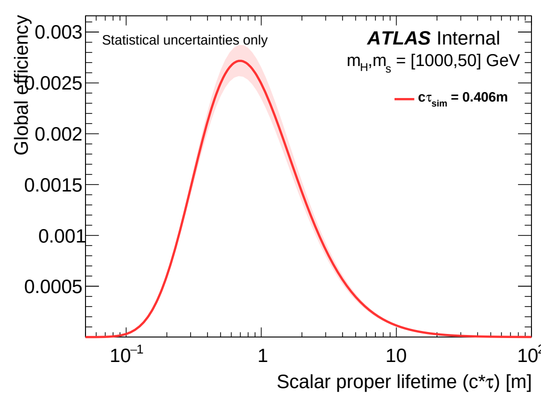

(f)

Figure 8.6: Extrapolated global signal efficiencies for different samples. The plots show agreement between extrapolations performed with official MC samples with different lifetimes for $H \rightarrow ss$ decays. Uncertainties are the result of statistical uncertainties of the efficiencies input into the extrapolation.

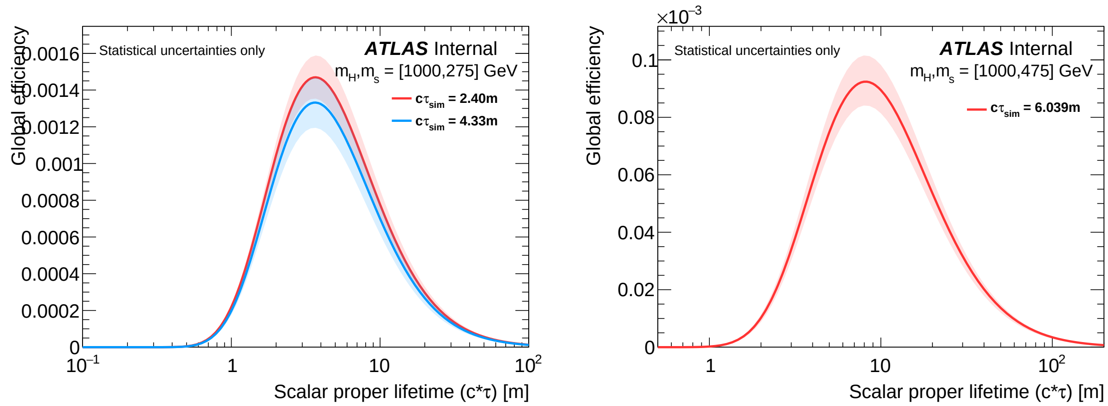

(a) (b)

Figure 8.7: Extrapolated global signal efficiencies for different samples. The plots show agreement between extrapolations performed with official MC samples with different lifetimes for $H \to ss$ decays. Uncertainties are the result of statistical uncertainties of the efficiencies input into the extrapolation.

8.5 Systematic Uncertainties

This section summaries the systematic uncertainties associated with the analysis.

8.5.1 Systematic Uncertainties from Mismodelling in Signal MC

In Section 5.4.1, mismodellilng factors on L1 Muon RoI are derived for barrel and endcaps respectively. They are 1.24 ± 0.01 in barrel and 1.20 ± 0.01 in endcaps. To be conservative and not over-estimate the final limits, these factors are used as systematic uncertainties on the trigger efficiencies, which means 24% uncertainty is applied to the barrel trigger efficiency and 20% uncertainty is applied on the endcap trigger efficiency.

Section 7.5 discusses the tracklet mismodelling. The scale factor derived for the barrel vertex reconstruction efficiency is 0.75 and the scale factor for the endcap vertex reconstruction efficiency is 0.91. The systematic uncertainties associated with these scale factors are 11% in the barrel and 13% in the endcaps.

8.5.2 Systematic Uncertainties from Pileup

The distribution of the number of primary vertices in MC simulation does not exactly match that in data. This is due to the imperfect modelling of the number of primary vertices in the minimum bias simulation. After reweighting the MC events, which is called the pileup reweighting (PRW) procedure, a systematic error remains. This can be seen in Figure 8.8 that shows the barrel vertex reconstruction efficiency for the $[m_H,\ m_S] = [125,\ 55]$ GeV sample, with and without the pileup systematic uncertainties applied.

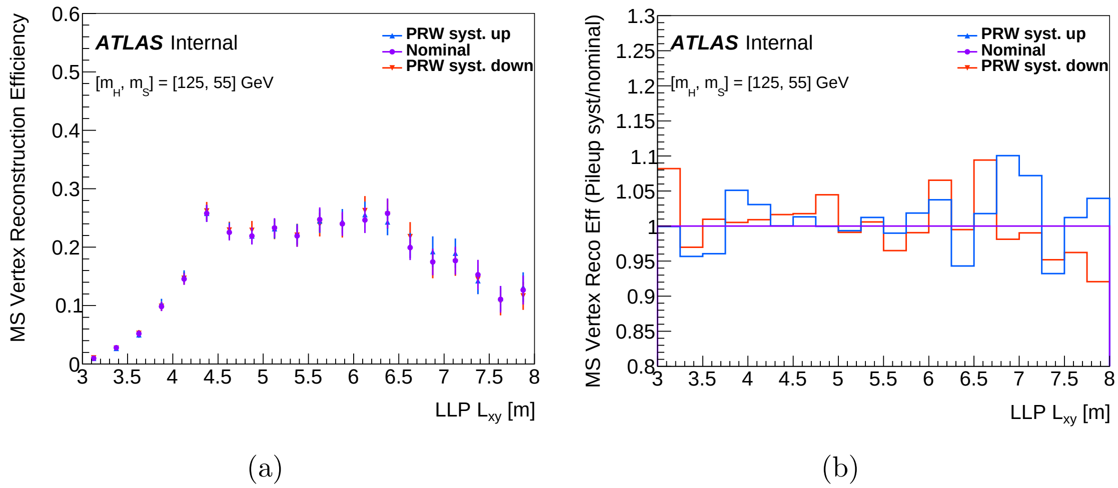

Figure 8.8: The effect of pileup systematic uncertainties on the MS vertex reconstruction efficiency in the barrel, for the Hidden Sector $[m_H,\ m_S] = [125,\ 55]$ GeV sample.

In Figure 8.8b, it is clear that any effect the pileup systematic uncertainty has on the vertex reconstruction efficiency does not depend on the LLP decay position. Thus, the final contribution to the vertex reconstruction efficiency is determined with a rebinned efficiency, just as with the data–MC scale factor systematic uncertainties addressed in the previous subsection. For this benchmark sample, pileup systematics contribute $+1.1$, -0% to the overall vertex reconstruction systematic uncertainty.

8.5.3 Systematic Uncertainties from PDF

The parton distribution function (PDF) used to generate signal MC events is NNPDF3.1 (NNPDF31_lo_as_0130). The central value "best estimate" of the PDF is used to generate events, but this is formed from the 100 different PDF fits extracted from input data. In order to determine the uncertainty resulting from this ensemble of fits, each MC sample is reweighed to mimic each of the 100 PDF fits. For each final-state efficiency (*e.g.* Muon RoI Cluster trigger or MS Vertex reconstruction), the ratio of the efficiency for the PDF fit weighted events to the central value PDF events is determined. An example of this is shown in Figure 8.9a.

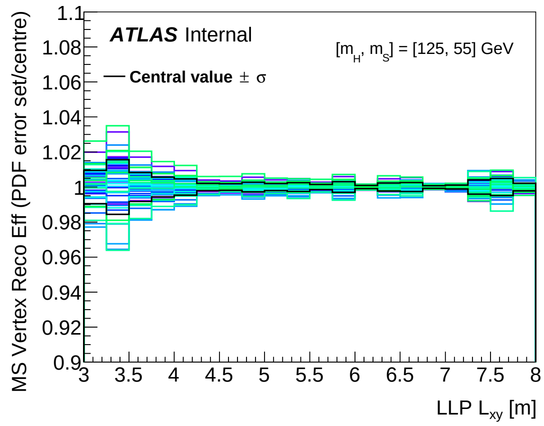

(a) (b)

Figure 8.9: The effect of parton distribution function uncertainties on the MS vertex reconstruction efficiency in the barrel, for the Hidden Sector $[m_H,\ m_S] = [125,\ 55]$ GeV sample.

The sample standard deviation of the ensemble is calculated for each L_{xy} bin, and the systematic uncertainty is the central value $\pm$ the standard deviation. The central value $\pm 1\sigma$ is shown as black line in Figure 8.9a and the data points in Figure 8.9b. The per-bin variations are approximately uniform, and thus the net systematic uncertainty on the reconstruction efficiency is determined by re-binning the efficiency into a single bin, as was done for the pileup and data–MC scale factor systematic uncertainties. In this case, the systematic uncertainty on barrel MS vertex reconstruction due to PDF uncertainties is ± 0.004, or $\pm 0.4\%$.

8.5.4 Summary of Systematic Uncertainties

The contributions to systematic uncertainties from each of the components are listed as follows:

- Systematic uncertainty from luminosity measurement in Run 2 is 1.7%.
- Mismodelling of muon RoIs assigns a 24% systematic uncertainty to the barrel trigger efficiency and a 20% systematic uncertainty to the endcap trigger efficiency.
- Mismodelling of MS vertex reconstruction is characterized by scale factors on the vertex reconstruction efficiencies, 0.75 for the barrel and 0.91 for the endcaps.

The systematic uncertainties associated to the barrel and endcap scale factors are 11% and 13%, respectively.

- The systematic uncertainties from lifetime extrapolation using the toy MC method are listed in Section 8.4. They range from 1.9% to 30% depending on masses.
- The pileup and PDF systematic uncertainties are summarized in Tables 8.7-8.14. In the end, the pileup and PDF uncertainties that are applied are the average uncertainties across all the signal samples. For the pileup uncertainty on the vertex reconstruction, it is ±0.51% in the barrel and ±0.24% in the endcaps. For the pileup uncertainty on the RoI Cluster trigger, it is ±0.47% in the barrel and ±0.58% in the endcaps. For the PDF uncertainty on the vertex reconstruction, it is ±0.19% in the barrel and ±0.19% in the endcaps. For the PDF uncertainty on the RoI Cluster trigger, it is ±0.23% in the barrel and ±0.22% in the endcaps.

Table 8.7: Summary of systematic uncertainties on the Muon RoI Cluster trigger in the barrel for the Higgs boson benchmark samples with $m_H = 125$ GeV.

m_s	Pileup	PDF	Total
5	+0, -2.0%	±0.1%	**+0.1, -2.0%**
15	+0.6, -1.3%	~ 0	**+0.6, -1.3%**
35	+0.2, -0.3%	±0.1%	**+0.2, -0.3%**
55	+0.8, -1.6%	±0.4%	**+0.9, -1.6%**

Table 8.8: Summary of systematic uncertainties on the Muon RoI Cluster trigger in the barrel for the scalar boson benchmark samples with $m_H \neq 125$ GeV.

m_H	m_s	Pileup	PDF	Total
60	5	+0, -1.6%	±0.4%	**+0.4, -1.6%**
60	15	+0, -1.5%	±0.4%	**+0.4, -1.6%**
200	50	+0.6, -0%	±0.07%	**+0.6, -0.07%**
400	100	+0, -0.4%	±0.02%	**+0.02, -0.4%**
600	50	+0.1, -0.3%	±0.02%	**+0.1, -0.3%**
600	150	+0.3, -0%	±0.04%	**+0.3, -0.04%**
600	275	+0, -0.3%	±0.6%	**+0.6, -0.7%**
1000	50	+0, -0.09%	±0.02%	**+0.02, -0.09%**
1000	275	+0, -0.1%	±0.07%	**+0.07, -0.1%**
1000	475	+0.5, -0.4%	±1.0%	±**1.1**%

Table 8.9: Summary of systematic uncertainties on the Muon RoI Cluster trigger in the endcaps for the Higgs boson benchmark samples with $m_H = 125$ GeV.

m_s	Pileup	PDF	Total
5	+0.1, -1.0%	±0.1%	**+0.1, -1.0%**
15	+2.4, -2.1%	~ 0	**+2.4, -2.1%**
35	+0.7, -0.2%	±0.2%	**+0.7, -0.3%**
55	+0.4, -0.03%	±0.4%	**+0.6, -0.4%**

Table 8.10: Summary of systematic uncertainties on the Muon RoI Cluster trigger in the endcaps for the scalar boson benchmark samples with $m_H \neq 125$ GeV.

m_H	m_s	Pileup	PDF	Total
60	5	+0, -0.9%	±0.1%	**+0.1, -0.9%**
60	15	+2.6, -1.3%	±0.3%	**+2.6, -1.3%**
200	50	+1.2, -0%	±0.2%	**+1.2, -0.2%**
400	100	+0.5, -0%	±0.2%	**+0.5, -0.2%**
600	50	+0.4, -0.2%	±0.1%	**+0.4, -0.2%**
600	150	+0.3, -0%	±0.2%	**+0.4, -0.2%**
600	275	+0.5, -0%	±0.2%	**+0.5, -0.2%**
1000	50	+0, -0.2%	±0.08%	**+0.08, -0.2%**
1000	275	+0, -0.1%	±0.3%	±**0.3**%
1000	475	+0, -1.0%	±0.7%	**+0.7, -1.2%**

Table 8.11: Summary of MS vertex systematic uncertainty in the barrel for the Higgs boson benchmark samples with $m_H = 125$ GeV.

m_s	Pileup	PDF	Total
5	+0, -0.3%	$\pm$0.1%	**+0.1, -0.3%**
15	+0.7, -1.7%	~ 0	**+0.7, -1.7%**
35	+0, -0.2%	$\pm$0.1%	**+0.1, -0.2%**
55	+1.1, -0%	$\pm$0.4%	**+1.2, -0.4%**

Table 8.12: Summary of MS vertex systematic uncertainty in the barrel for the scalar boson benchmark samples with $m_H \neq 125$ GeV.

m_H	m_s	Pileup	PDF	Total
60	5	+1.4, -1.1%	$\pm$0.2%	**+1.4, -1.1%**
60	15	+1.7, -0.2%	$\pm$0.2%	**+1.7, -0.3%**
200	50	+0.5, -0.5%	$\pm$0.09%	$\pm$**0.5**%
400	100	+0.3, -0.4%	$\pm$0.02%	**+0.3, -0.4%**
600	50	+0.3, -0.1%	$\pm$0.03%	**+0.3, -0.1%**
600	150	+0.1, -0%	$\pm$0.02%	**+0.1, -0.02%**
600	275	+0, -0.6%	$\pm$0.5%	**+0.5, -0.8%**
1000	50	+0.8, -0%	$\pm$0.07%	**+0.8, -0.07%**
1000	275	+0.05, -0.3%	$\pm$0.05%	**+0.07, -0.3%**
1000	475	+0.3, -1.5%	$\pm$0.5%	**+0.6, -1.6%**

Table 8.13: Summary of MS vertex systematic uncertainty in the endcaps for the Higgs boson benchmark samples with $m_H = 125$ GeV.

m_s	Pileup	PDF	Total
5	+0, -0.9%	$\pm$0.05%	**+0.05, -0.9%**
15	+0.2, -0.4%	~ 0	**+0.2, -0.4%**
35	+0, -0.08%	$\pm$0.1%	$\pm$**0.1**%
55	+0, -0.5%	$\pm$0.2%	**+0.2, -0.5%**

Table 8.14: Summary of MS vertex systematic uncertainty in the endcaps for the scalar boson benchmark samples with $m_H \neq 125$ GeV.

m_H	m_s	Pileup	PDF	Total
60	5	+0.3, -0.1%	±0.05%	**+0.3, -0.1%**
60	15	+0.06, -0.6%	±0.1%	**+0.1, -0.6%**
200	50	+0.1, -0.2%	±0.1%	**+0.1, -0.2%**
400	100	+0, -0.5%	±0.1%	**+0.1, -0.5%**
600	50	+0.3, -0.1%	±0.08%	**+0.3, -0.1%**
600	150	+0.3, -0%	±0.1%	**+0.3, -0.1%**
600	275	+0.3, -0%	±0.4%	**+0.5, -0.4%**
1000	50	+0.01, -0.6%	±0.2%	**+0.2, -0.6%**
1000	275	+0.2, -0.5%	±0.1%	**+0.2, -0.5%**
1000	475	+0, -0.4%	±1.1%	**+1.1, -1.2%**

CHAPTER 9

Statistical Interpretation of Results

9.1 Overview of the Statistical Method

9.1.1 Signal Discovery

In Chapter 8, the final data yield from the event selection is counted and the number of background events in the signal region is estimated. To tell how likely signal excess exists in the observed data, the final yield is compared to the total background using a statistical method called the hypothesis test. One hypothesis test consists of a null hypothesis H_0 and an alternative hypothesis H_1. In the context of signal discovery, H_0 assumes that only background processes exist, which is often referred to as the background-only hypothesis. H_1 assumes that signal process exists besides of the background, which is called the signal-plus-background hypothesis.

To quantify the level of agreement between the observed data and the given hypothesis, a test statistic needs to be constructed. The test statistic can be the number of events in a certain kinematic region or a likelihood ratio of signal and background events. According to the statistical model built for the analysis, the distribution of test statistic using assumption H_0 can be generated from either pseudo-experiments or from asymptotic functions [153]. The value of the test statistic can be used to find the probability of finding data of equal or greater incompatibility with the predictions under the assumption of H_0. This probability is called p-value. The smaller the $p-$value is, the larger is the incompatibility between data and the hypothesis. Typically a hypothesis is regarded as excluded if the p-value is below a certain threshold α, where $1-\alpha$ is referred to as confidence level (CL).

In this analysis, the statistical model is described by a likelihood that is the product of a Poisson probability and constraint terms π_j:

$$L(\mu, \boldsymbol{\theta}) = \frac{(\mu+b)^n}{n!} e^{-(\mu+b)} \prod_{\theta_j \in \boldsymbol{\theta}} \pi_j(\theta_j). \tag{9.1}$$

μ is our parameter of interest (POI), the expected signal yield. The value of $\mu = 0$ corresponds to the background-only hypothesis and $\mu > 0$ corresponds to the signal-plus-background hypothesis. The other values in the likelihood are b, the number of expected background events and n, the number of observed events in the signal region. Thus $\mu + b$ gives the expectation value of n.

The set of $\boldsymbol{\theta} = \{\theta_j\}$ is a set of nuisance parameters that describes the statistical and systematic uncertainties for signal and background. The value of a nuisance parameter is usually constrained by independent auxiliary measurements or by physical assumptions. Since all the nuisance parameters in our analysis are uncertainties, their distributions π_j have to be modeled from assumptions. We assume that the uncertainties associated with the number of signal and background events follow a Gaussian distribution. Hence the π_j are set to be Gaussian functions.

To test the agreement between the data and the hypothesized value of μ, we consider the profile likelihood ratio described in [153]:

$$\tilde{\lambda}(\mu) = \begin{cases} \frac{L(\mu,\boldsymbol{\theta}'(\mu))}{L(\hat{\mu},\hat{\boldsymbol{\theta}})} & \hat{\mu} \geq 0 \\ \frac{L(\mu,\boldsymbol{\theta}'(\mu))}{L(0,\boldsymbol{\theta}'(0))} & \hat{\mu} < 0 \end{cases} \tag{9.2}$$

In the numerator, $\boldsymbol{\theta}'$ is the value of $\boldsymbol{\theta}$ that maximizes L for any specified μ. In the denominator, $\hat{\mu}$ and $\hat{\boldsymbol{\theta}}$ are the maximum-likelihood estimators, i.e., $L(\hat{\mu}, \hat{\boldsymbol{\theta}}) \geq L(\mu, \boldsymbol{\theta})$ for any μ and $\boldsymbol{\theta}$. When $\hat{\mu} < 0$, the denominator is set to $L(0, \boldsymbol{\theta}'(0))$, because $\tilde{\lambda}(\mu)$ corresponds to a physics model with $\mu \geq 0$. If the data are found to have negative $\hat{\mu}$, the best level of agreement between data and any physical value of μ occurs for $\mu = 0$. For $\hat{\mu} \geq 0$, the value of $\tilde{\lambda}$ is within a range between 0 and 1. A value of $\tilde{\lambda}$ close to 1 implies good agreement between the data and the hypothesized μ.

The test statistic used by this analysis called the profile log-likelihood ratio, which is constructed from the profile likelihood ratio. It is defined in Equation 9.3.

$$q_0 = -2\ln\tilde{\lambda}(0) = \begin{cases} -2\ln\frac{L(0,\boldsymbol{\theta}')}{L(\hat{\mu},\hat{\boldsymbol{\theta}})} & \hat{\mu} \geq 0 \\ 0 & \hat{\mu} < 0 \end{cases}. \tag{9.3}$$

For the purpose of signal discovery, we test $\mu = 0$ against a hypothesis that assumes the existence of signal. With this definition, the background-only hypothesis is only tested for $\hat{\mu} \geq 0$. When the observed event yield is found to be above the expected background, $\hat{\mu}$ will increase. This in turn gives rise to a larger value of q_0, corresponding to a larger incompatibility between data and the $\mu = 0$ hypothesis. The case $\hat{\mu} < 0$ is irrelevant to signal finding but rather likely points to possible fluctuations in the data. As a result, it is not considered.

The p-value under the background-only hypothesis, p_0, is computed by

$$p_0 = \int_{q_{0,\mathrm{obs}}}^{\infty} f(q_0|0)dq_0, \tag{9.4}$$

where $f(q_0|0)$ is the probability density function of q_0 under the $\mu = 0$ hypothesis and $q_{0,\mathrm{obs}}$ is the value of q_0 at the observed n. In particle physics, the p-value is usually converted to a significance value, Z, given by

$$Z = \Phi^{-1}(1 - p_0), \tag{9.5}$$

where Φ^{-1} is the inverse of the cumulative distribution of the standard Gaussian and p_0 is equal to the upper tail probability. The value of the significance is interpreted as the level of deviation of a Gaussian variable from its mean value. Equivalently the value of Z is interpreted as Z standard deviations (σ) above the mean value. To claim a discovery, one necessary but arbitrary condition is $Z > 5$ (or $p_0 < 2.87 \times 10^{-7}$). This means that the probability of fluctuation of background events upwards to the observed number of events is very low, 2.87×10^{-7}. If Z is less than five but larger than three ($p_0 = 1.3 \times 10^{-3}$), we say there is an evidence of signal.

9.1.2 The CL$_s$ Method

In our analysis, we observed zero events which means no signal excess. In this case, we can proceed to set an exclusion limit on the cross section of the long-lived particle production. In the limit-setting procedure, the signal-plus-background hypothesis is treated as H_0 and tested against the background-only hypothesis, H_1. For models with $\mu \geq 0$, we consider a test statistic $\tilde{q}_\mu$ defined as

$$\tilde{q}_\mu = \begin{cases} -2\ln\tilde{\lambda}(\mu) & \mu \geq \hat{\mu} \\ 0 & \mu < \hat{\mu} \end{cases} = \begin{cases} -2\ln\frac{L(\mu,\boldsymbol{\theta}'(\mu))}{L(\hat{\mu},\hat{\boldsymbol{\theta}})} & \mu \geq \hat{\mu} \geq 0 \\ -2\ln\frac{L(\mu,\boldsymbol{\theta}'(\mu))}{L(0,\boldsymbol{\theta}'(0))} & \hat{\mu} < 0 \\ 0 & \mu < \hat{\mu}. \end{cases} \tag{9.6}$$

Note $\tilde{q}_\mu$ is set to 0 for $\mu < \hat{\mu}$, because the data with $\hat{\mu} > \mu$ is not considered to be less compatible with the hypothesis that predicts the presence of μ. Therefore $\mu < \hat{\mu}$ does not go into the rejection region. Generally speaking, a larger $\tilde{q}_\mu$ corresponds to a worse agreement between data and the μ prediction.

To quantify the agreement, we calculate the p-value under the signal-plus-background hypothesis. That is,

$$p_\mu = \int_{\tilde{q}_{\mu,\mathrm{obs}}}^{\infty} f(\tilde{q}_\mu|\mu)\, d\tilde{q}_\mu, \tag{9.7}$$

where $f(\tilde{q}_\mu|\mu)$ is the probability density function under the hypothesis μ. If p_μ is below a certain threshold α, then the signal-plus-background hypothesis is regarded as excluded at a confidence level of $1 - \alpha$. For limit setting, α is often set to 0.05. Thus the confidence interval $[0, \mu_{\rm up}]$ at 95% CL can be constructed. The upper limit $\mu_{\rm up}$, which is called the 95% CL upper limit, can be extracted from the point where $p_\mu = 0.05$. This hypothesis test method is called the "CL_{s+b}" method, where CL_{s+b} is another notation for the p-value p_μ, i.e., $\mathrm{CL}_{s+b} = p_\mu$.

One potential problem of the CL_{s+b} method is that signal models with low sensitivity could be excluded with a probability of α (0.05). This happens when $\mu \ll b$, which corresponds to the case where the signal-plus-background hypothesis is almost indistinguishable from the background-only hypothesis. When the number of observed events n has a sufficient downward fluctuation, the μ hypothesis could be excluded and result in an anomalously low upper limit. This exclusion has a one in 20 chance of occurring when α is equal to 0.05. In the case of models with low sensitivity, since if the outcomes predicted with or without μ are identical, it is not reasonable to reject the μ hypothesis and give preference to the background-only one.

In order not to reject a model with low sensitivity, the "CL_s" method [154] is used. This is method typically adopted for limit setting on ATLAS.

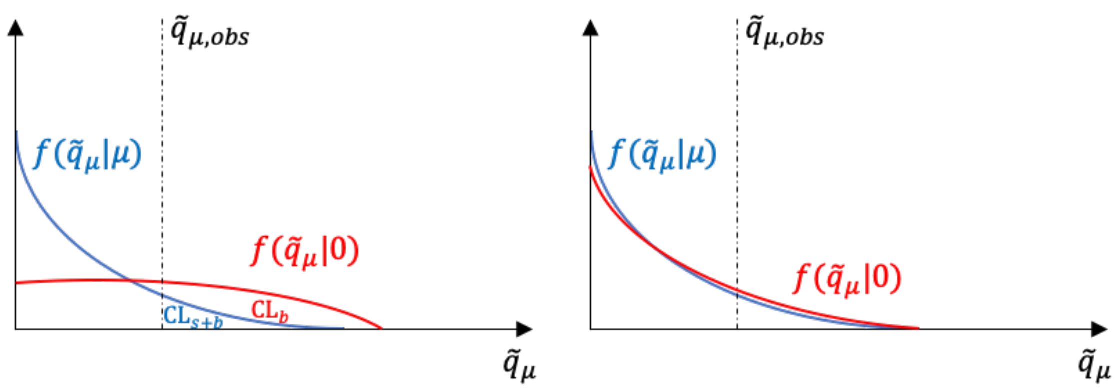

(a) (b)

Figure 9.1: Sketch of the probability density functions of $\tilde{q}_\mu$ under the signal-plus-background hypothesis (blue) and the background-only hypothesis (red), respectively. Figure 9.1a shows the case where the signal model has sufficient sensitivity. Figure 9.1b shows the case where the sensitivity to μ is low.

The CL_s is defined as a ratio of CL_{s+b} and CL_b. That is,

$$\mathrm{CL}_s = \frac{\mathrm{CL}_{s+b}}{\mathrm{CL}_b}, \quad \text{with } \mathrm{CL}_b = \int_{\tilde{q}_{\mu,\rm obs}}^{\infty} f(\tilde{q}_\mu|0)\, d\tilde{q}_\mu. \tag{9.8}$$

The signal-plus-background hypothesis is regarded as excluded if

$$\mathrm{CL}_s < \alpha. \tag{9.9}$$

Figure 9.1 shows a sketch of the probability density functions of $\tilde{q}_\mu$ under the signal-plus-background hypothesis and the background-only hypothesis, respectively. CL_{s+b} and CL_b correspond to the upper tail areas of the two functions and are labeled in Figure 9.1a. If a search has low sufficient sensitivity to μ, the two distributions $f(\tilde{q}_\mu|\mu)$ and $f(\tilde{q}_\mu|0)$ are overlap with each other. In this case, CL_b gives a small value that is close to CL_{s+b} and results in a CL_s that is larger than α. In this way, the CL_s method prevents from excluding signal models with low sensitivity.

Since CL_b is less than or equal to one, to exclude a μ hypothesis, CL_{s+b} derived in the CL_s method has to be smaller than that in the CL_{s+b} method given the same α. This means that the upper limit μ_{up} derived from the CL_s method is generally larger than that derived from the CL_{s+b} method. The CL_s method produces more conservative limits than the CL_{s+b}.

9.2 Results

9.2.1 Expected and Observed Limits

The CL_s method is used to derive the upper limits on the signal yield μ. The upper limit μ_{up} is given by

$$\mu_{\mathrm{up}} = (\sigma \times B)_{\mathrm{up}} \cdot \mathcal{L} \cdot \epsilon_{\mathrm{global}}, \tag{9.10}$$

This expression can be used to set an upper limit on $\sigma \times B$, which is denoted as $(\sigma \times B)_{\mathrm{up}}$. In the formula, σ is the production cross section of particle H, B represents the branching fraction for $H \to ss$ assuming 100% branching fraction of s into fermion pairs, $\mathcal{L}$ is the ATLAS Run 2 luminosity and $\epsilon_{\mathrm{global}}$ is the global signal efficiency. The global signal efficiency takes into account all effects including detector acceptance, trigger efficiency, vertex reconstruction efficiency, and event selection efficiency.

For scalar boson benchmark samples with $m_H \neq 125$ GeV, upper limits are set on $\sigma \times B$. For scalar boson benchmark samples with $m_H = 125$ GeV, upper limits are set on $(\sigma/\sigma_{\mathrm{SM}}) \times B$, where $\sigma_{\mathrm{SM}} = 48.61$ pb [155, 156, 157] is the SM Higgs boson gluon-gluon fusion production cross section at QCD next-to-next-to-next-to-leading order ($\mathrm{N^3LO}$) using Higgs boson mass of 125.09 GeV.

Upper limits are generated using pyhf-v0.6.2 [158, 159] package. The inputs consist of the number of background events, the background uncertainty and all the signal uncertainties. Signal uncertainties are combined and constrained by one Gaussian function. Pseudo-experiments, often referred to as toy ensembles or toys, are used to sample the distributions of the profile log-likelihood ratio $\tilde{q}_\mu$ under signal-plus-background and background-only hypotheses, respectively.

Figure 9.2 shows the expected and observed limits for a boson with $m_H = 125$ GeV decaying to long-lived particles that decay in the muon spectrometer. Figures 9.3 – 9.7 show the expected and observed limits for a boson with $m_H \neq 125$ GeV to displaced hadronic jets. The dashed line represents the expected upper limit, which assumes that n is equal to b (0.32). The 1σ and 2σ uncertainties for expected limit is given by the green and yellow bands, respectively. The solid line represents the observed limit. A summary of the observed limits is shown in Figure 9.8.

The different behaviors of limits of these bench mark samples are correlated with the kinematics of the LLP decay. Different kinematics correspond to different detector acceptance, trigger efficiencies and vertex reconstruction efficiencies, which affect the final limit. In these limit plots, one finds that the lifetime of the minimum limit increases with the scalar mass. This is due to the fact that scalars with lower boost need more time to reach the MS.

Table 9.1 summarizes the lifetime ranges excluded by the analysis for branching fractions $B(H(125) \to ss) = 10\%$ and 1% for the scalar boson with $m_H = 125$ GeV decaying into two long-lived scalars. Table 9.2 shows the lifetime exclusion range at 95% for samples with $m_H \neq 125$ GeV assuming $\sigma \times B = 1$ pb.

$H(125) \to ss$	Excluded $c\tau_s$ range for s [m]	
m_s [GeV]	B = 1%	B = 10%
5	0.08–1.6	0.04–5.9
15	0.18–10.8	0.11–32.9
35	0.48–22.6	0.30–71.3
55	2.1–7.8	0.84–40.2

Table 9.1: Ranges of mean proper lifetime excluded at 95% CL for scalar boson benchmark models with $m_H = 125$ GeV, assuming production cross-sections equal to 10% or 1% of the SM Higgs boson production cross section.

$(m_H,\, m_s)$ [GeV]	Excluded $c\tau_s$ range [m] $\sigma \times B = 1$ pb	$(m_H,\, m_s)$ [GeV]	Excluded $c\tau_s$ range [m] $\sigma \times B = 1$ pb
(60, 5)	0.20–1.50	(600, 150)	0.42–68.6
(60, 15)	0.51–11.0	(600, 275)	1.55–40.4
(200, 50)	0.33–47.8	(1000, 50)	0.10–19.7
(400, 100)	0.36–65.8	(1000, 275)	0.65–18.7
(600, 50)	0.13–30.2	(1000, 475)	2.73–33.1

Table 9.2: Ranges of mean proper lifetime excluded at 95% CL for scalar boson benchmark models with $m_H \neq 125$ GeV, assuming production cross-sections equal to 1 pb.

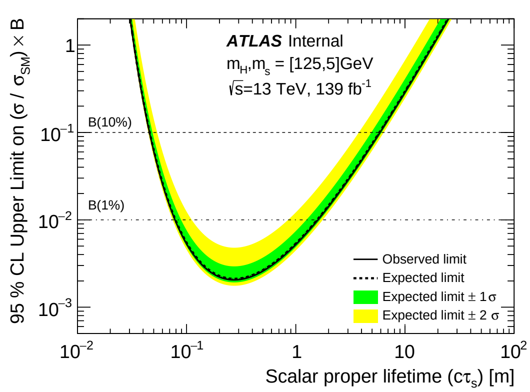

(a)

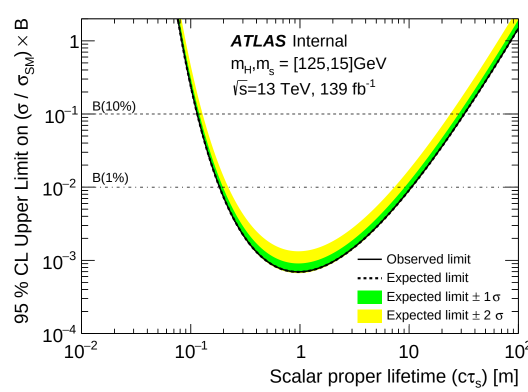

(b)

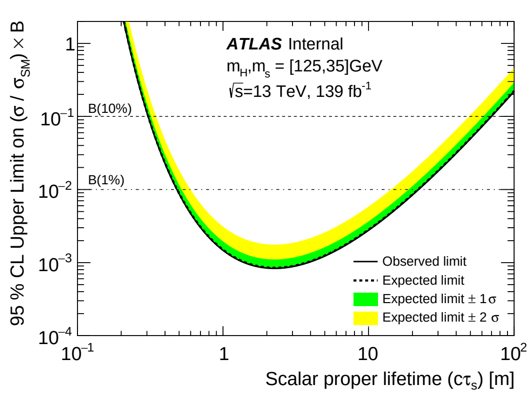

(c)

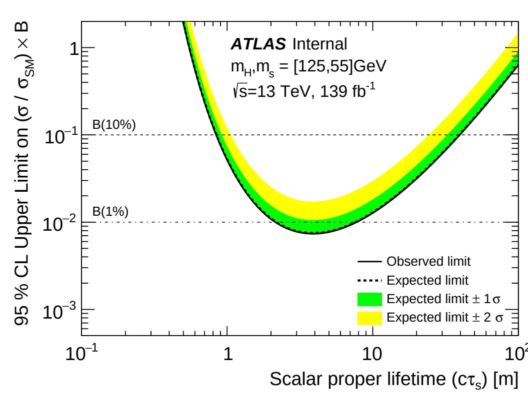

(d)

Figure 9.2: Expected and observed limits for the 125 GeV boson benchmark samples.

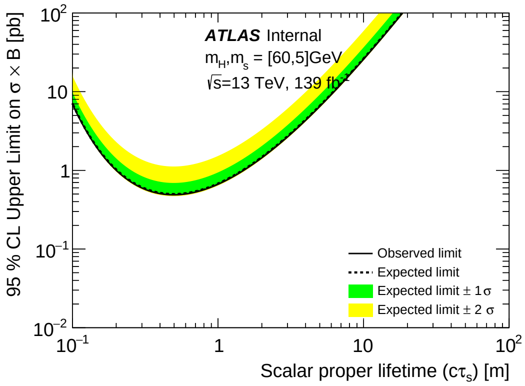

(a)

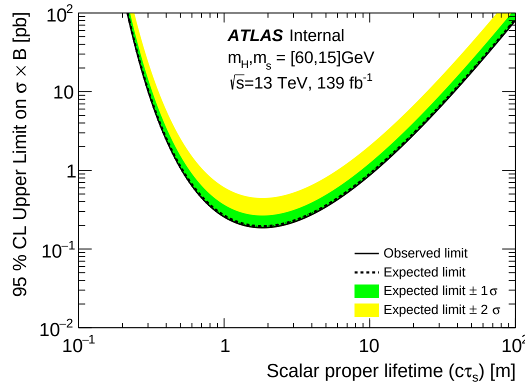

(b)

Figure 9.3: Expected and observed limits for 60 GeV non-SM Higgs boson scalar benchmark samples.

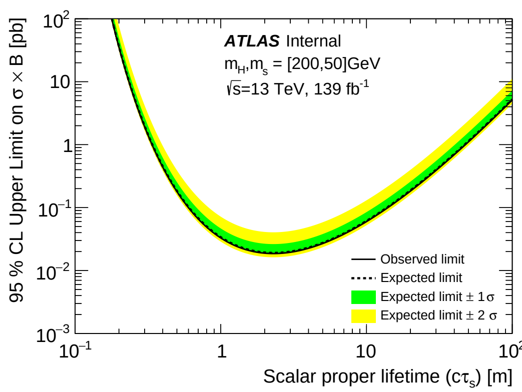

(a)

Figure 9.4: Expected and observed limits for 200 GeV non-SM Higgs boson scalar benchmark samples.

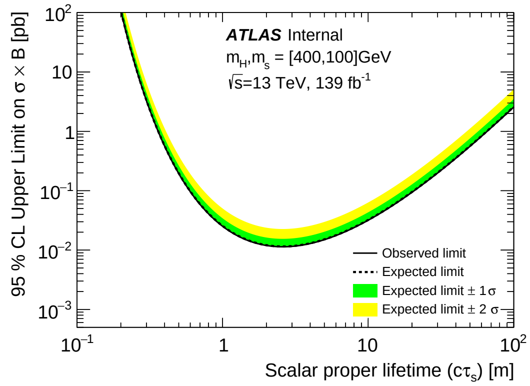

(a)

Figure 9.5: Expected and observed limits for 400 GeV non-SM Higgs boson scalar benchmark samples.

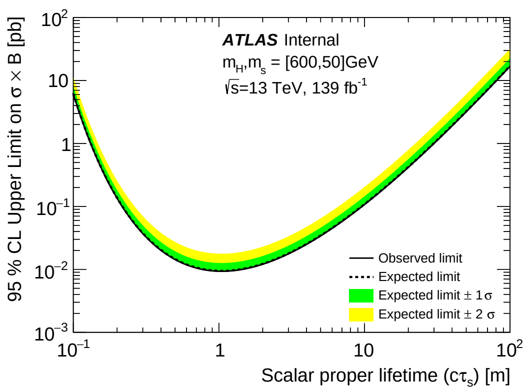

(a)

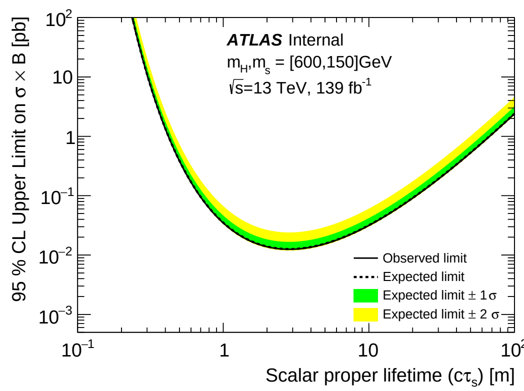

(b)

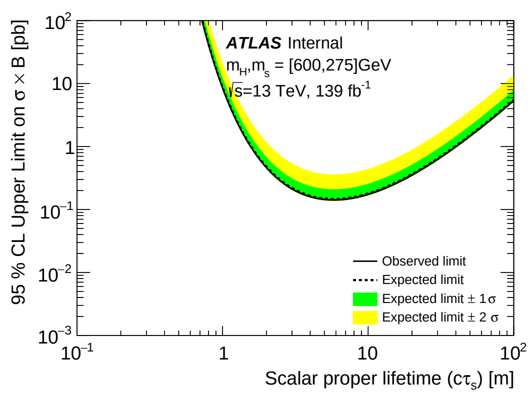

(c)

Figure 9.6: Expected and observed limits for 600 GeV non-SM Higgs boson scalar benchmark samples.

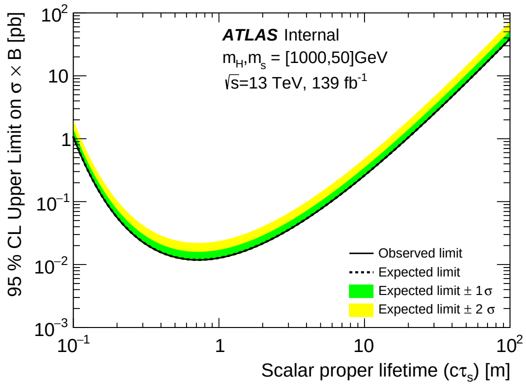

(a)

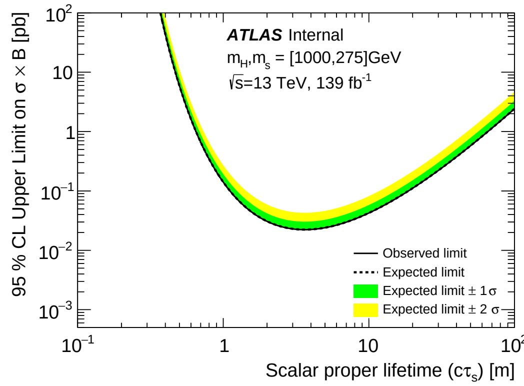

(b)

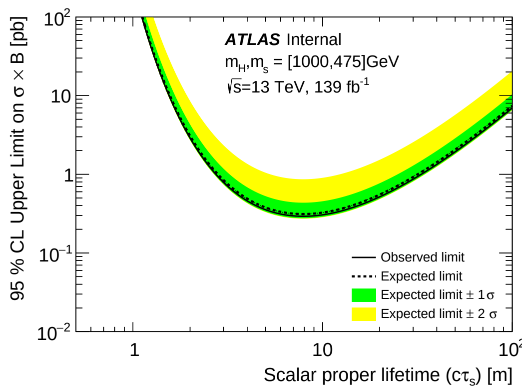

(c)

Figure 9.7: Expected and observed limits for 1000 GeV non-SM Higgs boson scalar benchmark samples.

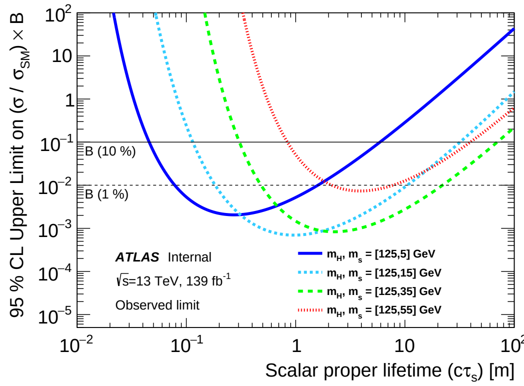

(a)

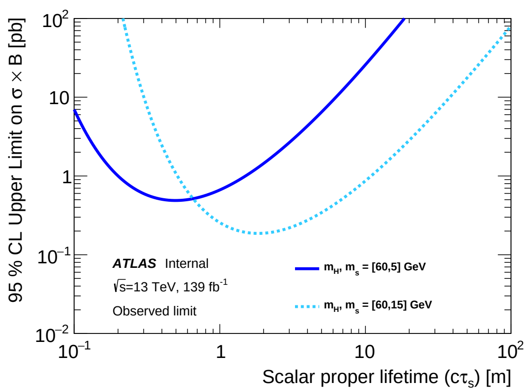

(b)

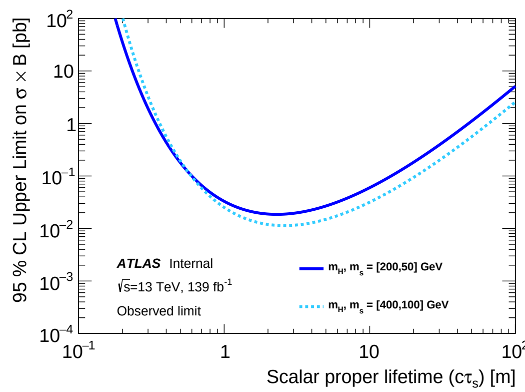

(c)

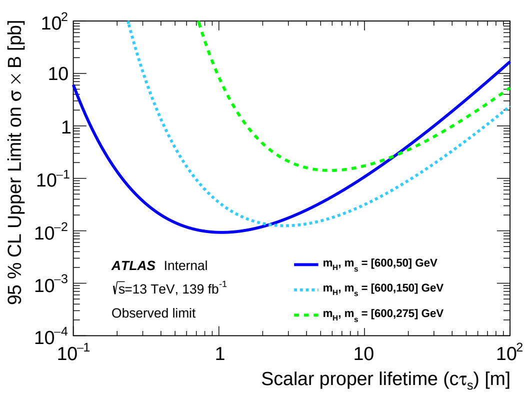

(d)

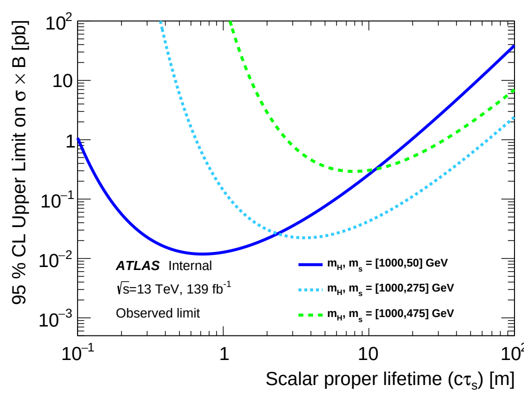

(e)

Figure 9.8: Observed limits for all the $H \rightarrow ss$ MC benchmark models.

9.2.2 Stat-only Limits

Figures 9.9 – 9.14 presents upper limit results considering only the statistical uncertainties on the number of signal and background events. Table 9.3 shows the numerical values of limits with full uncertainties calculated at $c\tau_s = 5$ m. Table 9.4 shows the numerical values of statistics-only limits calculated at $c\tau_s = 5$ m. Comparison of the statistical-only and statistical plus systematics results shows only a small difference. This means the two MS vertex search for long-lived particles is presently limited by statistics.

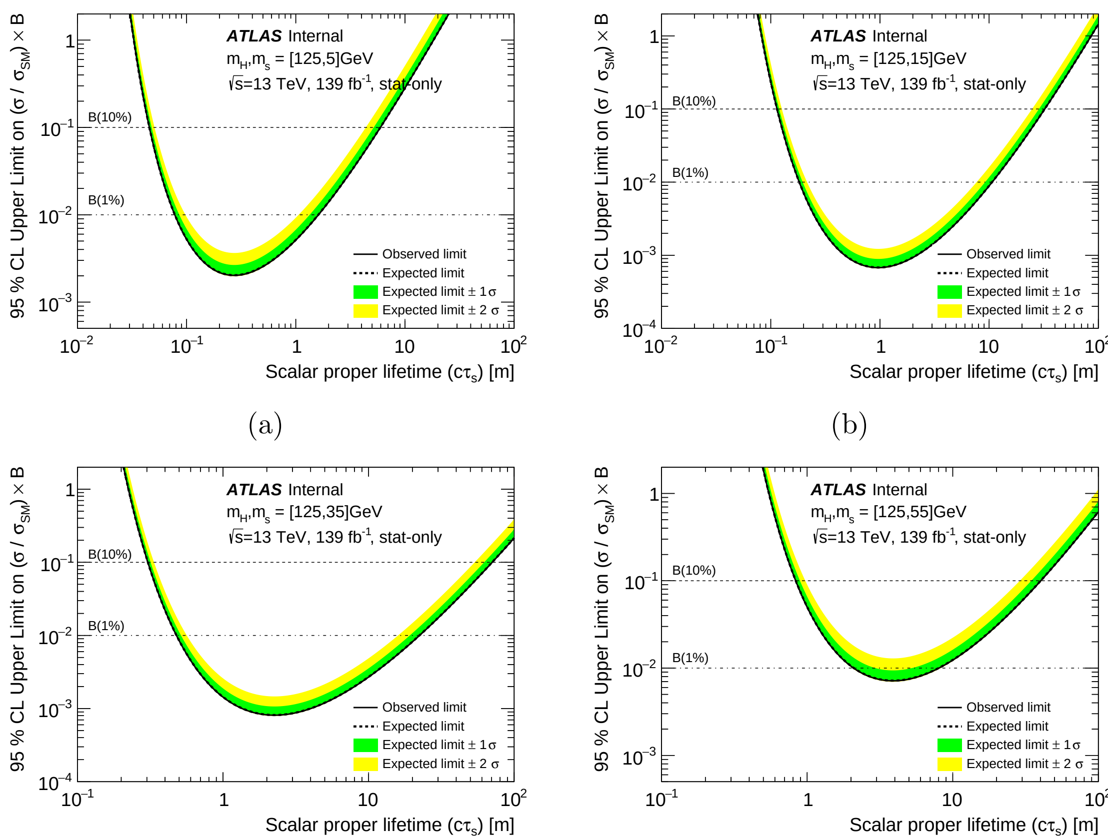

Figure 9.9: Expected limits for the 125 GeV boson benchmark samples with no systematic uncertainties.

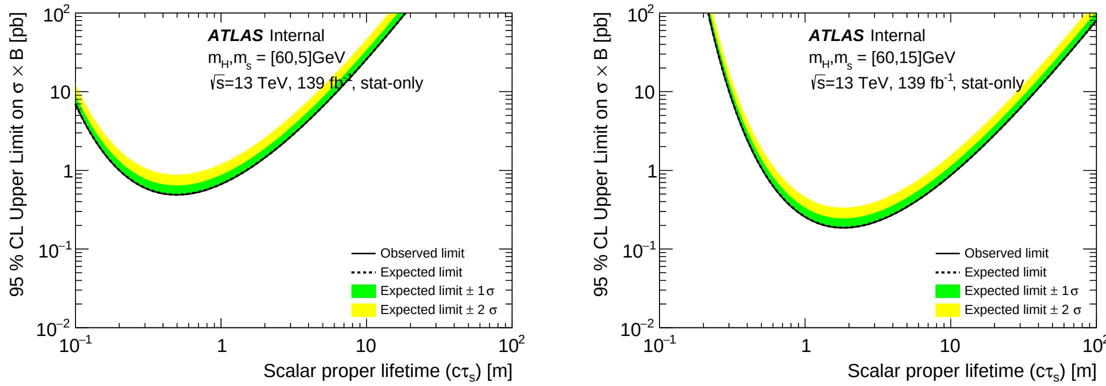

(a) (b)

Figure 9.10: Expected limits for 60 GeV non-SM Higgs boson scalar benchmark samples with no systematic uncertainties.

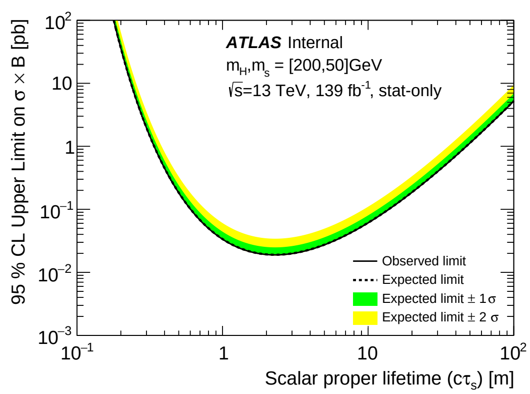

(a)

Figure 9.11: Expected limits for 200 GeV non-SM Higgs boson scalar benchmark samples with no systematic uncertainties.

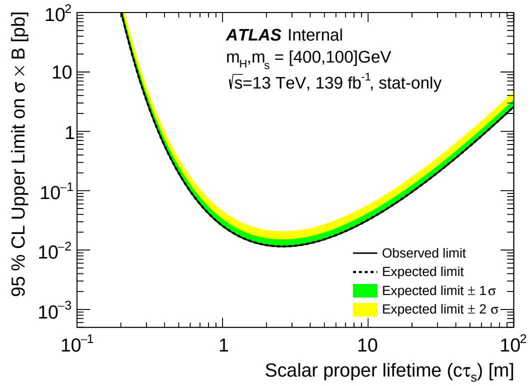

(a)

Figure 9.12: Expected limits for 400 GeV non-SM Higgs boson scalar benchmark samples with no systematic uncertainties.

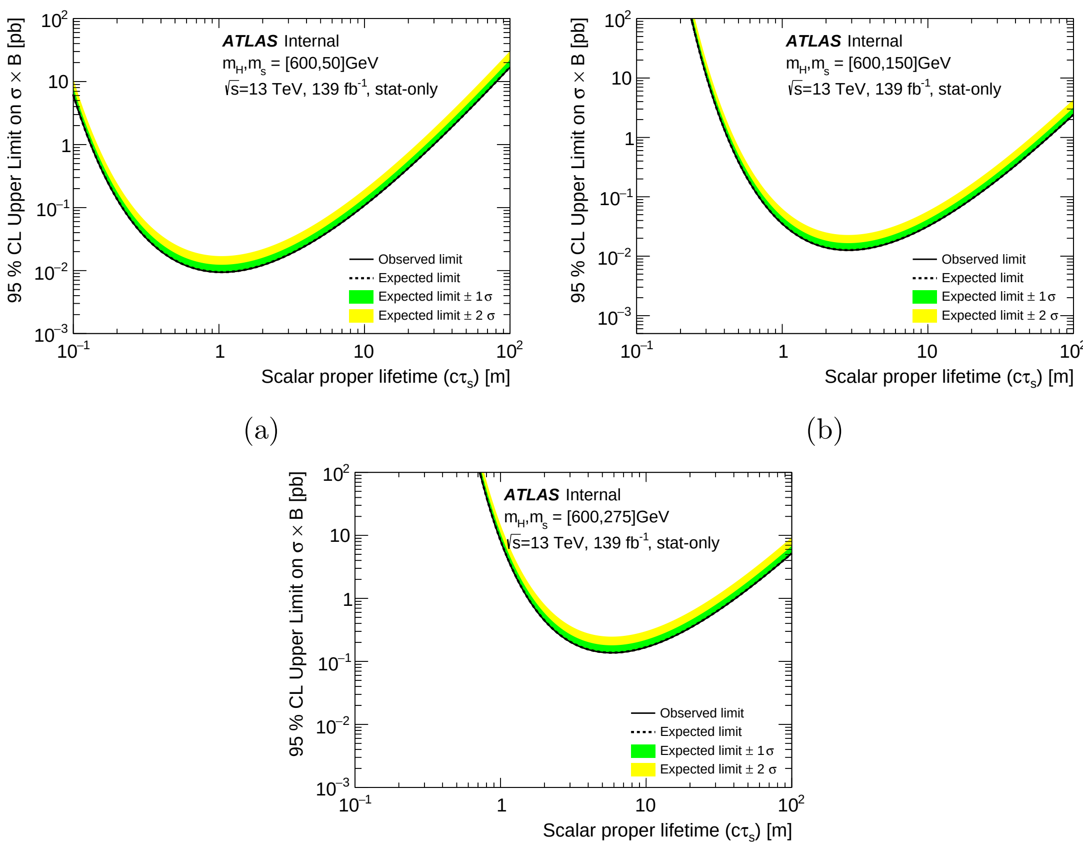

(a) (b) (c)

Figure 9.13: Expected and limits for 600 GeV non-SM Higgs boson scalar benchmark samples with no systematic uncertainties.

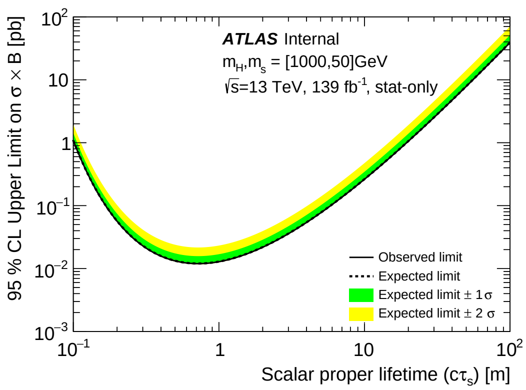

(a)

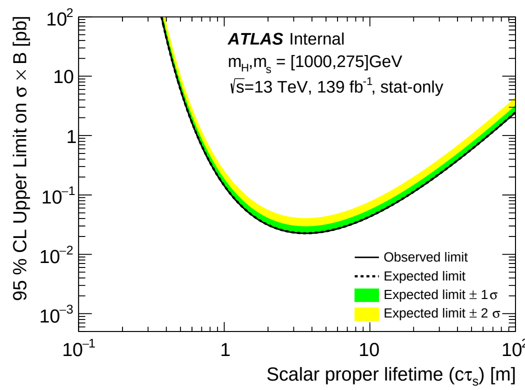

(b)

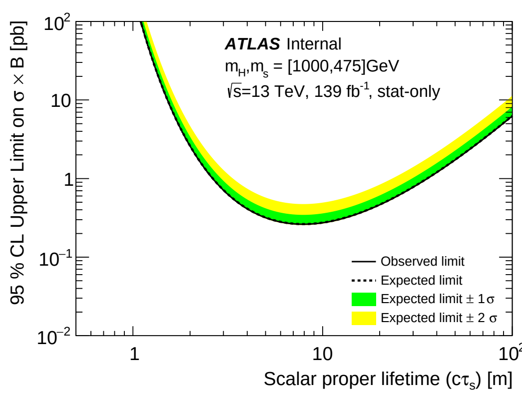

(c)

Figure 9.14: Expected limits for 1000 GeV non-SM Higgs boson scalar benchmark samples with no systematic uncertainties.

m_H [GeV]	m_s [GeV]	Obs.	Exp.	$+1\sigma$	-1σ	$+2\sigma$	-2σ
125	5	0.072	0.074	0.10	0.068	0.17	0.062
125	15	0.0028	0.0028	0.0037	0.0028	0.0054	0.0027
125	35	0.0012	0.0012	0.0016	0.0012	0.0026	0.0012
125	55	0.0077	0.0078	0.011	0.0077	0.018	0.0075

m_H [GeV]	m_s [GeV]	Obs. [pb]	Exp. [pb]	$+1\sigma$ [pb]	-1σ [pb]	$+2\sigma$ [pb]	-2σ [pb]
60	5	6.5	6.6	9.2	6.4	14.8	6.2
60	15	0.34	0.36	0.49	0.34	0.82	0.34
200	50	0.027	0.028	0.038	0.027	0.058	0.023
400	100	0.015	0.015	0.020	0.015	0.030	0.015
600	50	0.034	0.034	0.046	0.034	0.065	0.034
600	150	0.015	0.016	0.021	0.015	0.030	0.015
600	275	0.14	0.15	0.21	0.14	0.37	0.14
1000	50	0.076	0.076	0.10	0.075	0.14	0.073
1000	275	0.024	0.024	0.033	0.024	0.046	0.024
1000	475	0.36	0.38	0.53	0.34	1.1	0.33

Table 9.3: Observed and expected limit with its 1σ and 2σ uncertainty bands calculated at $c\tau_s = 5.0$ m. All uncertainties are applied. For samples with $m_H = 125$ GeV, upper limits are set on $(\sigma/\sigma_{\mathrm{SM}}) \times B$. For samples with $m_H \neq 125$ GeV, upper limits are set on $\sigma \times B$ with units of pb.

One may be curious why the -1σ and -2σ bands are absent in the expected limit plots. This is caused by the Poisson likelihood with close-to-zero background. Figure 9.15 shows the distributions of $\tilde{q}_\mu$ under the signal-plus-background hypothesis and the background-only hypothesis, with $b = 0.32$ and statistics-only condition. When computing the expected limits, the observed number of events n is equal to the expected number of backgrounds b (0.32), which corresponds to the dashed line. The rightmost bin corresponds to $n = 0$. Due to the discreteness of the distribution shown in the figure, there is no $\tilde{q}_\mu$ distributed in the region $[0, 0.32]$. Therefore, when n varies between 0 and 0.32, the p-value p_μ stays as a constant, which means that p_μ does not have a downward variation. Thus, the -1σ and -2σ variations on the expected limit disappear.

m_H [GeV]	m_s [GeV]	Obs.	Exp.	$+1\sigma$	-1σ	$+2\sigma$	-2σ
125	5	0.071	0.072	0.094	0.071	0.13	0.069
125	15	0.0028	0.0028	0.0036	0.0027	0.005	0.0027
125	35	0.0012	0.0012	0.0016	0.0012	0.0022	0.0012
125	55	0.0075	0.0075	0.0098	0.0074	0.013	0.0073

m_H [GeV]	m_s [GeV]	Obs. [pb]	Exp. [pb]	$+1\sigma$ [pb]	-1σ [pb]	$+2\sigma$ [pb]	-2σ [pb]
60	5	6.5	6.5	8.5	6.4	11.7	6.3
60	15	0.34	0.34	0.45	0.34	0.62	0.33
200	50	0.027	0.027	0.036	0.027	0.049	0.027
400	100	0.015	0.015	0.020	0.015	0.027	0.015
600	50	0.034	0.034	0.045	0.034	0.062	0.033
600	150	0.016	0.016	0.021	0.015	0.028	0.015
600	275	0.14	0.14	0.18	0.14	0.25	0.14
1000	50	0.077	0.077	0.10	0.076	0.14	0.075
1000	275	0.024	0.024	0.032	0.024	0.044	0.024
1000	475	0.32	0.32	0.42	0.32	0.57	0.31

Table 9.4: Stat-only observed and expected limit with its 1σ and 2σ uncertainty bands calculated at $c\tau_s = 5.0$ m. For samples with $m_H = 125$ GeV, upper limits are set on $(\sigma/\sigma_{\rm SM}) \times B$. For samples with $m_H \neq 125$ GeV, upper limits are set on $\sigma \times B$ with units of pb.

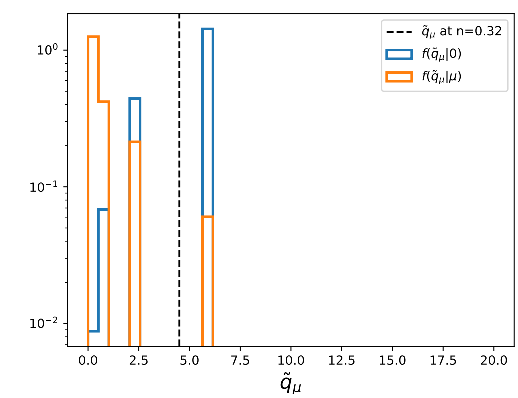

Figure 9.15: The distributions of $\tilde{q}_\mu$ under the signal-plus-background hypothesis, $f(\tilde{q}_\mu|\mu)$, and the distribution under the background-only hypothesis, $f(\tilde{q}_\mu|0)$. The systematic uncertainty is not applied. The dashed line corresponds to the $\tilde{q}_\mu$ obtained by assuming $n = b$ (0.32). The distributions are generated at $\mu = 3.0$.

CHAPTER 10

Conclusion

10.1 Summary of the Analysis

Searching for new long-lived particles is one of the directions that aim to explore for the new physics that is not predicted by the Standard Model (SM). This thesis presents an analysis that searches for two displaced vertices in the ATLAS muon spectrometer. The analysis uses proton-proton collision data collected at a center-of-mass energy of 13 TeV with an integrated luminosity of 139 fb^{-1}.

The benchmark model that is compared to data is the Hidden Sector model, which provides a scenario where two long-lived neutral scalars can be produced via a Higgs portal and then decay to SM fermions. This search is sensitive to a broad range of LLP decay modes, including $b\bar{b}$, $c\bar{c}$ and $\tau^+\tau^-$. The $c\tau_s$ sensitivity of this search ranges from a few centimeters to an order of 100 meters depending on the LLP mass.

In the analysis, the Muon RoI Cluster trigger, seeded by the L1 muon RoIs, is used to select the events of interest. In the signal Monte Carlo (MC) simulation, there exists a mismodelling of the trigger, which potentially can be propagated from the mismodelling of L1 muon RoIs. To correct the mismodelling, a SM multi-jet simulation is compared to the data using the distribution of the muon RoIs in a cone around punch-through jets. In the barrel (endcaps), the data have 24% (20%) more muon RoIs than in MC simulation. This difference is taken as a systematic uncertainty to the signal trigger efficiency.

Signal events can lead to displaced vertices in the muon spectrometer. In order to reconstruct these vertices, a tracklet-finding technique and a dedicated standalone reconstruction algorithm are used. The mismodelling of tracklets is estimated by comparing the multi-jet MC with data using the tracklet distribution in a cone around punch-through jets. The number of tracklets in the jet cone is found to be 20% larger in the MC compared to the data in the barrel, and 25% larger in the endcaps. To correct for this, the number of tracklets is scaled down according to these fractions by randomly removing tracklets from the signal samples. The vertex reconstruction algorithm is rerun after the tracklet removal procedure. Another method that performs bin-by-bin reweighting on the tracklet distribution is used to provide a cross-check.

The difference between the scale factors derived by these two methods is used as a systematic uncertainty.

The main background in the signal region are vertices produced from punch-through jets. This background is significantly reduced by requiring the MS vertex to be isolated from calorimeter jets and Inner Detector tracks. The remaining background arises from a combination of remaining punch-through jets and non-collision hits. This background is estimated by a data-driven method using both main stream and zero-bias stream data. The zero-bias data are reweighted to have the same pileup profile as the main stream data, and are used to calculate the probability to create a MS vertex from background events. The total number of background events in the signal region is estimated to be 0.32 ± 0.05. The background estimation method is validated in an orthogonal region. Due to the good validation result, no systematic uncertainties are added to the background. The analysis is unblinded after background validation and zero data events are observed in the signal region.

To estimate the expected number of signal events at different LLP proper lifetimes, a toy MC method that uses an LLP sample produced at generator level and applies the appropriate trigger efficiency and vertex reconstruction efficiency is employed. This method is improved from the one used by the 2015-2016 analysis and gives a more accurate estimation of the number of expected signal events with reduced statistical uncertainty and reduced extrapolation systematic uncertainty. This method is validated by checking the outputs of the signal efficiency from two signal samples generated at different lifetimes and a good closure is seen between these samples.

With no excess observed in the signal region, a 95% confidence level (CL) limit is evaluated for each benchmark MC sample using the CLs method with the profile log-likelihood ratio test statistic. For samples with $m_H = 125$ GeV, upper limits are derived for the branching fraction B of the $H \to ss$ process. The 95% CL exclusion ranges for the LLP proper lifetimes $c\tau_s$ are given at $B = 1\%$ and $B = 10\%$, respectively. The branching fraction above 10% are excluded for $c\tau_s$ from about 4 cm to about 71.3 m depending on the LLP masses. In the 2015-2016 analysis, the $c\tau_s$ exclusion range at $B = 10\%$ given by the MS two-vertex search for benchmark sample with $m_H = 125$ GeV and $m_s = 5$ GeV is [0.06, 4.39], whereas the corresponding exclusion range using 139 fb^{-1} data is [0.04, 5.9]. The improvement on the limits mainly benefits from the increase of the integrated luminosity.

For samples with $m_H \neq 125$ GeV, the upper limit is set on the cross section of $H \to ss$ production. All the signal samples show a sensitivity to a cross section that is less than 1 pb within a certain $c\tau_s$ range. The cross section above 1 pb can be excluded for $c\tau_s$ as small as 0.13 m and as large as 68.6 m depending on the masses.

10.2 Future Work

The LHC Long Shutdown 2 scheduled from 2019 to 2021 gives the ATLAS detector a chance to upgrade its tracking, calorimeter and muon system in order to prepare for the upcoming LHC Run 3 data-taking period. In Run 3, the center-of-mass energy of proton-proton collision will be upgraded to 14 TeV and approximately 300 fb^{-1} of integrated luminosity of collision data is expected to be collected. For the MS two-vertex search, there are some aspects that can be considered to improve the overall Run 3 analysis:

- The detector fiducial region $0.7 < |\eta| < 1.3$ in the MS is removed from the analysis. If the vertices in this region can be properly reconstructed, an improved signal efficiency and increased statistics in the signal region can be obtained. To achieve this goal, an algorithm that can reconstruct vertices from tracklets in both barrel and endcap chambers is needed. Since the barrel and the endcaps use completely different strategies to reconstruct vertices, one can imagine it would be difficult to build an algorithm connecting these two regions. This may be the task that requires the largest effort in the future analysis.

- There are MC mismodellings of the muon RoIs and tracklets that are not understood in the current analysis. One possible source for the mismodelling may be the cosmic ray muons or cavern background, which is a mixture of prompt particles from recent proton collisions. These backgrounds are not well modeled by the simulation and may therefore contribute to the difference between the data and MC.

  Another possible source may be related to a poor understanding of punch-through jets, since the mismodelling estimation is based on muon RoIs and tracklets in a punch-through jet cone. In the analysis, the punch-through jet is required to be associated with at least 50 muon segments. However, by varying the number of associated muon segments, the mismodelling factor could change accordingly. In the future analysis, it would be better to find a "standard" way that defines a punch-through jet. Punch-through jets are not well modeled in the MC and also need additional study. To reduce the systematic uncertainties due to mismodelling, more studies will be needed in the Run 3 analysis.

- The toy MC lifetime extrapolation method generally behaves well for the analysis, but it also has a limitation. This method assumes that in the signal region each of the two vertices is reconstructed independently. This assumption could fail when the two LLPs are not well separated and have wide decays. This happens when the mass of LLP becomes large. For example, we see a larger extrapolation systematic uncertainty for the sample with the sample with $m_H = 1000$ GeV and $m_s = 475$ GeV. In this sample, the two vertices may be correlated and thus the toy MC method does not provide a good estimation. A correction that compensates for the correlation effect needs to be considered.

Searching for one MS displaced vertex is another topology that can be applied to the $H \to ss$ process. The probability to have two LLPs with longer or shorter lifetimes decay inside the MS detector region is increasingly smaller compared to the one LLP case. Thus, the one-vertex search would be sensitive to a wider range of LLP proper lifetimes. The combination of one-vertex and two-vertex search will give rise to a much improved limit.

The one-vertex search using 139 fb^{-1} data is an ongoing analysis. The baseline selection includes: events pass GRL and event cleaning; events have a good primary vertex with at least two tracks; events pass the Muon RoI Cluster trigger; events have only one MS vertex reconstructed in the barrel ($|\eta| < 0.7$) or endcaps ($1.3 < |\eta| < 2.5$). The expected number of background can be estimated by the ABCD method. The ABCD method depends on two uncorrelated variables that can discriminate the signal from background. By selecting an appropriate region for each of these two variables, one can define a region A rich in signal events, and three control regions B, C and D on an ABCD plane with the two variables forming the X and Y axes. The number of background events in region A can be estimated from the number of events in the other three regions.

One of the main tasks is to find the two uncorrelated variables. One of the variable is chosen to be the minimum ΔR between the MS vertex and jets, and the MS vertex and tracks, $\min(\Delta R(\text{vertex}, \text{jet}), \Delta R(\text{vertex}, \text{track}))$, which provides an extremely good signal separation from the punch-through jets. The other variable will be determined by a multivariate technique. The Boost Decision Tree (BDT) is likely to be the choice as it shows a good signal acceptance and background rejection.

Currently, the BDT is trained on a set of input variables including detector hits (nMDT, nRPC, nTGC), the mean and RMS value of ΔR between the MS vertex and tracklets, the mean and RMS value of ΔR between the MS vertex and muon segments. These input variables are chosen to be uncorrelated to the jets or tracks, so that the BDT output is independent from the other ABCD variable.

Once two ABCD variables are determined, studies are needed to check if there are other backgrounds in the ABCD plane besides the punch-through jet background. This is because the ABCD method relies on there being only one source of background, or multiple sources that have identical behavior in the ABCD plane. If the contribution from other backgrounds is negligible, then the defined ABCD plane needs to be validated using a separate validation region rich in background and comparing the expected number of events with the observed one. Once the method for determining background is validated, the analysis can be unblinded. The baryogenesis model described in Section 2.2.2 will be included besides the Hidden Sector model.

The plan for the one-vertex search is to be combined with the two-vertex search. If no excess is found in the one-vertex signal region, a combined limit will be given. From the two-vertex search, the 95% CL upper limit of the branching fraction of the SM Higgs boson to long-lived scalars reaches 1% for all of the benchmark samples and even 0.1% for some of the samples. However, the $c\tau_s$ exclusion ranges for these branching fractions are about $\mathcal{O}(10\text{ m})$ or even less. A wide range of LLP lifetime is not strictly constrained by the MS search. As a result, there are still many opportunities to search for the LLP productions via the Higgs portal in other ATLAS detector regions and the CMS detector, or other future detectors designed for the LLP search like MATHUSLA [160].

REFERENCES

[1] M. K. Gaillard, P. D. Grannis, and F. J. Sciulli, *The Standard model of particle physics*, *Rev. Mod. Phys.* **71** (1999) S96–S111, [hep-ph/9812285].

[2] S. F. Novaes, *Standard model: An Introduction*, in *10th Jorge Andre Swieca Summer School: Particle and Fields*, 1, 1999. hep-ph/0001283.

[3] **ATLAS** Collaboration, G. Aad et al., *Observation of a new particle in the search for the Standard Model Higgs boson with the ATLAS detector at the LHC*, *Phys. Lett. B* **716** (2012) 1–29, [arXiv:1207.7214].

[4] **CMS** Collaboration, S. Chatrchyan et al., *Observation of a New Boson at a Mass of 125 GeV with the CMS Experiment at the LHC*, *Phys. Lett. B* **716** (2012) 30–61, [arXiv:1207.7235].

[5] P. Fayet, *Supersymmetry and Weak, Electromagnetic and Strong Interactions*, *Phys. Lett. B* **64** (1976) 159.

[6] P. Fayet, *Spontaneously Broken Supersymmetric Theories of Weak, Electromagnetic and Strong Interactions*, *Phys. Lett. B* **69** (1977) 489.

[7] G. F. Giudice and A. Romanino, *Erratum to: "Split supersymmetry" [Nucl. Phys. B 699 (2004) 65]*, *Nuclear Physics B* **706** (Jan., 2005) 487–487, [hep-ph/0406088].

[8] J. A. L. Hewett, B. Lillie, M. Masip, and T. G. Rizzo, *Signatures of long-lived gluinos in split supersymmetry*, *Journal of High Energy Physics* **2004** (Sept., 2004) 070, [hep-ph/0408248].

[9] R. Barbier, C. Bérat, M. Besançon, M. Chemtob, A. Deandrea, E. Dudas, P. Fayet, S. Lavignac, G. Moreau, E. Perez, and Y. Sirois, *R-Parity-violating supersymmetry*, *PhR* **420** (Nov., 2005) 1–195, [hep-ph/0406039].

[10] J. Fan, M. Reece, and J. T. Ruderman, *Stealth supersymmetry*, *Journal of High Energy Physics* **2011** (Nov., 2011) 12, [arXiv:1105.5135].

[11] J. Fan, M. Reece, and J. T. Ruderman, *A stealth supersymmetry sampler*, *Journal of High Energy Physics* **2012** (July, 2012) 196, [arXiv:1201.4875].

[12] M. J. Strassler and K. M. Zurek, *Echoes of a hidden valley at hadron colliders*, *Physics Letters B* **651** (Aug., 2007) 374–379, [hep-ph/0604261].

[13] M. J. Strassler and K. M. Zurek, *Discovering the Higgs through highly-displaced vertices*, *Physics Letters B* **661** (Mar., 2008) 263–267, [`hep-ph/0605193`].

[14] Z. Chacko, H.-S. Goh, and R. Harnik, *Natural Electroweak Breaking from a Mirror Symmetry*, *PhRvL* **96** (June, 2006) 231802, [`hep-ph/0506256`].

[15] G. Burdman, Z. Chacko, H.-S. Goh, and R. Harnik, *Folded supersymmetry and the LEP paradox*, *Journal of High Energy Physics* **2007** (Feb., 2007) 009, [`hep-ph/0609152`].

[16] H. Cai, H.-C. Cheng, and J. Terning, *A quirky little Higgs model*, *Journal of High Energy Physics* **2009** (May, 2009) 045, [`arXiv:0812.0843`].

[17] N. Craig, S. Knapen, and P. Longhi, *Neutral Naturalness from Orbifold Higgs Models*, *PhRvL* **114** (Feb., 2015) 061803, [`arXiv:1410.6808`].

[18] M. L. Graesser, *Experimental Constraints on Higgs Boson Decays to TeV-scale Right-Handed Neutrinos*, *arXiv e-prints* (May, 2007) arXiv:0705.2190, [`arXiv:0705.2190`].

[19] M. L. Graesser, *Broadening the Higgs boson with right-handed neutrinos and a higher dimension operator at the electroweak scale*, *PhRvD* **76** (Oct., 2007) 075006, [`arXiv:0704.0438`].

[20] E. Izaguirre and B. Shuve, *Multilepton and lepton jet probes of sub-weak-scale right-handed neutrinos*, *PhRvD* **91** (May, 2015) 093010, [`arXiv:1504.02470`].

[21] G. Cottin, J. C. Helo, and M. Hirsch, *Searches for light sterile neutrinos with multitrack displaced vertices*, *PhRvD* **97** (Mar., 2018) 055025, [`arXiv:1801.02734`].

[22] K. Griest and D. Seckel, *Three exceptions in the calculation of relic abundances*, *Phys. Rev. D* **43** (May, 1991) 3191–3203.

[23] K. M. Zurek, *Asymmetric Dark Matter: Theories, signatures, and constraints*, *PhR* **537** (Apr., 2014) 91–121, [`arXiv:1308.0338`].

[24] L. J. Hall, K. Jedamzik, J. March-Russell, and S. M. West, *Freeze-in production of FIMP dark matter*, *Journal of High Energy Physics* **2010** (Mar., 2010) 80, [`arXiv:0911.1120`].

[25] Y. Cui and R. Sundrum, *Baryogenesis for weakly interacting massive particles*, *PhRvD* **87** (June, 2013) 116013, [`arXiv:1212.2973`].

[26] S. Ipek and J. March-Russell, *Baryogenesis via particle-antiparticle oscillations*, *PhRvD* **93** (June, 2016) 123528, [`arXiv:1604.00009`].

[27] Y. Cui, *Natural Baryogenesis from Unnatural Supersymmetry*, *JHEP* **12** (2013) 067, [`arXiv:1309.2952`].

[28] D. Curtin et al., *Long-Lived Particles at the Energy Frontier: The MATHUSLA Physics Case*, *Rept. Prog. Phys.* **82** (2019), no. 11 116201, [`arXiv:1806.07396`].

[29] **ATLAS Collaboration** Collaboration, *Summary Plots for Heavy Particle Searches and Long-lived Particle Searches*, Tech. Rep. ATL-PHYS-PUB-2020-011, CERN, Geneva, May, 2020.

[30] S. L. Glashow, *Partial Symmetries of Weak Interactions*, *Nucl. Phys.* **22** (1961) 579–588.

[31] S. Weinberg, *A Model of Leptons*, *Phys. Rev. Lett.* **19** (1967) 1264–1266.

[32] A. Salam, *Weak and Electromagnetic Interactions*, *Conf. Proc. C* **680519** (1968) 367–377.

[33] F. Englert and R. Brout, *Broken Symmetry and the Mass of Gauge Vector Mesons*, *Phys. Rev. Lett.* **13** (1964) 321–323.

[34] P. W. Higgs, *Broken Symmetries and the Masses of Gauge Bosons*, *Phys. Rev. Lett.* **13** (1964) 508–509.

[35] G. 't Hooft, *Renormalizable Lagrangians for Massive Yang-Mills Fields*, *Nucl. Phys. B* **35** (1971) 167–188.

[36] G. 't Hooft and M. J. G. Veltman, *Regularization and Renormalization of Gauge Fields*, *Nucl. Phys. B* **44** (1972) 189–213.

[37] S. L. Glashow, J. Iliopoulos, and L. Maiani, *Weak Interactions with Lepton-Hadron Symmetry*, *Phys. Rev. D* **2** (1970) 1285–1292.

[38] N. Cabibbo, *Unitary Symmetry and Leptonic Decays*, *Phys. Rev. Lett.* **10** (1963) 531–533.

[39] M. Kobayashi and T. Maskawa, *CP Violation in the Renormalizable Theory of Weak Interaction*, *Prog. Theor. Phys.* **49** (1973) 652–657.

[40] G. Altarelli, *Partons in Quantum Chromodynamics*, *Phys. Rept.* **81** (1982) 1.

[41] **E598** Collaboration, J. J. Aubert et al., *Experimental Observation of a Heavy Particle J*, *Phys. Rev. Lett.* **33** (1974) 1404–1406.

[42] **SLAC-SP-017** Collaboration, J. E. Augustin et al., *Discovery of a Narrow Resonance in e^+e^- Annihilation*, *Phys. Rev. Lett.* **33** (1974) 1406–1408.

[43] S. W. Herb et al., *Observation of a Dimuon Resonance at 9.5-GeV in 400-GeV Proton-Nucleus Collisions*, *Phys. Rev. Lett.* **39** (1977) 252–255.

[44] **UA1** Collaboration, G. Arnison et al., *Experimental Observation of Isolated Large Transverse Energy Electrons with Associated Missing Energy at* $\sqrt{s} = 540$ *GeV*, *Phys. Lett. B* **122** (1983) 103–116.

[45] **UA2** Collaboration, M. Banner et al., *Observation of Single Isolated Electrons of High Transverse Momentum in Events with Missing Transverse Energy at the CERN anti-p p Collider*, *Phys. Lett. B* **122** (1983) 476–485.

[46] **UA1** Collaboration, G. Arnison et al., *Experimental Observation of Lepton Pairs of Invariant Mass Around 95-GeV/c**2 at the CERN SPS Collider*, *Phys. Lett. B* **126** (1983) 398–410.

[47] **UA2** Collaboration, P. Bagnaia et al., *Evidence for* $Z^0 \to e^+e^-$ *at the CERN* $\bar{p}p$ *Collider*, *Phys. Lett. B* **129** (1983) 130–140.

[48] **CDF** Collaboration, F. Abe et al., *Observation of top quark production in* $\bar{p}p$ *collisions*, *Phys. Rev. Lett.* **74** (1995) 2626–2631, [hep-ex/9503002].

[49] **D0** Collaboration, S. Abachi et al., *Observation of the top quark*, *Phys. Rev. Lett.* **74** (1995) 2632–2637, [hep-ex/9503003].

[50] **DONUT** Collaboration, K. Kodama et al., *Observation of tau neutrino interactions*, *Phys. Lett. B* **504** (2001) 218–224, [hep-ex/0012035].

[51] G. Altarelli and F. Feruglio, *Theoretical models of neutrino masses and mixings*, *Springer Tracts Mod. Phys.* **190** (2003) 169–207, [hep-ph/0206077].

[52] K. G. Wilson, *Confinement of quarks*, *Phys. Rev. D* **10** (Oct, 1974) 2445–2459.

[53] J. C. Collins, D. E. Soper, and G. F. Sterman, *Factorization for Short Distance Hadron - Hadron Scattering*, *Nucl. Phys. B* **261** (1985) 104–142.

[54] **NNPDF** Collaboration, R. D. Ball et al., *Parton distributions from high-precision collider data*, *Eur. Phys. J. C* **77** (2017), no. 10 663, [arXiv:1706.00428].

[55] T.-J. Hou et al., *New CTEQ global analysis of quantum chromodynamics with high-precision data from the LHC*, *Phys. Rev. D* **103** (2021), no. 1 014013, [arXiv:1912.10053].

[56] A. D. Martin, W. J. Stirling, R. S. Thorne, and G. Watt, *Parton distributions for the LHC*, *Eur. Phys. J. C* **63** (2009) 189–285, [arXiv:0901.0002].

[57] **H1, ZEUS** Collaboration, H. Abramowicz et al., *Combination and QCD analysis of charm and beauty production cross-section measurements in deep inelastic ep scattering at HERA*, *Eur. Phys. J. C* **78** (2018), no. 6 473, [arXiv:1804.01019].

[58] J. C. Pati and A. Salam, *Unified lepton-hadron symmetry and a gauge theory of the basic interactions*, *Phys. Rev. D* **8** (Aug, 1973) 1240–1251.

[59] H. Georgi and S. L. Glashow, *Unity of all elementary-particle forces*, *Phys. Rev. Lett.* **32** (Feb, 1974) 438–441.

[60] S. Weinberg, *Photons and gravitons in perturbation theory: Derivation of Maxwell's and Einstein's equations*, *Phys. Rev.* **138** (1965) B988–B1002.

[61] C. Csáki and P. Tanedo, *Beyond the Standard Model*, in *2013 European School of High-Energy Physics*, pp. 169–268, 2015. arXiv:1602.04228.

[62] N. Arkani-Hamed, S. Dimopoulos, and G. R. Dvali, *The Hierarchy problem and new dimensions at a millimeter*, *Phys. Lett. B* **429** (1998) 263–272, [hep-ph/9803315].

[63] D. B. Kaplan, H. Georgi, and S. Dimopoulos, *Composite Higgs Scalars*, *Phys. Lett. B* **136** (1984) 187–190.

[64] **Daya Bay** Collaboration, F. P. An et al., *Observation of electron-antineutrino disappearance at Daya Bay*, *Phys. Rev. Lett.* **108** (2012) 171803, [arXiv:1203.1669].

[65] **RENO** Collaboration, J. K. Ahn et al., *Observation of Reactor Electron Antineutrino Disappearance in the RENO Experiment*, *Phys. Rev. Lett.* **108** (2012) 191802, [arXiv:1204.0626].

[66] **Double Chooz** Collaboration, Y. Abe et al., *Improved measurements of the neutrino mixing angle θ_{13} with the Double Chooz detector*, *JHEP* **10** (2014) 086, [arXiv:1406.7763]. [Erratum: JHEP 02, 074 (2015)].

[67] **T2K** Collaboration, K. Abe et al., *Observation of Electron Neutrino Appearance in a Muon Neutrino Beam*, *Phys. Rev. Lett.* **112** (2014) 061802, [arXiv:1311.4750].

[68] **MINOS** Collaboration, P. Adamson et al., *Electron neutrino and antineutrino appearance in the full MINOS data sample*, *Phys. Rev. Lett.* **110** (2013), no. 17 171801, [arXiv:1301.4581].

[69] L. Bergstrom, *Dark Matter Evidence, Particle Physics Candidates and Detection Methods*, *Annalen Phys.* **524** (2012) 479–496, [arXiv:1205.4882].

[70] **AMS** Collaboration, M. Aguilar et al., *Antiproton Flux, Antiproton-to-Proton Flux Ratio, and Properties of Elementary Particle Fluxes in Primary Cosmic Rays Measured with the Alpha Magnetic Spectrometer on the International Space Station*, *Phys. Rev. Lett.* **117** (2016), no. 9 091103.

[71] G. Steigman, *Primordial Nucleosynthesis: The Predicted and Observed Abundances and Their Consequences*, *PoS* **NICXI** (2010) 001, [arXiv:1008.4765].

[72] L. Canetti, M. Drewes, and M. Shaposhnikov, *Matter and Antimatter in the Universe*, *New J. Phys.* **14** (2012) 095012, [arXiv:1204.4186].

[73] P. Ronchese, *Measurement of the CP violating phase Φ_s with CMS and ATLAS*, in *12th Conference on the Intersections of Particle and Nuclear Physics*, 9, 2015. arXiv:1509.09266.

[74] **LHCb** Collaboration, R. Aaij et al., *First measurement of the CP-violating phase in $B_s^0 \to J/\psi(\to e^+e^-)\phi$ decays*, arXiv:2105.14738.

[75] R. D. Peccei, *The Strong CP problem and axions*, *Lect. Notes Phys.* **741** (2008) 3–17, [hep-ph/0607268].

[76] J. M. Pendlebury et al., *Revised experimental upper limit on the electric dipole moment of the neutron*, *Phys. Rev. D* **92** (2015), no. 9 092003, [arXiv:1509.04411].

[77] **ATLAS** Collaboration, G. Aad et al., *Combined measurements of Higgs boson production and decay using up to 80 fb^{-1} of proton-proton collision data at $\sqrt{s} =$ 13 TeV collected with the ATLAS experiment*, *Phys. Rev. D* **101** (2020), no. 1 012002, [arXiv:1909.02845].

[78] **CMS** Collaboration, A. M. Sirunyan et al., *Search for invisible decays of a Higgs boson produced through vector boson fusion in proton-proton collisions at $\sqrt{s} =$ 13 TeV*, *Phys. Lett. B* **793** (2019) 520–551, [arXiv:1809.05937].

[79] R. M. Schabinger and J. D. Wells, *A Minimal spontaneously broken hidden sector and its impact on Higgs boson physics at the large hadron collider*, *Phys. Rev. D* **72** (2005) 093007, [hep-ph/0509209].

[80] Y. Cui and B. Shuve, *Probing Baryogenesis with Displaced Vertices at the LHC*, *JHEP* **02** (2015) 049, [arXiv:1409.6729].

[81] **ALICE** Collaboration, K. Aamodt et al., *First proton-proton collisions at the LHC as observed with the ALICE detector: Measurement of the charged particle pseudorapidity density at s**(1/2) = 900-GeV*, *Eur. Phys. J. C* **65** (2010) 111–125, [arXiv:0911.5430].

[82] E. Mobs, *The CERN accelerator complex - 2019. Complexe des accélérateurs du CERN - 2019*, . General Photo.

[83] S. Myers, *The Large Hadron Collider 2008-2013*, *Int. J. Mod. Phys. A* **28** (2013) 1330035.

[84] **TOTEM** Collaboration, G. Anelli et al., *The TOTEM experiment at the CERN Large Hadron Collider*, *JINST* **3** (2008) S08007.

[85] **LHCf** Collaboration, E. Berti, *The LHCf experiment: present status and physics results*, `arXiv:1710.03991`.

[86] **MoEDAL** Collaboration, V. A. Mitsou, *The MoEDAL experiment at the LHC: status and results*, *J. Phys. Conf. Ser.* **873** (2017), no. 1 012010, [`arXiv:1703.07141`].

[87] M. Benedikt, P. Collier, V. Mertens, J. Poole, and K. Schindl, *LHC Design Report*. CERN Yellow Reports: Monographs. CERN, Geneva, 2004.

[88] B. Salvachúa, *Overview of proton-proton physics during run ii*, 2019.

[89] **ATLAS** Collaboration, G. Aad et al., *Performance of pile-up mitigation techniques for jets in pp collisions at $\sqrt{s} = 8$ TeV using the ATLAS detector*, *Eur. Phys. J. C* **76** (2016), no. 11 581, [`arXiv:1510.03823`].

[90] R. Steerenberg, *Batch Compression Merging and Splitting (BCMS). Batch Compression Merging and Splitting (BCMS)*, . General Photo.

[91] W. Herr and B. Muratori, *Concept of luminosity*, .

[92] **ATLAS** Collaboration, A. Airapetian et al., *ATLAS: Detector and physics performance technical design report. Volume 1*, .

[93] **ATLAS Collaboration** Collaboration, G. Aad et al., *The ATLAS Experiment at the CERN Large Hadron Collider*, *JINST* **3** (2008) S08003. 437 p. Also published by CERN Geneva in 2010.

[94] **ATLAS** Collaboration, G. Aad et al., *Alignment of the ATLAS Inner Detector in Run-2*, *Eur. Phys. J. C* **80** (2020), no. 12 1194, [`arXiv:2007.07624`].

[95] G. Aad et al., *ATLAS pixel detector electronics and sensors*, *JINST* **3** (2008) P07007.

[96] **ATLAS Collaboration** Collaboration, M. Capeans, G. Darbo, K. Einsweiller, M. Elsing, T. Flick, M. Garcia-Sciveres, C. Gemme, H. Pernegger, O. Rohne, and R. Vuillermet, *ATLAS Insertable B-Layer Technical Design Report*, Tech. Rep. CERN-LHCC-2010-013. ATLAS-TDR-19, Sep, 2010.

[97] **ATLAS Collaboration** Collaboration, *ATLAS inner detector: Technical Design Report, 1.* Technical design report. ATLAS. CERN, Geneva, 1997.

[98] **ATLAS TRT Collaboration** Collaboration, E. Abat et al., *The ATLAS Transition Radiation Tracker (TRT) proportional drift tube: design and performance*, *JINST* **3** (2008) P02013.

[99] **ATLAS Liquid Argon Calorimeter** Collaboration, D. Gillberg, *Performance of the ATLAS forward calorimeters in first LHC data*, *J. Phys. Conf. Ser.* **293** (2011) 012041.

[100] **ATLAS** Collaboration, G. Aad et al., *Resolution of the ATLAS muon spectrometer monitored drift tubes in LHC Run 2*, *JINST* **14** (2019), no. 09 P09011, [`arXiv:1906.12226`].

[101] **ATLAS** Collaboration, G. Aad et al., *Search for long-lived neutral particles produced in pp collisions at $\sqrt{s} = 13$ TeV decaying into displaced hadronic jets in the ATLAS inner detector and muon spectrometer*, *Phys. Rev. D* **101** (2020), no. 5 052013, [`arXiv:1911.12575`].

[102] **ATLAS Collaboration** Collaboration, *Performance of the reconstruction of large impact parameter tracks in the ATLAS inner detector*, Tech. Rep. ATL-PHYS-PUB-2017-014, CERN, Geneva, Jul, 2017.

[103] **ATLAS** Collaboration, G. Aad et al., *Search for long-lived, massive particles in events with a displaced vertex and a muon with large impact parameter in pp collisions at $\sqrt{s} = 13$ TeV with the ATLAS detector*, *Phys. Rev. D* **102** (2020), no. 3 032006, [`arXiv:2003.11956`].

[104] **ATLAS** Collaboration, M. Aaboud et al., *Search for long-lived, massive particles in events with displaced vertices and missing transverse momentum in $\sqrt{s}$ = 13 TeV pp collisions with the ATLAS detector*, *Phys. Rev. D* **97** (2018), no. 5 052012, [`arXiv:1710.04901`].

[105] **ATLAS** Collaboration, M. Aaboud et al., *Search for long-lived neutral particles in pp collisions at $\sqrt{s}$ = 13 TeV that decay into displaced hadronic jets in the ATLAS calorimeter*, *Eur. Phys. J. C* **79** (2019), no. 6 481, [`arXiv:1902.03094`].

[106] **ATLAS** Collaboration, M. Aaboud et al., *Search for long-lived particles in final states with displaced dimuon vertices in pp collisions at* $\sqrt{s} = 13$ *TeV with the ATLAS detector*, *Phys. Rev. D* **99** (2019), no. 1 012001, [arXiv:1808.03057].

[107] **ATLAS** Collaboration, G. Aad et al., *Search for light long-lived neutral particles produced in pp collisions at* $\sqrt{s} = 13$ *TeV and decaying into collimated leptons or light hadrons with the ATLAS detector*, *Eur. Phys. J. C* **80** (2020), no. 5 450, [arXiv:1909.01246].

[108] A. Falkowski, J. T. Ruderman, T. Volansky, and J. Zupan, *Hidden Higgs Decaying to Lepton Jets*, *JHEP* **05** (2010) 077, [arXiv:1002.2952].

[109] A. Falkowski, J. T. Ruderman, T. Volansky, and J. Zupan, *Discovering Higgs Decays to Lepton Jets at Hadron Colliders*, *Phys. Rev. Lett.* **105** (2010) 241801, [arXiv:1007.3496].

[110] **ATLAS** Collaboration, M. Aaboud et al., *Search for long-lived charginos based on a disappearing-track signature in pp collisions at* $\sqrt{s} = 13$ *TeV with the ATLAS detector*, *JHEP* **06** (2018) 022, [arXiv:1712.02118].

[111] **ATLAS** Collaboration, M. Aaboud et al., *Search for heavy charged long-lived particles in proton-proton collisions at* $\sqrt{s} = 13$ *TeV using an ionisation measurement with the ATLAS detector*, *Phys. Lett. B* **788** (2019) 96–116, [arXiv:1808.04095].

[112] **ATLAS** Collaboration, G. Aad et al., *Search for nonpointing and delayed photons in the diphoton and missing transverse momentum final state in 8 TeV pp collisions at the LHC using the ATLAS detector*, *Phys. Rev. D* **90** (2014), no. 11 112005, [arXiv:1409.5542].

[113] **ATLAS** Collaboration, G. Aad et al., *ATLAS data quality operations and performance for 2015–2018 data-taking*, *JINST* **15** (2020), no. 04 P04003, [arXiv:1911.04632].

[114] **ATLAS Collaboration** Collaboration, *Luminosity determination in pp collisions at* $\sqrt{s} = 13$ *TeV using the ATLAS detector at the LHC*, Tech. Rep. ATLAS-CONF-2019-021, CERN, Geneva, Jun, 2019.

[115] G. Avoni et al., *The new LUCID-2 detector for luminosity measurement and monitoring in ATLAS*, *JINST* **13** (2018), no. 07 P07017.

[116] J. Alwall, R. Frederix, S. Frixione, V. Hirschi, F. Maltoni, O. Mattelaer, H. S. Shao, T. Stelzer, P. Torrielli, and M. Zaro, *The automated computation of tree-level and next-to-leading order differential cross sections, and their*

matching to parton shower simulations, *JHEP* **07** (2014) 079, [arXiv:1405.0301].

[117] T. Sjostrand, S. Mrenna, and P. Z. Skands, *A Brief Introduction to PYTHIA 8.1*, *Comput. Phys. Commun.* **178** (2008) 852–867, [arXiv:0710.3820].

[118] *ATLAS Pythia 8 tunes to 7 TeV data*, Tech. Rep. ATL-PHYS-PUB-2014-021, CERN, Geneva, Nov, 2014.

[119] **GEANT4** Collaboration, S. Agostinelli et al., *GEANT4–a simulation toolkit*, *Nucl. Instrum. Meth. A* **506** (2003) 250–303.

[120] R. Brun and F. Rademakers, *ROOT: An object oriented data analysis framework*, *Nucl. Instrum. Meth. A* **389** (1997) 81–86.

[121] T. Sjöstrand, S. Ask, J. R. Christiansen, R. Corke, N. Desai, P. Ilten, S. Mrenna, S. Prestel, C. O. Rasmussen, and P. Z. Skands, *An introduction to PYTHIA 8.2*, *Comput. Phys. Commun.* **191** (2015) 159–177, [arXiv:1410.3012].

[122] **ATLAS Collaboration** Collaboration, *The Pythia 8 A3 tune description of ATLAS minimum bias and inelastic measurements incorporating the Donnachie-Landshoff diffractive model*, Tech. Rep. ATL-PHYS-PUB-2016-017, CERN, Geneva, Aug, 2016.

[123] W. Buttinger, *Using Event Weights to account for differences in Instantaneous Luminosity and Trigger Prescale in Monte Carlo and Data*, tech. rep., CERN, Geneva, May, 2015.

[124] L. Lonnblad and S. Prestel, *Matching Tree-Level Matrix Elements with Interleaved Showers*, *JHEP* **03** (2012) 019, [arXiv:1109.4829].

[125] **ATLAS** Collaboration, G. Aad et al., *Operation of the ATLAS trigger system in Run 2*, *JINST* **15** (2020), no. 10 P10004, [arXiv:2007.12539].

[126] R. Achenbach et al., *The ATLAS level-1 calorimeter trigger*, *JINST* **3** (2008) P03001.

[127] E. F. Eisenhandler, *ATLAS Level-1 Calorimeter Trigger Algorithms*, Tech. Rep. ATL-DAQ-2004-011. CERN-ATL-DAQ-2004-011, CERN, Geneva, Sep, 2004.

[128] **ATLAS** Collaboration, G. Aad et al., *Performance of the ATLAS muon triggers in Run 2*, *JINST* **15** (2020), no. 09 P09015, [arXiv:2004.13447].

[129] **ATLAS Collaboration** Collaboration, R. Simoniello, *The ATLAS Level-1 Topological Processor: from design to routine usage in Run-2*, Tech. Rep. ATL-DAQ-PROC-2018-044, CERN, Geneva, Dec, 2018.

[130] **ATLAS** Collaboration, M. Aaboud et al., *Search for long-lived particles produced in pp collisions at $\sqrt{s} = 13$ TeV that decay into displaced hadronic jets in the ATLAS muon spectrometer*, *Phys. Rev. D* **99** (2019), no. 5 052005, [arXiv:1811.07370].

[131] **ATLAS** Collaboration, G. Aad et al., *Performance of the ATLAS muon trigger in pp collisions at $\sqrt{s} = 8$ TeV*, *Eur. Phys. J. C* **75** (2015) 120, [arXiv:1408.3179].

[132] **ATLAS** Collaboration, G. Aad et al., *A neural network clustering algorithm for the ATLAS silicon pixel detector*, *JINST* **9** (2014) P09009, [arXiv:1406.7690].

[133] R. Fruhwirth, *Application of Kalman filtering to track and vertex fitting*, *Nucl. Instrum. Meth. A* **262** (1987) 444–450.

[134] *Vertex Reconstruction Performance of the ATLAS Detector at $\sqrt{s} = 13$ TeV*, Tech. Rep. ATL-PHYS-PUB-2015-026, CERN, Geneva, Jul, 2015.

[135] **ATLAS** Collaboration, M. Aaboud et al., *Reconstruction of primary vertices at the ATLAS experiment in Run 1 proton–proton collisions at the LHC*, *Eur. Phys. J. C* **77** (2017), no. 5 332, [arXiv:1611.10235].

[136] T. Robertson and J. D. Cryer, *An iterative procedure for estimating the mode*, *Journal of the American Statistical Association* **69** (1974), no. 348 1012–1016, [https://www.tandfonline.com/doi/pdf/10.1080/01621459.1974.10480246].

[137] **ATLAS** Collaboration, G. Aad et al., *Topological cell clustering in the ATLAS calorimeters and its performance in LHC Run 1*, *Eur. Phys. J. C* **77** (2017) 490, [arXiv:1603.02934].

[138] M. Cacciari, G. P. Salam, and G. Soyez, *The anti-k_t jet clustering algorithm*, *JHEP* **04** (2008) 063, [arXiv:0802.1189].

[139] **ATLAS** Collaboration, M. Aaboud et al., *Jet energy scale measurements and their systematic uncertainties in proton-proton collisions at $\sqrt{s} = 13$ TeV with the ATLAS detector*, *Phys. Rev. D* **96** (2017), no. 7 072002, [arXiv:1703.09665].

[140] S. Catani, Y. L. Dokshitzer, M. H. Seymour, and B. R. Webber, *Longitudinally invariant K_t clustering algorithms for hadron hadron collisions*, *Nucl. Phys. B* **406** (1993) 187–224.

[141] M. Cacciari and G. P. Salam, *Pileup subtraction using jet areas*, *Phys. Lett. B* **659** (2008) 119–126, [arXiv:0707.1378].

[142] M. Cacciari, G. P. Salam, and G. Soyez, *The Catchment Area of Jets*, *JHEP* **04** (2008) 005, [arXiv:0802.1188].

[143] **ATLAS** Collaboration, G. Aad et al., *Jet energy measurement with the ATLAS detector in proton-proton collisions at $\sqrt{s} = 7$ TeV*, *Eur. Phys. J. C* **73** (2013), no. 3 2304, [arXiv:1112.6426].

[144] **ATLAS** Collaboration, M. Aaboud et al., *Determination of jet calibration and energy resolution in proton-proton collisions at $\sqrt{s} = 8$ TeV using the ATLAS detector*, *Eur. Phys. J. C* **80** (2020), no. 12 1104, [arXiv:1910.04482].

[145] *Selection of jets produced in 13TeV proton-proton collisions with the ATLAS detector*, Tech. Rep. ATLAS-CONF-2015-029, CERN, Geneva, Jul, 2015.

[146] *Tagging and suppression of pileup jets with the ATLAS detector*, Tech. Rep. ATLAS-CONF-2014-018, CERN, Geneva, May, 2014.

[147] **ATLAS** Collaboration, M. Aaboud et al., *Performance of missing transverse momentum reconstruction with the ATLAS detector using proton-proton collisions at $\sqrt{s} = 13$ TeV*, *Eur. Phys. J. C* **78** (2018), no. 11 903, [arXiv:1802.08168].

[148] M. J. Woudstra, *Precision of the ATLAS muon spectrometer*, 2002. Presented on 4 Dec 2002.

[149] **ATLAS** Collaboration, G. Aad et al., *Standalone vertex finding in the ATLAS muon spectrometer*, *JINST* **9** (2014) P02001, [arXiv:1311.7070].

[150] G. Ciapetti, H. Lubatti, and D. Ventura, *Standalone Vertex Finding in the ATLAS Muon Spectrometer*, Tech. Rep. ATLAS-COM-CONF-2012-102, CERN, Geneva, May, 2012.

[151] H. Russell, *Search for long-lived particles decaying in the muon spectrometer of the ATLAS detector at the LHC*, Dec, 2016. Presented 02 Dec 2016.

[152] **Belle** Collaboration, H. Ikeda et al., *A detailed test of the CsI(Tl) calorimeter for BELLE with photon beams of energy between 20-MeV and 5.4-GeV*, *Nucl. Instrum. Meth. A* **441** (2000) 401–426.

[153] G. Cowan, K. Cranmer, E. Gross, and O. Vitells, *Asymptotic formulae for likelihood-based tests of new physics*, *Eur. Phys. J. C* **71** (2011) 1554, [arXiv:1007.1727]. [Erratum: Eur.Phys.J.C 73, 2501 (2013)].

[154] A. L. Read, *Presentation of search results: The CL(s) technique*, *J. Phys. G* **28** (2002) 2693–2704.

[155] **LHC Higgs Cross Section Working Group** Collaboration, D. de Florian et al., *Handbook of LHC Higgs Cross Sections: 4. Deciphering the Nature of the Higgs Sector*, `arXiv:1610.07922`.

[156] C. Anastasiou, C. Duhr, F. Dulat, E. Furlan, T. Gehrmann, F. Herzog, A. Lazopoulos, and B. Mistlberger, *High precision determination of the gluon fusion Higgs boson cross-section at the LHC*, *JHEP* **05** (2016) 058, [`arXiv:1602.00695`].

[157] M. Cepeda et al., *Report from Working Group 2: Higgs Physics at the HL-LHC and HE-LHC*, *CERN Yellow Rep. Monogr.* **7** (2019) 221–584, [`arXiv:1902.00134`].

[158] L. Heinrich, M. Feickert, and G. Stark, "pyhf: v0.6.2." https://github.com/scikit-hep/pyhf/releases/tag/v0.6.2.

[159] L. Heinrich, M. Feickert, G. Stark, and K. Cranmer, *pyhf: pure-python implementation of histfactory statistical models*, *Journal of Open Source Software* **6** (2021), no. 58 2823.

[160] J. P. Chou, D. Curtin, and H. J. Lubatti, *New Detectors to Explore the Lifetime Frontier*, *Phys. Lett. B* **767** (2017) 29–36, [`arXiv:1606.06298`].